BUDOWNICTWO
I ARCHITEKTURA

BUDOWNICTWO
I ARCHITEKTURA

SPIS TREŚCI
CONTENTS

Deformability of the masonry subjected to shearing due to vertical displacements

Adam Piekarczyk

Department of Building Structures; Faculty of Civil Engineering; Silesian University of Technology;
5 Akademicka Street, 44-100 Gliwice, Poland;
Adam.Piekarczyk@polsl.pl iD *0000-0002-5790-9560*

Abstract: The paper presents the results of tests of masonry specimens subjected to vertical displacement, with limited deformations in a direction parallel to the masonry bed joints (horizontally) and additionally compressed in the direction perpendicular to the bed joints (vertically). Specimens in the form of fragments of masonry walls were made of solid ceramic brick and AAC blocks. Studies have shown that the nature of the relationship between wall deformation angles and shear stresses caused by vertical displacements depends on the values of accompanying compressive stresses normal to the plane of the masonry bed joints. Compressive stresses have a positive effect on the load-bearing capacity and crack resistance of this type of masonry walls and the angles of deformation occurring at the moment of cracking. The dependence of the transverse stiffness modulus on the value of shear stresses is strongly non-linear, but with increasing shear stresses, it stabilises at a certain level independent of the values of compressive stresses associated with shear.

Keywords: vertical shear, vertical wall displacement, transverse stiffness, shear deformation angle

1. Introduction

Vertical displacements of masonry walls may result from deformations of the structures on which they are directly supported, i.e. deflections of ceiling members, floors, lintel beams and foundations or displacements transferred from other elements adjacent to these walls, e.g. transverse walls and columns.

Uneven displacements of foundations and floors may be the effect of improper preparation of the subsoil [1]–[9] resulting from inadequate or uneven compaction, changes in water regimes due to drainage, land quality improvement, deep excavations in the vicinity, swelling or shrinkage of the subsoil caused by vegetation, displacement of expansive soils, soil leaching during plumbing or rainfall installations failure, loss of soil stability. Additional displacements of the subsoil may also be the result of erecting new buildings next to existing

ones, compaction of the soil and increasing loads due to vehicle traffic or other dynamic loads. Underground mining exploitation also causes the formation of continuous and discontinuous deformations on the land surface.

In masonry walls subjected to the influences mentioned above, usually a complex stress state occurs resulting not only from shear caused by vertical displacements. Additionally, the value and direction of the principal stresses causing cracking and failure are also affected by the limited freedom of deformation in the horizontal direction by the adjacent structural members and, in case of load-bearing walls, vertical compressive stresses transmitted to the wall from the upper storeys.

Research on unreinforced and reinforced masonry shear walls due to vertical displacements, among other research problems, has been conducted at the Civil Engineering Faculty of the Silesian University of Technology for over 20 years and published, among others, in works [1], [3], [5], [10]–[22]. The described research problem is rarely analysed experimentally and theoretically. The author is known only to a few foreign publications, which are quite loosely related to the subject presented here. Subject-related studies were described in reports from foreign researches [23]–[25]. On the one hand, it proves the originality of the presented research, and on the other hand, it makes it difficult to compare the results of the tests with the results from other research centres.

2. Specimens and test stand

2.1. Materials and specimens

The tests were carried out on specimens made of solid ceramic bricks and autoclaved aerated concrete blocks (AAC). The walls made of ceramic bricks had bed joints of normal thickness, nominally equal to 10 mm, while the specimens of AAC had thin bed joints with a nominal thickness of 3 mm and unfilled head joints.

For ceramic brick specimens, masonry units with mean compressive strength $f_B = 28.8$ N/mm^2 and normalised strength $f_b = 23.3$ N/mm^2 determined in accordance with PN-EN 772-1 [26] and with a coefficient of variation equal to 6.4% were used. A prescribed cement-lime mortar was used with a volume components ratio 1:1:6 (cement:lime:sand) with mean compressive strength determined according to PN-EN 998-2 [27] standard equal to $f_m = 9.7$ N/mm^2 with a coefficient of variation of 10.0%

AAC blocks with a nominal volume density of 500 kg/m^3 had a mean compressive strength of 2.7 N/mm^2 and normalised strength according to [26] $f_b = 3.1$ N/mm^2 with a coefficient of variation of 7.9%. The system prescribed mortar for thin joins bonding AAC blocks had a mean compressive strength according to [27] $f_m = 18.8$ N/mm^2 with a coefficient of variation of 9.6%.

The dimensions of the specimens are shown in Fig. 1. The thickness of the specimens made of ceramic bricks was 25 cm, whereas of AAC blocks 24 cm.
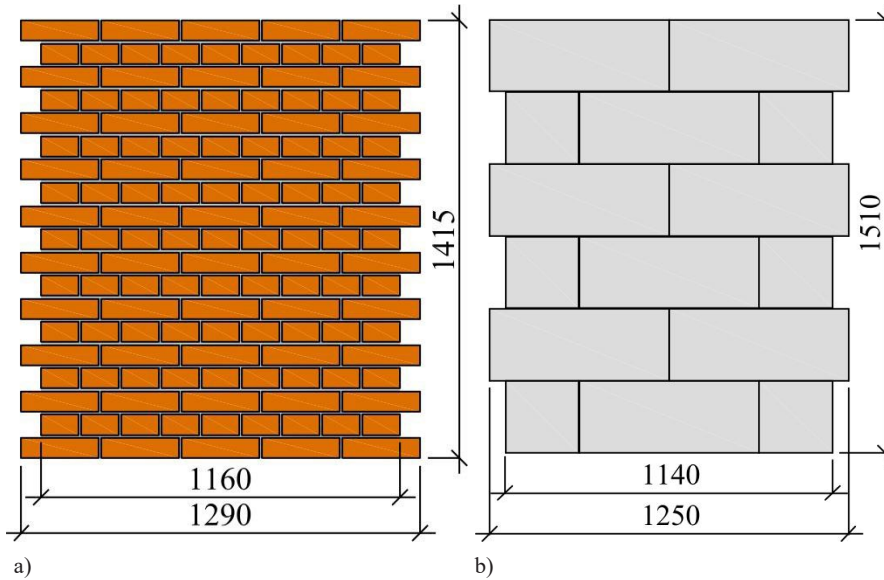
Fig. 1.   Specimens used in the tests made of: a) solid ceramic bricks, b) AAC blocks. *Source:* own study

Ten specimens made of ceramic bricks and five specimens made of AAC blocks were tested. The specimens were divided into groups depending on the values of compressive stresses normal to the masonry bed joints plane σ_c that accompanied the vertical displacements and shear in this direction. The specimens were tested without the participation of σ_c stress and at four compressive stress values in the case of ceramic bricks specimens and with $\sigma_c = 0.9$ N/mm^2 for AAC blocks specimens. Tab. 1 lists individual test series with their symbols, values of compressive stresses accompanying vertical displacements and a total number of specimens.

Table 1.   Tests programme. *Source:* own study

Ceramic solid bricks masonry		AAC blocks masonry	
Specimen	Compressive stress σ_c, N/mm^2	Specimen	Compressive stress σ_c, N/mm^2
CB-00/1	0	AAC-00/1	0
CB-00/2		AAC-00/2	
CB-03/1	0.3	AAC-00/3	
CB-03/2		AAC-09/1	0.9
CB-06/1	0.6	AAC-09/2	
CB-06/2		A total of 5 specimens	
CB-09/1	0.9		
CB-09/2			
CB-15/1	1.5		
CB-15/2			
A total of 10 specimens			

2.2. Test stand and testing technique

The tests were carried out in the specially designated test stand shown in Fig. 2. The main elements of the test stand were two external columns, the internal column through which the vertical displacements were produced by F force, horizontal ties transferring S forces, resisting members transmitting vertical R and horizontal H reactions and members for developing vertical compressive stress σ_c using N_c forces. Photograph of Fig. 3 shows the specimen monolithised with columns and prepared for a test.
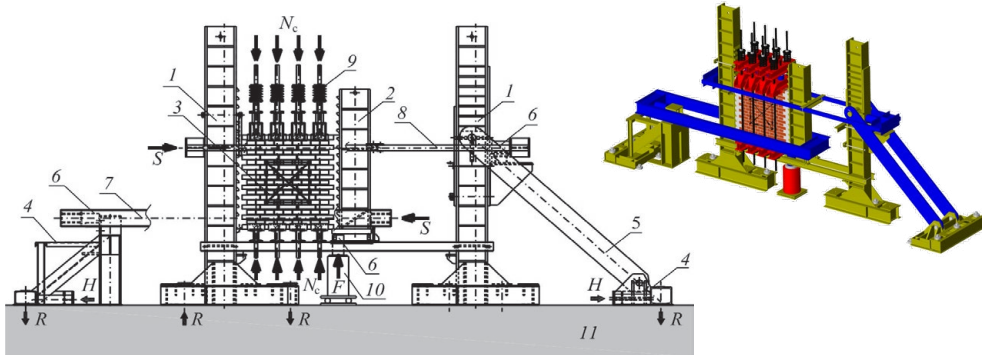
Fig. 2. Test stand: *1* – external column, *2* – internal column, *3* – masonry specimen, *4* – resisting member, *5* – tension member, *6* – load cell, *7* – lower tie, *8* – upper tie, *9* – members inducing compressive stresses, *10* – hydraulic jack, *11* – laboratory floor. *Source:* own study
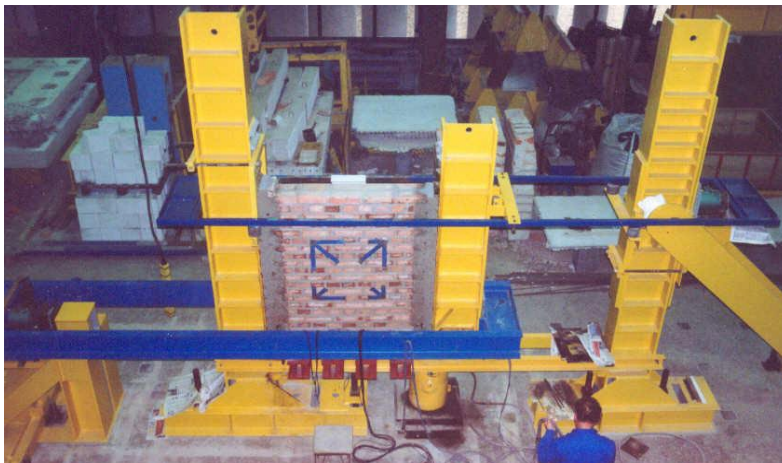
Fig. 3. Specimen made of ceramic bricks prepared for testing. *Source:* own study

The masonry specimen was monolithised with an external and internal column using concrete containing early strength gain Portland cement. Vertical displacements were induced by force F using a hydraulic cylinder and transferred to the specimen via an internal column equipped with dowels. Force F was measured by a strain gauge load cell. The vertical reaction was transferred from the specimen to the outer column also having steel dowels and further to the laboratory floor. Horizontal S-reactions were measured by means load cells, transmitted to resisting members and to the laboratory floor. Compressive stress normal to the plane of the

masonry bed joints σ_c was induced by a system of three (AAC) or four (CB) pairs of 45 mm diameter steel tendons under N_c force and equipped with springs compensating the influence of vertical wall displacements on the value and distribution of σ_c stress. Fig. 4 schematically shows the loads to the specimen was subjected to during the test and the stresses affecting the central area of the wall outside the zone of the disturbance of stress distribution.
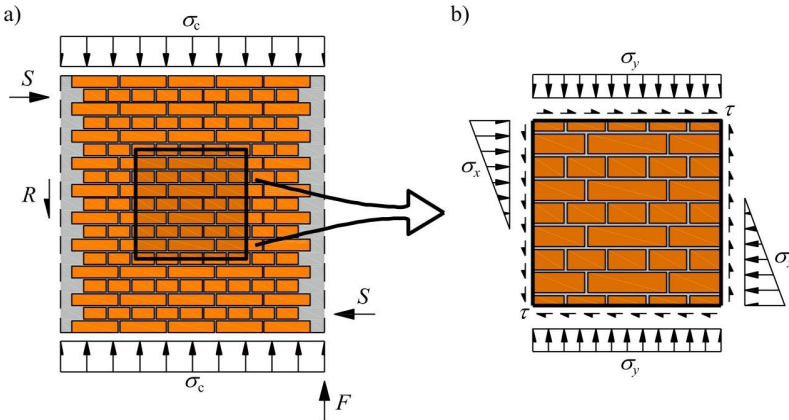
Fig. 4. Diagram of: a) external loads acting on the specimen, b) stresses in the central part of the wall. *Source:* own study

In addition to the force values, changes in the mutual position of four measuring points on the wall surface on both specimen sides were recorded during the test. Mutual dislocations of these points were determined based on the change in the length of the measurement bases, which formed a square measurement system on the faces of the specimen with a side length equal to 600 mm – Fig. 5a. Displacements were recorded using six transducers for each face of the specimen with a measurement accuracy of 0.002 mm. Values of wall deformation angles were determined on the basis of changes in the length of measurement bases according to the diagram shown in Fig. 5b. For example, the angle θ_1 was calculated from the Eq. 1, in which a_i, b_i and c_i are the lengths of the sides of the respective triangle at the i-th load level.
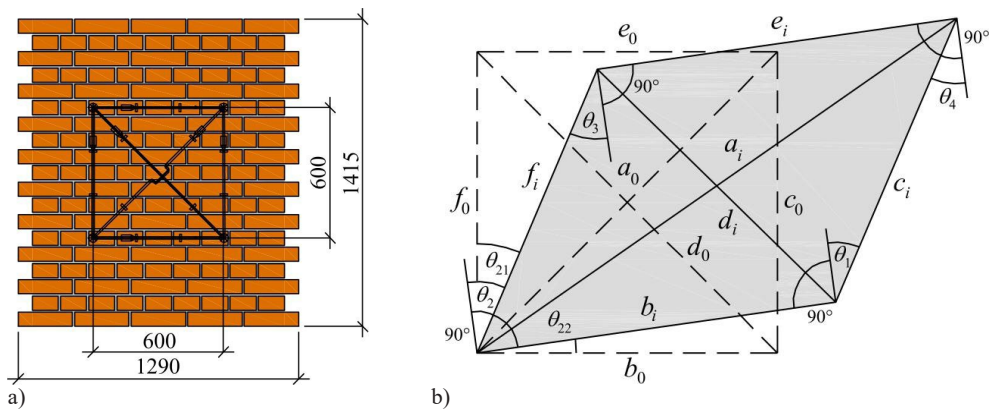
Fig. 5. Method of measuring deformations of specimens: a) square system of measuring bases equipped with displacement transducers, b) determination of deformation angles. *Source:* own study

$$\theta_1 = \arcsin\left(\frac{a_i^2 - b_i^2 - c_i^2}{2b_i c_i}\right) \tag{1}$$

The tests were carried out with a monotonic load increase until failure, i.e. a state at which it was not possible to obtain a higher value of the vertical force F.

3. Test results and discussion

Tab. 2 summarises the obtained test results, i.e. the values of shear stress accompanying the occurrence of the first crack τ_{cr} and the corresponding mean value $\tau_{cr,mv}$, ultimate shear stresses τ_u and $\tau_{u,mv}$, the ratio of mean ultimate shear stresses to shear stresses at the moment of cracking $\tau_{u,mv}/\tau_{cr,mv}$, deformation angles determined at the occurrence of cracks and accompanying the ultimate load obtained, $\theta_{cr,mv}$ and $\theta_{u,mv}$ respectively, the mean values of these angles $\theta_{cr,mv}$ and $\theta_{u,mv}$, the ratio $\theta_{u,mv}/\theta_{cr,mv}$, as well as the values of the transverse stiffness modulus D_{cr} determined on the basis of shear stresses and angles of deformation obtained at the moment of masonry cracking and corresponding mean values $D_{cr,mv}$.

The shear stress τ_i was determined as averaged at the height of the specimen by dividing the force F_i causing vertical displacements by the vertical cross-sectional area of the wall A_v. The transverse stiffness modulus D_i was calculated as the quotient of the shear stress τ_i and the corresponding deformation angle θ_i:

$$D_i = \frac{\tau_i}{\theta_i} \tag{2}$$

Table 2. Basic test results. *Source:* own study

Ceramic solid bricks masonry

Specimen	σ_c, N/mm²	τ_{cr}, N/mm²	$\tau_{cr.mv}$, N/mm²	τ_u, N/mm²	$\tau_{u.mv}$, N/mm²	$\tau_{u.mv}/\tau_{cr.mv}$	θ_{cr}, mm/m
CB-00/1	0	0.568	0.582	0.683	0.656	1.13	0.378
CB-00/2		0.569		0.628			0.344
CB-03/1	0.3	0.776	0.799	0.942	0.940	1.18	0.386
CB-03/2		0.822		0.937			0.362
CB-06/1	0.6	0.905	0.919	1.24	1.21	1.32	0.545
CB-06/2		0.933		1.18			0.576
CB-09/1	0.9	1.16	1.11	1.35	1.34	1.21	0.602
CB-09/2		1.05		1.33			0.743
CB-15/1	1.5	1.27	1.30	1.67	1.70	1.31	0.818
CB-15/2		1.33		1.73			0.934

Specimen	σ_c, N/mm²	$\theta_{cr.v}$, mm/m	θ_u, mm/m	$\theta_{u.mv}$, mm/m	$\theta_{u.mv}/\theta_{cr.mv}$	D_{cr}, N/mm²	$D_{cr.mv}$, N/mm²
CB-00/1	0	0.361	5.83	3.11	8.60	1503	1618
CB-00/2			0.381			1733	
CB-03/1	0.3	0.374	0.533	0.490	1.31	2010	2141
CB-03/2			0.446			2271	
CB-06/1	0.6	0.561	6.90	5.22	9.31	1661	1640
CB-06/2			3.54			1620	
CB-09/1	0.9	0.673	5.43	4.78	7.10	1927	1670
CB-09/2			4.12			1413	
CB-15/1	1.5	0.876	9.14	9.05	10.3	1553	1488
CB-15/2			8.96			1424	

AAC blocks masonry

Specimen	σ_c, N/mm²	τ_{cr}, N/mm²	$\tau_{cr.mv}$, N/mm²	τ_u, N/mm²	$\tau_{u.mv}$, N/mm²	$\tau_{u.mv}/\tau_{cr.mv}$	θ_{cr}, mm/m
AAC-00/1	0	0.181	0.177	0.181	0.177	1.0	0.273
AAC-00/2		0.188		0.188			0.323
AAC-00/3		0.163		0.163			0.336
AAC-09/1	0.9	0.282	0.334	0.505	0.516	1.55	0.589
AAC-09/2		0.385		0.526			0.872

Specimen	σ_c, N/mm²	$\theta_{cr.mv}$, mm/m	θ_u, mm/m	$\theta_{u.mv}$, mm/m	$\theta_{u.mv}/\theta_{cr.mv}$	D_{cr}, N/mm²	$D_{cr.mv}$, N/mm²
AAC-00/1	0	0.311	0.273	0.311	1.0	663	577
AAC-00/2			0.323			582	
AAC-00/3			0.337			485	
AAC-09/1	0.9	0.731	2.61	2.69	3.68	479	460
AAC-09/2			2.76			442	

Fig. 6 shows the relationship between shear stresses τ_i and deformation angles θ_i at various values of accompanying normal compressive stress σ_c for specimens made of ceramic bricks and AAC blocks. The graph in Fig. 7 shows the changes in the transverse stiffness modulus D_i depending on the stress value τ_i in the range from 0 to τ_{cr} at different compressive stress σ_c.

In Fig. 6, the positive effect of the compressive stress σ_c on the values of ultimate shear stress τ_u is visible. The ratio of mean stress $\tau_{u.mv}$ obtained at stress $\sigma_c = 1.5$ N/mm² to the ultimate shear stress in the case of the non-compression test was 2.59. There is also a visible change

in the nature of the wall behaviour after cracking. In the case of specimens tested without the compressive stress σ_c and ceramic brick walls sheared at $\sigma_c = 0.3$ N/mm^2, it can be observed that after cracking, the deformation angle increases sharply while shear stress decreases. At higher values of compressive stress σ_c, the quasi-plastic nature of the wall behaviour is visible. It consists in the fact that after cracking, the specimens are able to carry loads higher than those that caused the cracking, i.e. it is strengthened, while the deformation increases significantly.
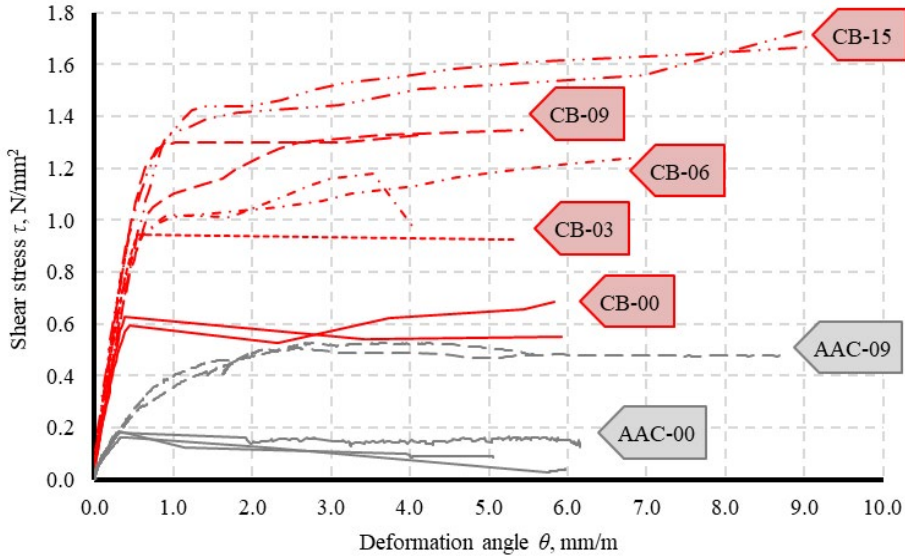
Fig. 6.   Dependence of deformation angles θ_i on the value of stresses τ_i. *Source:* own study
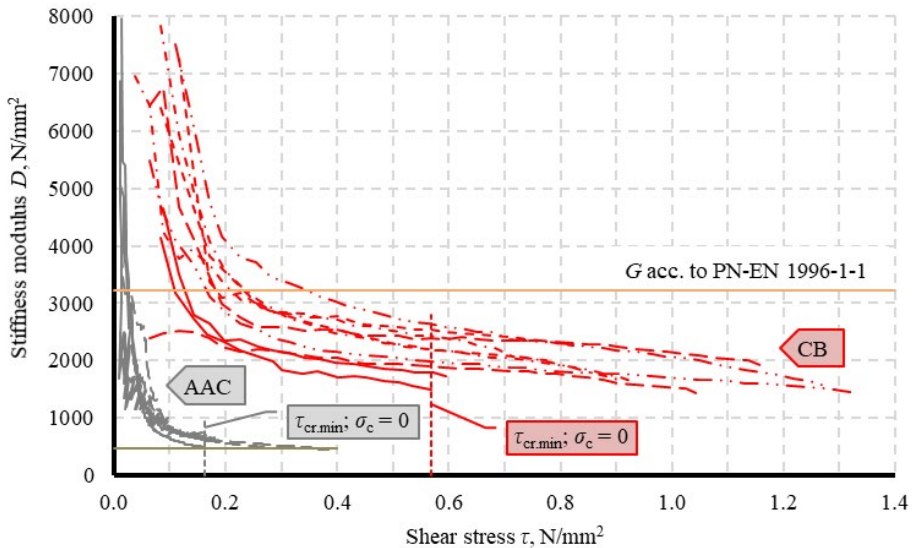
Fig. 7.   Changes in the value of transverse stiffness modulus D_i depending on the shear stress τ_i in the range $\tau_i = 0 - \tau_{cr}$. *Source:* own study

There is also a relationship between the values of compressive stress σ_c and the shear stresses τ_{cr} and angles θ_{cr} obtained at the moment of the first crack appearance. Fig. 8a shows an increase in the stress τ_{cr} as the compressive stress increases. The absolute increase in shear stress value was higher for brick walls, the difference between $\tau_{cr.mv}$ obtained at stress $\sigma_c = 0.9$ N/mm² and $\sigma_c = 0$ was 0.528 and 0.157 N/mm², respectively, for ceramic brick and AAC block walls. However, the relative increase understood as the quotient of the stress difference mentioned above and stress values $\tau_{cr.mv}$ at $\sigma_c = 0$ was about 0.90 for walls made of both types of masonry units.

Similarly, Fig. 8b shows the effect of stress σ_c on the obtained deformation angles at the moment of masonry cracking θ_{cr}. The wall was cracked with larger deformation angles, the higher the compressive stress values were. The relative increase in angles θ_{cr} obtained at $\sigma_c = 0$ and 0.9 N/mm² was about 0.86 for ceramic brick walls and 1.35 for specimens made of AAC blocks.
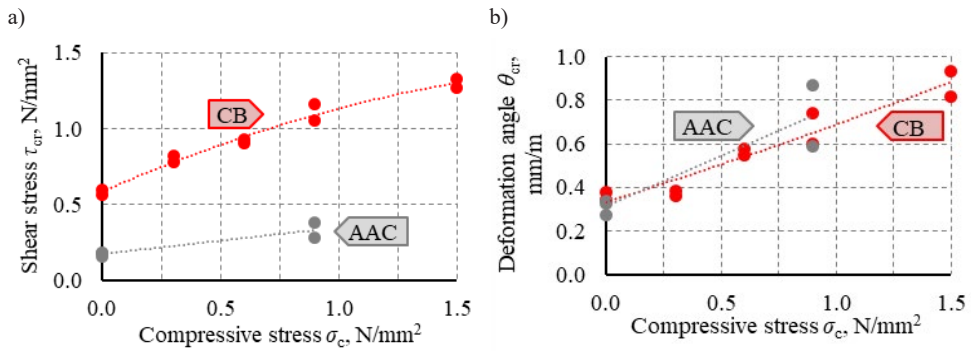
Fig. 8. The effect of compressive stress σ_c on the accompanying formation of the first cracking: a) shear stresses τ_{cr}, b) deformation angles θ_{cr}. *Source:* own study

The dependence of the transverse stiffness modulus D_i on the shear stress τ_i, as can be seen in Fig. 7, is strongly non-linear. Initially, at low stress τ_i, the stiffness decreases sharply, after which it undergoes relative stabilisation, but still shows a tendency to decrease. A much higher lateral rigidity of the walls made of ceramic bricks is visible. In the case of brick specimens, it is also possible to observe higher stiffness of the walls, which were tested with the simultaneous action of compressive stress σ_c, which was not found in the case of specimens made of AAC blocks.

On the graph shown in Fig. 7, for illustrative purposes, the values of the shear modulus G are depicted as a horizontal solid line. However, it should be remembered that shear modulus G is a material feature of the body subjected to deformations, which results in only a change in shape, without changing the volume, i.e. in the so-called simple shear case. Therefore, G modulus and the transverse stiffness modulus D discussed here are not the same parameters. Modulus G was determined for a wall made of both types of masonry in accordance with PN-EN 1996-1-1 [26], i.e.:

$$G = 0.4E, \tag{3}$$

where E is the modulus of elasticity determined according to the standard [26] as the characteristic compressive strength of the masonry f_k multiplied by the masonry elasticity coefficient

K_E equal to 1000 or 600, respectively for ceramic brick and AAC block masonry. Masonry strength f_k was also calculated using standard relationships based on normalised compressive strength of masonry units and, in the case masonry made of ceramic bricks, mean compressive strength of mortar. Modulus G was similar in value to the transverse stiffness modulus D_{cr} in the case of walls made of AAC blocks. The transverse stiffnesses of the brick walls after falling to relatively stable values, not subjected to rapid changes as the shear stress increases were lower than the value of calculated shear modulus G (see Fig. 7).

Fig. 9a is a graph depicting the values of transverse stiffness modulus obtained on the basis of the stresses and deformation angles recorded at the moment of masonry cracking D_{cr}. This modulus does not change significantly with a change in the value of compressive stress σ_c, although a slight tendency to decrease with increasing σ_c stress can be observed here. The values of D_{cr} modulus was determined based on the shear stress τ_{cr} and angles θ_{cr}, which increased with the growth of the compressive stress σ_c, therefore they do not correctly show the effect of this compression on transverse stiffness modulus D. For this reason Fig. 9b shows the values of D_i modulus determined at the smallest shear stress $\tau_{cr,min}$ occurring at the moment of masonry cracking of walls tested without compression ($\sigma_c = 0$) – see Fig. 7, which were 0.163 and 0.568 N/mm^2 in the case of specimens made of AAC blocks and ceramic bricks, respectively. As can be seen in Fig. 9b graph, the stiffness principally did not depend on the compressive stress value σ_c. However, there is an increase in the mean stiffness of ceramic brick walls tested at $\sigma_c \neq 0$ by 30 to 45% compared to the stiffness specified at $\sigma_c = 0$. For walls made of AAC blocks, this increase was only 4%.

Fig. 10 shows the pattern of the cracks of masonry specimens observed at failure for the maximum accompanying compressive stress σ_c and without compression. In the case of specimens made of ceramic bricks tested at $\sigma_c = 0$ (Fig. 10a), there are much fewer cracks, basically it is a single bifurcating crack, which mostly runs at the interface of masonry units and mortar. Stress $\sigma_c = 1.5$ N/mm^2 changed the way the masonry cracked (Fig. 10b); there are more cracks, and they run mainly through masonry units. Specimens made of AAC blocks tested without compressive stresses failed as it is shown in Fig. 10c, i.e. a single diagonal crack was created, which due to the proportions of masonry units mainly ran diagonally through the blocks. In the case of specimens tested at stress $\sigma_c = 0.9$ N/mm^2, many cracks and detachments of material appeared on the outer surface of the masonry blocks (Fig. 10d). The direction of the cracks was much closer to vertical.
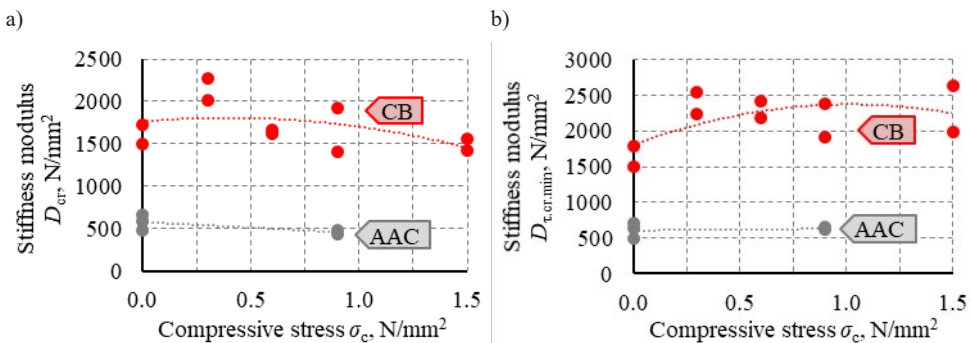
Fig. 9.   Influence of compressive stress σ_c on the values of transverse stiffness modulus: a) at shear stresses τ_{cr} proper for each specimen, b) at shear stresses τ_{cr} lowest in the group of specimens made of bricks and AAC blocks. *Source:* own study
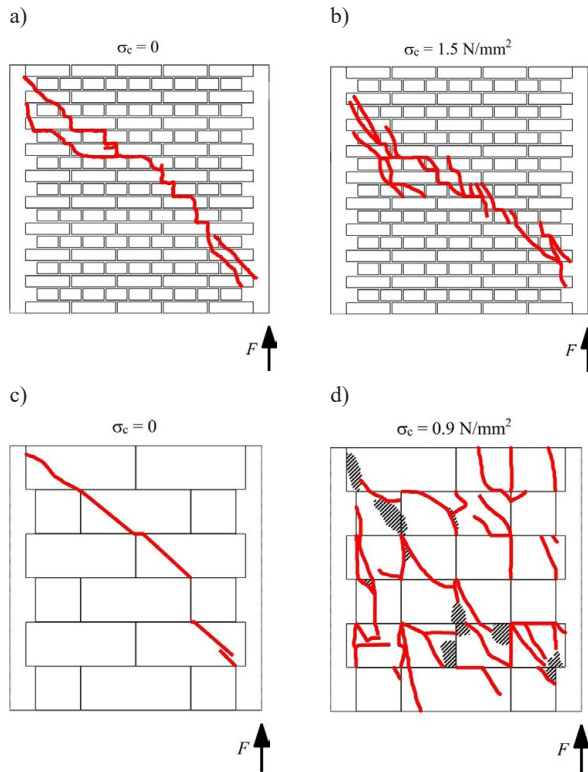
Fig. 10.   Cracks pattern at the failure of masonry specimens made of: a), b) ceramic bricks, c), d) AAC blocks.
Source: own study

4. Conclusions

Based on the tests carried out in the scope described above, the following conclusions can be made:

- The nature of the dependence of the deformation angle θ_i on the shear stress τ_i was determined by the values of compressive stresses normal to the plane of masonry bed joints σ_c. At low values of σ_c or in its absence, the brittle nature failure was observed. At stresses $\sigma_c \geq 0.6$ N/ mm², the quasi-plastic behaviour was visible with hardening in the phase after masonry cracking;
- The increase in compressive stress value σ_c meant that the first crack occurred at higher values of shear stress τ_{cr} and deformation angle θ_{cr};
- Compressive stresses σ_c had a positive effect on the load-bearing capacity of masonry sheared due to vertical displacements;
- The dependence of the transverse stiffness modulus on the value of shear stress was strongly non-linear. After the initial rapid decrease in stiffness, its further degradation was significantly slowed down;
- The transverse stiffness modulus of the masonry determined at the moment of first cracking D_{cr} did not change considerably with increasing stress σ_c;

- The compressive stress σ_c increased the transverse stiffness of the ceramic brick masonry D_i compared to the stiffness of the masonry determined at $\sigma_c = 0$ by 30 to 45%. No such relation was observed in the case of walls made of AAC blocks.

References

[1]　Piekarczyk A., "Shear stiffness of solid clay brick wallets sheared perpendicularly to the masonry bed joints", *Procedia Engineering*, vol. 161, 2016, pp. 1064-1069. https://doi.org/10.1016/j.proeng.2016.08.849

[2]　Piekarczyk A., "Uszkodzenia i naprawy niekonstrukcyjnych elementów budynków", in *XXX Jubileuszowe Ogólnopolskie Warsztaty Pracy Projektanta Konstrukcji*. Polski Związek Inżynierów i Techników Budownictwa. Oddział w Bielsku-Białej, vol. 3, Szczyrk, 2015, pp. 233-290.

[3]　Piekarczyk A., "Shear modulus and non-dilatational strains of unreinforced and reinforced clay brick masonry", in *8th International Masonry Conference*, Dresden, 2010, pp. 315-324.

[4]　Drobiec Ł., "Przyczyny uszkodzeń murów", in *XXII Ogólnopolska Konferencja Warsztat Pracy Projektanta Konstrukcji*. Polski Związek Inżynierów i Techników Budownictwa. Oddział w Bielsku-Białej, vol. 1, Szczyrk, 2007.

[5]　Kubica J., *Niezbrojone ściany murowane poddane odkształceniom postaciowym wywołanym nierównomiernymi pionowymi przemieszczeniami podłoża*. Wydawnictwo Politechniki Śląskiej, Gliwice 2003.

[6]　Małyszko L., Orłowicz R., *Konstrukcje murowe. Zarysowania i naprawy*. Wydawnictwo Uniwersytetu Warmińsko-Mazurskiego w Olsztynie, Olsztyn 2000.

[7]　Masłowski E., Spiżewska D., *Wzmacnianie konstrukcji budowlanych*. Wydawnictwo „Arkady", Warszawa 2002.

[8]　Rudziński L., *Konstrukcje murowe. Remonty i wzmocnienia*. Wydawnictwo Politechniki Świętokrzyskiej, Kielce 2006.

[9]　Stawski B., *Konstrukcje murowe. Naprawy i wzmocnienia*. Polcen Sp. z o.o., Warszawa 2014.

[10]　Piekarczyk A., "Comparative investigations of unreinforced and reinforced masonry walls subjected to vertical shearing", in *II International Scientific Conference – Quality and Reliability in Building Industry*, Levoča, 2001, pp. 424-429.

[11]　Piekarczyk A., Kubica J., "Capacity and deformability of vertically sheared clay brick masonry with horizontal reinforcement", in *Proceedings of the British Masonry Society. Proceedings of the Sixth International Masonry Conference, Proceedings No. 9*, London, 2002, pp. 386-391.

[12]　Jasiński R., Piekarczyk A., "Cracking of clay brick masonry wallets sheared parallel and perpendicular to the bed joints – a trial of the problem description", in *III International Scientific Conference – Quality and Reliability in Building Industry*, Levoča, 2003, pp. 244-250.

[13]　Jasiński R., Piekarczyk A., "Próba opisu zjawiska cinania w kierunku równoległym i prostopadłym do spoin wspornych niezbrojonych murów ceglanych", in *XLIX Konferencja Naukowa Komitetu Inżynierii Lądowej i Wodnej PAN i Komitetu Nauki PZITB, Warszawa – Krynica*, 2003, vol. 4, pp. 139-147.

[14]　Kubica J., Piekarczyk A., "Tests of vertically sheared clay brick masonry walls with and without bed joint reinforcement", in *Proceedings of 13th IB²MaC*, Amsterdam, 2004, pp. 191-200.

[15]　Piekarczyk A., *Nośność i odkształcalność zbrojonych ścian murowych poddanych ścinaniu w kierunku pionowym*. Politechnika Śląska [praca doktorska], Gliwice, 2005.

[16]　Kubica J., "Reinforced masonry shear walls – application, design and research problems", in *Analytical models and new concepts in concrete and masonry structures AMCM'2008, 6th International Conference*, Łódź, 2008, pp. 43-57.

[17]　Kubica J., Piekarczyk A., *Investigations of reinforced (with "Murfor" reinforcement situated in bed joints) masonry walls made of AAC blocks "Ytong" type subjected to vertical shearing. Chapter 4.*

Main investigations – masonry wallettes subjected to vertical shearing. Research report NB-227/RB-8/2008. Silesian University of Technology, Gliwice 2008.

[18] Kubica J., "In-plane sheared unreinforced masonry wallettes – proposition of failure criterion", in *Proceedings of 15th IB²MaC*, Florianópolis, 2012, pp. 191-200.

[19] Drobiec Ł., Jasiński R., Piekarczyk A., *Konstrukcje murowe według Eurokodu 6 i norm związanych*. PWN, vol. 1, Warszawa, 2013.

[20] Kubica J., "Size and shape effect of test specimens on shear of clay brick and AAC block masonry – a comparative study" in *9th International Masonry Conference*, Guimaraes, 2014, p. 192.

[21] Kubica J., "Unreinforced clay brick masonry wallettes sheared perpendicular or parallel to the bed joints – a comparative study", in *16th International Brick and Block Masonry Conference. Trends, innovations and challenges*. CRC Press-Taylor & Francis Group, Padova, 2016, pp. 1683-1690.

[22] Piekarczyk A., "The Influence of Compressive Stress on the Load-Bearing Capacity of Masonry Subjected to Vertical Displacements", in *3rd World Multidisciplinary Civil Engineering –Architecture – Urban Planning Symposium, WMCAUS 2018*, IOP Conference Series: Science and Engineering, vol. 471, Prague, 2019.

[23] Lurati F., Graf H., Thürlimann B., *Experimental determination of the strength parameters of concrete masonry, Report No 8401-2*. Institute of Structural Engineering, Zürich 1990.

[24] Raijmakers T. M. J., Vermeltfoort A. J., *Deformation controlled tests in masonry shear walls, Report B-92-1156*. TNO-Bouw, Delft 1992.

[25] Tsui T. P., "A preliminary investigation of the vertical shear strength of brick masonry", in *6th International Brick/Block Masonry Conference*, Rome, 1982, pp. 33-44.

[26] PN-EN 772-1 Metody badań elementów murowych. Część 1: Określenie wytrzymałości na ściskanie.

[27] PN-EN 998-2 Wymagania dotyczące zapraw do murów. Część 2: Zaprawa murarska.

[28] PN-EN 1996-1-1 Eurokod 6. Projektowanie konstrukcji murowych. Część 1-1: Reguły ogólne dla zbrojonych i niezbrojonych konstrukcji murowych.

Orginal Article

Mechanical performance of FRP-RC flexural members subjected to fire conditions

Kostiantyn Protchenko[1], Elżbieta Szmigiera[2], Marek Urbański[3], Andrzej Garbacz[4]

[1] Warsaw University of Technology, Faculty of Civil Engineering, 16 Armii Ludowej av., 00-637 Warsaw, Poland; k.protchenko@il.pw.edu.pl ID 0000-0003-1357-2174
[2] Warsaw University of Technology, Faculty of Civil Engineering, 16 Armii Ludowej av., 00-637 Warsaw, Poland; e.szmigiera@il.pw.edu.pl ID 0000-0001-9084-2372
[3] Warsaw University of Technology, Faculty of Civil Engineering, 16 Armii Ludowej av., 00-637 Warsaw, Poland; m.urbanski@il.pw.edu.pl ID 0000-0002-3568-6888
[4] Warsaw University of Technology, Faculty of Civil Engineering, 16 Armii Ludowej av., 00-637 Warsaw, Poland; a.garbacz@il.pw.edu.pl ID 0000-0002-5229-7884

Abstract: One of the main concerns that limit the widespread use of Fibre-Reinforced Polymers (FRP) bars as internal reinforcement for reinforced concrete (RC) structures is their relatively unexplored response to elevated temperatures. The behaviour of FRP reinforcement at elevated temperature as well as their post-fire behaviour can be different from conventional reinforcement and depends on the properties of the constituents of the bars. Therefore, the fire resistance of FRP-RC structures is an important issue that needs careful investigation before FRP reinforcement can be implemented in RC structures.

The experimental results for full-scale FRP-RC beams subjected to specific fire action were presented and discussed in this paper. The specimens were exposed to heat in the mid-section from below (tension zone) and from the sides. As one of the main aims was to examine the influence of different reinforcement configurations, the testing was made for concrete beams reinforced with three different types of FRP bars: (i) basalt-FRP (BFRP), (ii) hybrid FRP with carbon and basalt fibres (HFRP) and (iii) nano-hybrid FRP (nHFRP), with modification of the epoxy matrix of the rebars.

The present work describes the behaviour of FRP-RC beams exposed to fire conditions and simultaneous loading (50% of their ultimate strength capacity at normal temperature) and unloaded beams were tested after the cooling phase in order to evaluate their residual resistance.

Present work shows that the type of FRP bars used has a direct influence on the outcomes and the way of destruction. The maximum ductility, the longest heating time of approximately 100 minutes, was obtained for beams reinforced with BFRP bars and attained deflections were corresponded to the value of 162 mm.

1. Introduction

Implementing Fibre-Reinforced Polymers (FRP) bars as an alternative solution to traditional methods of reinforcing has become an extremely interesting issue from both theoretical and practical perspectives. FRP bars are attractive due to their advantageous properties such as durability in environments subjected to heavy corrosion, low weight while maintaining, or adequate stiffness and stability. Progress in manufacturing technology has introduced new types of FRP bars, and furthermore different hybrid FRP (HFRP) types that contain several types of reinforcing constituents and/or several types of adhesive constituents in a matrix. An important feature of HFRP bars is that the combination of its constituent allows for adjustment of their properties to a desirable design situation.

Nevertheless, the employment of FRP bars as internal reinforcement for reinforced concrete (RC) structures still poses many challenges. The bond behaviour of FRP reinforcement varies from conventional rebar due to the anisotropy of the material and a different surface texture than that of steel. In addition, FRP reinforcement displays linearly elastic behaviour up to its failure when subjected to tensile forces [1]. Other issues include a lower modulus of elasticity (for certain types) and brittle mode of failure [2]. This causes FRP bars to break without significant bending of the element, so this mode of failure is un-signalized [3]. However, some authors suggest that hybridization can partially solve this issue by changing the behaviour of FRP-RC members, making it semi-ductile instead of linear [4], [5].

The mechanical performance of FRP-RC structures is already known at ambient temperatures. One of the major issues that hinder the extensive use of FRP reinforced members is their low fire resistance, which is of high importance since building structures must satisfy the requirements of building codes, which relate to the behaviour of those structures in a fire. Fire ratings for buildings refer to the amount of time a structure can be exposed to fire before the structure collapses [6], [7]. Fire resistance of FRP-RC structures, particularly, is a multifaceted issue that considers many influencing factors, such as the critical temperature for a certain type of FRP bars, fire scenario, clear concrete cover, aggregates used for concrete mixture, etc.

The data available from standards on the behaviour of FRP, and particularly HFRP bars, at elevated temperature are scarce. ACI committee ACI 440.1R-15 [8] describes the material characteristics needed to design the minimum reinforcement regarding temperature and shrinkage thresholds. The Canadian code CAN/CSA S806-12, Annex R for slabs [9] provides a design procedure in a fire situation based on critical temperatures related to the FRP bars [10]. However, the aforementioned standards are related mainly to the most prevalent and commercially available FRP bars and do not consider hybrid bars.

In addition, several mechanical and physical characteristics of FRP bars make designing structures with FRP reinforcement different from conventional RC design in regard to fire resistance aspects [11]. Abassi and Hogg [12] performed fire tests on concrete beams reinforced with Glass-FRP (GFRP) bars with a concrete cover of about 70 mm. The beams attained fire endurance

for longer than 90 min. Therefore, a minimum concrete cover of 70 mm was recommended for design of GFRP-RC beams under fire action.

Furthermore, the literature provides experimental results from failure tests performed on FRP reinforced concrete slabs [13]–[16] and beams [12], [17] working in flexure that were exposed in most of the cases to conventional fire conditions, e.g. simultaneous loading and heating. The outlined literature shows a need for further research regarding the post-fire behaviour of FRP-RC structures [17]. Nigro at al. [14] investigated the residual strength capacity for slabs reinforced with GFRP bars. Two unloaded slabs after heating attained deflections of approximately 70 mm due to their own weight and thermal strains, and their residual resistance evaluated after the cooling phase were about 55% to 100% of the ultimate design bearing moment resistance. Moreover, it was stated that the typical values of concrete clear cover (i.e. between 30 and 50 mm) can be adopted.

As it is suggested in the literature, the behaviour of FRP reinforcement at elevated temperatures can be different from the conventional reinforcement and depends on the glass transition temperature of the resin. When the temperature in the resin reaches this point, it no longer becomes possible to redistribute the stresses along fibres. However, the fibres continue to withstand loading till the next threshold at which fibres begin to degrade, which is the point of failure of the structure [18]. Nevertheless, the critical temperature of FRP bars remains unknown for most of the currently available FRP-reinforcing products [14].

This study investigates the behaviour of FRP-RC beams subjected to specific fire actions, where the midsection, approximately 1/3 of the length of the beams, was exposed to heating from both the bottom and sides. The experimental procedure consisted of two different cases, some samples were exposed to fire conditions and simultaneous loading (50% of their ultimate strength capacity at normal temperature), and for the rest of samples the residual resistance was estimated, i.e. beams were subjected to heating for approximately one hour and then unloaded. Once cooled, the beams were tested until failure. The reference beams for both cases were tested to examine the mechanical properties of the beams and compare them with the beams after being subjected to elevated temperatures.

The results of investigations were discussed with a particular emphasis on the structural behaviour of the concrete members and the types of FRP bars used.

2. Hybrid and nano-hybrid FRP bars

In the context of this work, the term "Hybridization" might be understood as a physical substitution of a part of fibres by another type. The proposed constituents for the hybrid bars: carbon and basalt fibres, were embedded in epoxy resin creating HC/BFRP (HFRP) bars. Processing HFRP bars is analogous to the process of producing Basalt-FRP (BFRP) bars where a certain amount of the basalt roving is replaced with carbon roving during the pultrusion process.

Prior to creating the HFRP bars, several parameters of the proposed HFRP bars were estimated, including the location of fibres, technological aspects, and the volume-fraction ratios of fibres. With that aim, the numerical and analytical considerations were made.

The properties of FRP bars in the longitudinal direction can be calculated using the Rule of Mixtures (ROM) (axial loading – Voigt model) [19]–[21]. The transverse properties can be obtained with Halpin-Tsai and other semi-empirical models [22], [23]. However, these models do not consider bars configuration, i.e. location of fibres, so, it was suggested to perform a numerical simulation.

The numerical simulation of tensile strength test for HFRP bars was performed by Finite Element Analysis (FEA) in the software ANSYS® Academic Research Mechanical, Release 16.2 [24]. Two different bar configurations were proposed, one where carbon fibres were substituting basalt fibres in the core region, the other one with carbon fibres located in the near-surface region. In addition, different volume fractions were used to estimate their influence on the mechanical properties of HFRP bars.

The results showed that bar configuration is less important than the volume fraction of fibres. The difference between various bar configurations was shown to be a maximum of 2%. Meanwhile, the volume fraction of all analyzed combinations can influence the final stiffness by 74.6%.

Several technological issues were observed while placing the carbon fibres located in the near-surface region, such as increased heterogeneity in fibre locations and local scorching of the bars caused by temperature increases. Consequently, the appropriate location of carbon fibres is in the core region of the HFRP rebar.

As it is suggested in the literature, the addition of nano silica particles into the epoxy resin can improve the general performance of a composite material [25]–[27]. Therefore, it was decided to elaborate nano-Hybrid FRP (nHFRP) bars as well. A modified epoxy resin with a four-component 1300 System® was used, which is dedicated to the manufacturing of composite materials using the pultrusion method. The sol with the nano silica particles with a concentration of 25 to 30% by weight was used. The average diameter of particles was equal to 24.7 nm, containing two fractions: fine (80%) and coarse (20%).

A more detailed description of HFRP and nHFRP development is provided in the companion papers [28]–[31].

3. Materials and experimental programme

The experimental programme encompasses the design and fabrication of nine FRP reinforced concrete beams without any fire protection system. The investigation consisted of two different cases, Group 1 – standard fire resistance testing, the beams were subjected to loading and heating at the same time till the failure (50% of their ultimate strength capacity at normal temperature); Group 2 – residual fire resistance testing, the beams were heated for a period of approximately one hour and then loaded till failure.

In addition, both groups were divided into two sets: set 1 with the tested beams and set 2 as reference beams. Sets 1 for both groups were preliminarily loaded, applying a gradual force until 50% of their ultimate strength capacity, and then unloaded to simulate realistic conditions, i.e. appearance of cracks. Beams from set 2 were tested with four-point flexural tests without preliminary loading and were not exposed to elevated temperatures. Table 1 shows the description of the specimens used in the tests depending on the set.

Table 1. Descriptions of the Specimens. *Source:* own study

Set No.	Beam designation*	Reinforcement type (tension zone)	Preliminary loaded (50% of ultimate load)
		[Items / Ø / Type]	[kN]
GROUP 1 – Standard fire resistance testing & GROUP 2 – Residual fire resistance testing			
1	B2Ø14	2 / 14 / BFRP	30
	H2Ø14	2 / 14 / HFRP	40
	N2Ø14	2 / 14 / nHFRP	40
2 (reference samples)	B2Ø14	2 / 14 / BFRP	0
	H2Ø14	2 / 14 / HFRP	0
	N2Ø14	2 / 14 / nHFRP	0

* B – reinforced with BFRP bars; H – reinforced with HFRP bars; N – reinforced with FRP bars

All specimens had the same section dimensions: 140 mm wide, 260 mm high and were 3200 mm long. The clear cover was equal to 30 mm from all sides for all tested specimens.

The beams were reinforced solely with FRP bars, three different types of FRP bars were used for the tensile zone: (i) BFRP, (ii) HFRP and (iii) nHFRP bars; reinforcement ratio 0.98% was constant for all samples. The compression zone and shear reinforcement were kept constant for all the beams and were reinforced with two BFRP bars with diameters of 8 mm. The stirrups were made of BFRP with a diameter of 6 mm and spacing of 100 mm for all the beams. The stirrups for the mid part were omitted to simulate clear bending. Figure 1 shows the scheme of tested specimens.
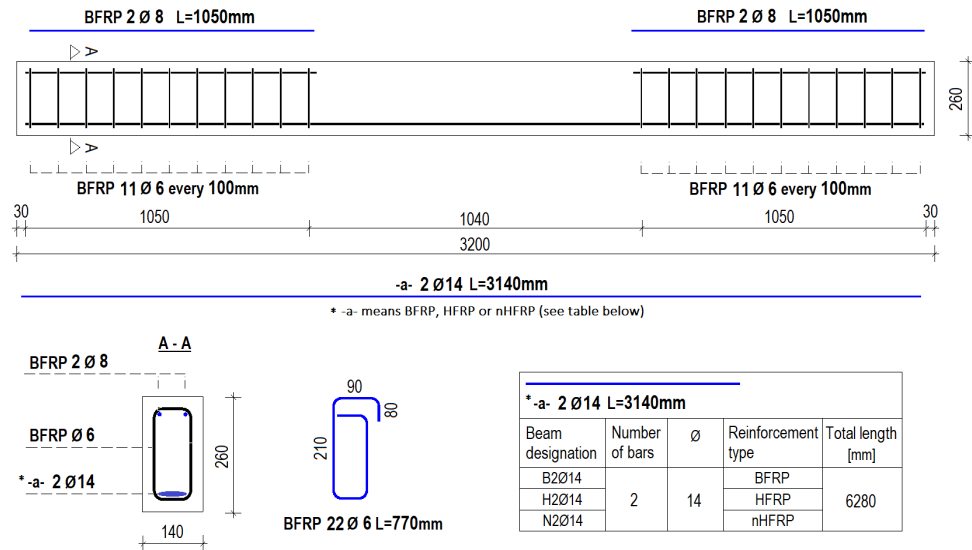
Fig. 1. Schematic details of beam specimens. *Source:* own study

3.1. Materials utilized for the work

3.1.1. Concrete

The concrete mixture was the same for all beams: a typical concrete mix C40/45 was used. Ordinary Portland cement CEM III/A, ash, and crushed stone (silica) with a nominal maximum size of 16 mm were used in concrete mixes.

3.1.2. Reinforcement

A more detailed description for choosing the configuration of the bars and their characteristics are reported in the following companion papers [28]–[31]. The mechanical properties for BFRP, HFRP and nHFRP, obtained experimentally from tensile testing, are shown in Tab. 2.

Table 2.   Mechanical properties of FRP bars. *Source:* own study

Type of bars	Maximum tensile force	Tensile strength	Tensile strength at rupture	Modulus of elasticity
Type / Dia	F_u [kN]	f_u [MPa]	ε_u [%]	E_{11} [GPa]
BFRP Ø6	37.07	1148.81	2.48	46. 47
BFRP Ø8	60.03	1103.30	2.52	43.87
BFRP Ø14	179.26	1101.94	2.39	46.02
HFRP Ø14	206.57	1160.06	1.61	72.12
nHFRP Ø14	150.54	958.00	1.58	60.44

3.2. Test setup

In order to monitor the temperature distribution, deflections and possible stretching, the beams were instrumented with thermocouples in different locations (in concrete at different depths and sections and on the bars' surface) and dial gauges (on the top side and on edges).

The furnace was located around the central part of the beam and heated 1/3 of the beam length. The heating was applied from the bottom and sides. The gaps between the furnace and the beam were insulated with ceramic and rock wool. Heating was applied in accordance with standard heating curve ISO-834 (1999) [32].

The Fig. 2 demonstrates the test setup and instrumentation of the beams.
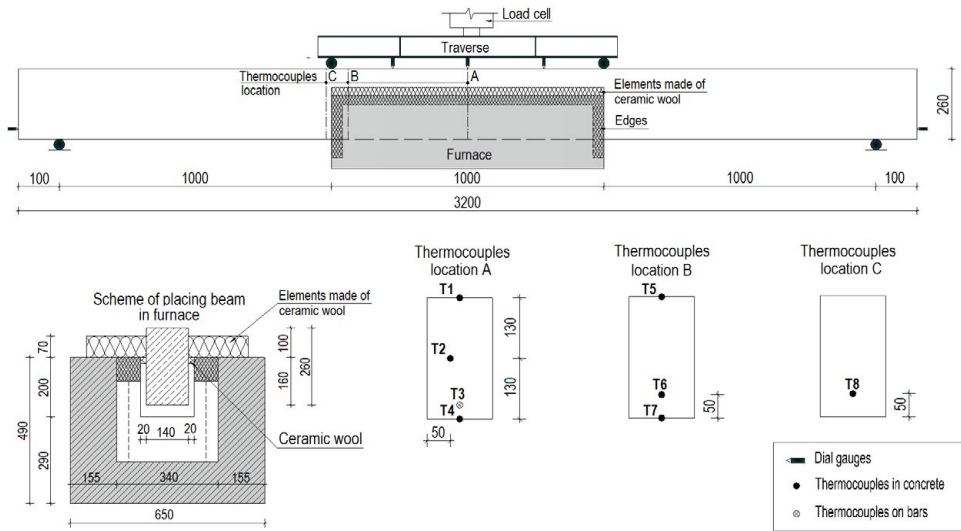
Fig. 2.   Test setup description and instrumentation of the beams. *Source:* own study

3.3. **Standard fire resistance testing**

In the case of standard fire resistance testing, three beams of Set 1 were first loaded in the four-point flexural test with a gradual force till 50% of their ultimate strength capacity, then unloaded before being heated. The values of loading are shown in Tab. 1. Then, the beams were reloaded with sustained loading providing a bending moment that corresponds to 50% of ultimate bending moment resistance of the beams (at ambient temperature), and heating was applied. Beams were loaded and heated till failure. Set 2 was used as a reference to calculate the loading that the beams can withstand.

Beams of Set 1 were destroyed in different ways, the B2Ø14 was destroyed due to reinforcement failure, and both other beams reinforced with hybrid bars were destroyed due to concrete crushing. All the beams of the Set 2 were destroyed due to concrete crushing.

The deflections against heating duration are shown on the Fig. 3. The maximum time of fire exposure, 97 minutes, was achieved by the sample B2Ø14, once the deflection at the midspan attained a value $U_{B2Ø14} = 162$ mm. The temperature recorded on the bottom side was approximately 940°C and 593°C, measured directly on the bars. The displacements for the beams reinforced with hybrid bars were approximately 70 mm
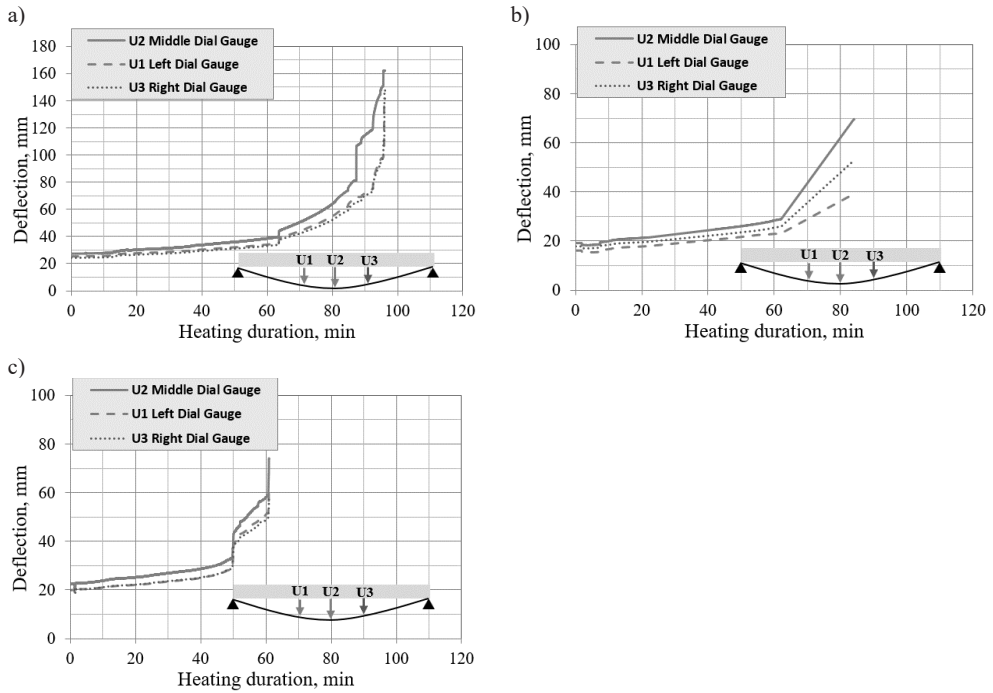
Fig. 3.   Deflection – heating duration dependencies for samples (Group 1): a) B2Ø14, b) H2Ø14, c) N2Ø14.
Source: own study

When the concrete cover was removed from samples H2Ø14 and N2Ø14, it could be seen that the resin evaporated from the bars. Moreover, it is visible that the temperature caused a de-bonding of the bars from the concrete. Figure 4 demonstrates the beam H2Ø14 after removing clear concrete cover.

Fig. 4.   Uncovered HFRP bars (by removing the clear cover after testing). *Source:* own study

3.4. Residual fire resistance testing

For residual testing, the beams of Set 1 were preliminarily loaded with a force of 50% of their ultimate strength capacity. Then the beams were unloaded. For the following steps, the beams were placed into a furnace and heated for approximately one hour. After heating, the beams were allowed to cool, and finally reloaded flexurally until failure. Figure 5 demonstrates the beam sample B2Ø14 from Set 1 just after it was taken out of the furnace.
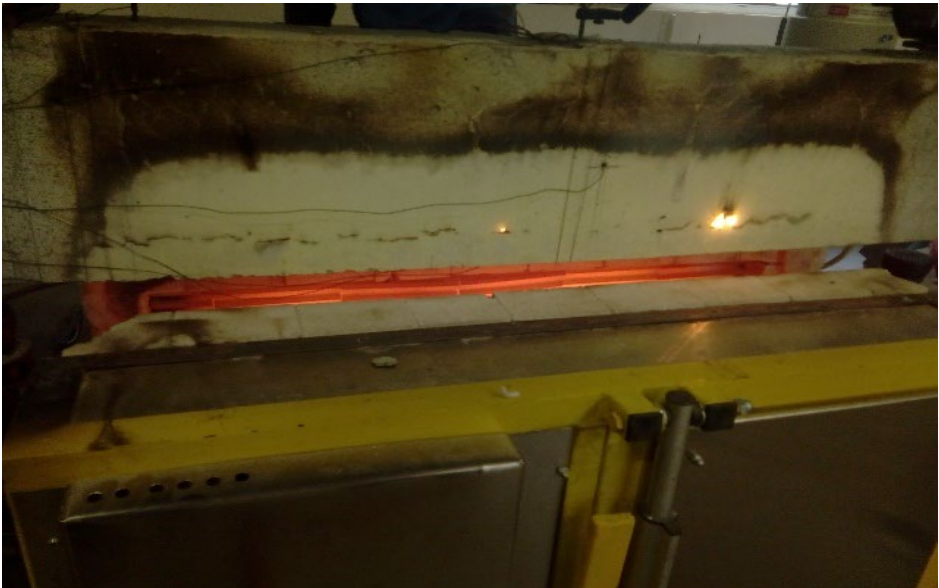
Fig. 5.   Sample B2Ø14 just after taking it out from the furnace. *Source:* own study

All the specimens from Set 1 were destroyed due to reinforcement failure in the tension zone, unlike beams from Set 2, where destruction took place due to concrete crushing. The authors suggest that different manners of destruction can be explained by a significant reduction in the properties of the bars after being subjected to elevated temperatures.

The evaluated resistance for beams from Set 1 after being subjected to elevated temperatures was 43.39%, 40.34%, and 43.42% lower for the beams B2Ø14; H2Ø14 and N2Ø14, respectively, from Set 2 (reference beams).

Moreover, atypical behaviour of FRP-RC beams was observed while heating unloaded beams. The deflections for the beams reinforced with HFRP and nHFRP bars began to decrease after reaching a certain temperature threshold. The temperatures, measured on HFRP and nHFRP bars, were in the range of 550–570ºC. Fig.6 demonstrates deflection – heating time dependencies for the beams subjected to residual testing.
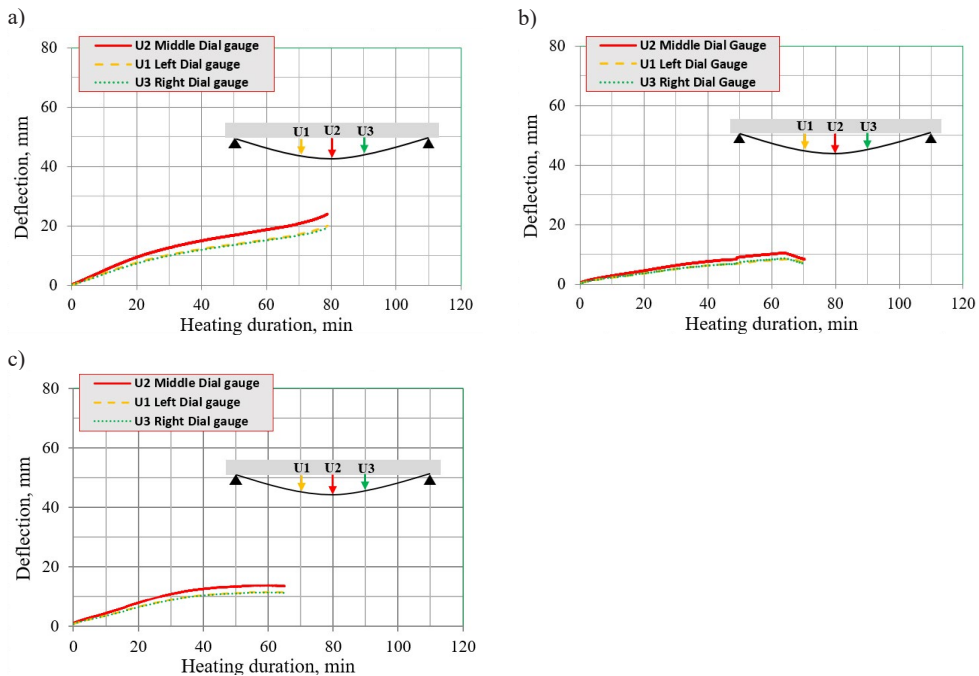
Fig. 6.   Deflection – heating duration dependencies for samples (Group 2): a) B2Ø14, b) H2Ø14, c) N2Ø14.
    Source: own study

4. Conclusions

The main focus of this research was the experimental investigation of the behaviour of FRP-RC beams subjected to elevated temperatures, reflecting conditions of fire and post-fire performance of FRP-RC beams. The beams were subjected to a specific fire scenario, where the mid-part was heated.

Two cases were analyzed: (i) standard fire conditions, where loaded beams are subjected to heating and simultaneously loaded and (ii) residual behaviour of FRP-RC beams, after being subjected to elevated temperatures.

The following conclusive remarks can be drawn:

1. Based on the maximum heating time and deflections, the best-recorded results were obtained for the samples reinforced with BFRP bars. For standard fire resistance testing, BFRP-RC beams show the longest heating time (approximately 100 min) and attained the highest deflections, corresponding to the value 162 mm.

2. Different destruction modes were observed for beams reinforced with BFRP bars and beams reinforced with hybrid bars after standard testing; for the BFRP-RC structures, the destruction was caused by a failure in the tensile zone, unlike in the other samples from Group 1 – standard testing

3. The residual capacity for the beams after being subjected to the fire exposure, decreased by approximately 40% compared to Set 2. The highest strength capacity was obtained by beams reinforced with HFRP bars and was equal to 50.71 kN. It is worth mentioning that the post-fire behaviour of FRP-RC beams was similar as for beams not subjected to fire exposure until failure as it can be seen from the force-deflection curves.

4. Different ways of destruction, all the tested specimens from Set 1 were destroyed due to tension zone failure, unlike beams from Set 2. This can indicate a reduction of mechanical properties of FRP bars after being subjected to elevated temperatures.

5. It should be noticed that very uncharacteristic behaviour was recorded for the beams reinforced with HFRP and nHFRP bars. The authors suggest that this phenomenon is connected with the thermal expansion coefficient of the carbon fibres present in HFRP and nHFRP bars and therefore creep can appear in the bars, which causes an effect of "prestressing" of the beams.

It is worth mentioning that for a comprehensive investigation, it is needed to make more sophisticated analyses of a bigger number of samples with different fire scenario in order to receive more representative results. Current experimental work will serve to develop a program for FRP-RC members tested at and after being subjected to elevated temperatures.

References

[1]   Portnov G., Bakis C.E., Lackey E., Kulakov V., "FRP Reinforcing bars – designs and methods of manufacture (Review of Patents)", *Mechanics of Composite Materials*, vol. 49, no. 4, (2013), pp. 381-400. https://doi.org/10.1007/s11029-013-9355-1

[2]   Castro F., Protasio, Carino N., "Tensile and Nondestructive Testing of FRP Bars", *Journal of Composites for Construction*, vol. 2, no. 1, 1998, pp. 17-27. https://doi.org/10.1061/(ASCE)1090-0268(1998)2:1(17)

[3]   Palmieri A., Matthys S., and Tierens M. "Basalt fibres: Mechanical properties and applications for concrete structures." in *Concrete solutions : proceedings of the international conference on Concrete Solutions*. Taylor and Francis Group, 2009, pp.165-169.

[4]   Garbacz A., Radomski W.A., Mossakowski P., "Alternatywne zbrojenie betonu kompozytami FRP – zagadnienie kompatybilności" [EN: Alternative reinforcement of concrete using FRP composites – compatibility issues], *Mosty*, no. 1, (2015), pp. 42-45.

[5]   Elsayed T.A., Elhefnawy A.A., Eldaly A.A., Ghanem, G.M., "Hybrid fiber reinforced polymers rebars", *Journal of Advanced Materials*, vol. 43, 2011, pp. 65-75. https://doi.org/10.1163/092430410X547074

[6]   Kowalski R., Głowacki M.J., Abramowicz M., "Premature destruction of two-span RC beams exposed to high temperature caused by a redistribution of shear forces", *Journal of Civil Engineering and Manufacturing*, vol. 22, no. 8, 2016, pp. 1-9. https://doi.org/10.3846/13923730.2016.1144645

[7]   Kowalski R., Głowacki M.J., "On the experimental analysis of temperature influence on stiffness of reinforced concrete beams", *Journal of Structural Fire Engineering*, vol. 6, no. 1, 2015, pp. 49-57. https://doi.org/10.1260/2040-2317.6.1.49

[8]   ACI. Guide for the design and construction of concrete reinforced with FRP Bars. ACI 440.1R-15. Farmington Hills, MI: American Concrete Institute, 2015.

[9]   CSA. Design and construction of building structures with fibre-reinforced polymers. CAN/CSA S806-12, Canadian Standards Association, 2012, Reaffirmed in 2017, 206 pages.

[10] Nigro E., Cefarelli G., Bilotta A., Manfredi G., Cosenza E., "Fire resistance of concrete slabs reinforced with FRP bars part II: experimental results and numerical simulations on the thermal field", *Composites Part B: Engineering*, vol. 42, no. 6, 2011, pp. 1751-1763. https://doi.org/10.1016/j.compositesb.2011.02.026

[11] Nanni A., De Luca A., Jawaheri Zadeh H., *Reinforced concrete with FRP bars: Mechanics and design*. CRC Press, Boca Raton, FL, 2014.

[12] Abbasi A., Hogg P.J., "Fire testing of concrete beams with fibre reinforced plastic rebar", *Composites Part A*, vol. 37, 2006, pp.1142-1150.

[13] Hajiloo H., Green M.F., Noël M., Bénichou N., Sultan M., "Fire tests on full-scale FRP reinforced concrete slabs", *Composite Structures*, vol. 179, 2017, pp. 705-719. https://doi.org/10.1016/j.compstruct.2017.07.060

[14] Nigro E., Cefarelli G., Bilotta A., Manfredi G., Cosenza E., "Fire resistance of concrete slabs reinforced with FRP bars part I: Experimental investigations on the mechanical behavior", Composites Part B Engineering, 42 (6), (2011), pp. 1739-1750. https://doi.org/10.1016/j.compositesb.2011.02.025

[15] Kodur V.K.R., Bisby L.A., Foo S., "Thermal behaviour of fire-exposed concrete slabs reinforced with fibre reinforced polymer bars", *ACI Structural Journal*, vol. 102, no. 6, 2005, pp. 799-807.

[16] Nigro E., Cefarelli G., Bilotta A., Manfredi G., Cosenza E., "Tests at high temperatures on concrete slabs reinforced with bent FRP bars", in *Proc., 10th International symp on fiber reinforced polymer reinforcement for reinforced concrete structures*, ACI SP-275, Farmington Hills Michigan, USA, 2011.

[17] Sadek A., El-Hawary M., El-Deeb A., "Fire Resistance Testing of Concrete Beams Reinforced by GFRP Rebars", *European Journal of Scientific Resources*, vol. 15, no. 2, 2006, pp. 190-200.

[18] Protchenko K., Szmigiera E.D., Urbański M., Garbacz A., Narloch P.L., & Lesniak P., "State-of-the-Art on Fire Resistance Aspects of FRP Reinforcing Bars", *IOP Conference Series: Materials Science and Engineering*, vol. 661, 2019, pp. 1-8. http://doi.org/10.1088/1757-899X/661/1/012081

[19] Barbero E.J., *Introduction to composite materials design*. 2nd ed., Taylor & Francis Group: Boca Raton, USA, 2011.

[20] Black T., Kosher R., "Non Metallic Materials: Plastic, Elastomers, Ceramics and Composites", in *Materials and Processing in Manufacturing*. 10th ed., John Wiley & Sons, USA, (2008), pp. 162-194.

[21] Voigt W., "Uber die beziehung zwischen den beiden elasticitatsconstanten isotroperkorper", *Annals of Physics*, vol. 274, no. 12, 1889, pp. 573-587.

[22] Ashton J.E., Halpin J.C., Petit P.H., *Primer on composite materials: analysis*. Technomic, Stamford Conn., 1969.

[23] Halpin J.C. "Stiffness and expansion estimates for oriented short fiber composites", *Journal of Composite Materials*, vol. 3, 1969, pp. 732-734. https://doi.org/10.1177/002199836900300419

[24] ANSYS® Academic Research Mechanical, Release 16.2, Help System, Coupled Field Analysis Guide, ANSYS, Inc.

[25] Jesionowski T., Pilawka R., "Epoxy composites with silica crosslinked with 1-ethylimidazole" *Polymers*, vol. 11, no. 1, 2011, pp. 14-17.

[26] Baur J.W., Chen C., Justice R.S., Schaefer D.W., "Highly dispersed nanosilica-epoxy resins with enhanced mechanical properties", *Polymers*, vol. 49, 2008, pp. 3805-3815.

[27] Jesionowski T., Pilawka R., "Kompozycje epoksydowe z krzemionką", *Kompozyty*, vol. 9, no. 2, 2009, pp. 112-116.

[28] Szmigiera E., Protchenko K., Urbański M., Garbacz A., "Mechanical Properties of Hybrid FRP Bars and Nano-Hybrid FRP Bars", *Archives of Civil Engineering,* vol. 65, no. 1, 2019, pp. 97-110. https://doi.org/10.2478/ace-2019-0007

[29] Garbacz A., Szmigiera E.D., Protchenko K., Urbański M. "On Mechanical Characteristics of HFRP Bars with Various Types of Hybridization", in *Intern. Congr. on Polym. in Con. (ICPIC 2018): Polym. for Res. and Sust. Con. Infr.*, 2018, pp. 653-658. http://dx.doi.org/10.1007/978-3-319-78175-4

[30] Protchenko K., Dobosz J., Urbański M., Garbacz A., "Wpływ substytucji włókien bazaltowych przez włókna węglowe na właściwości mechaniczne prętów B/CFRP (HFRP)" [Influence of the substitution of basalt fibres by carbon fibres on the mechanical behavior of B/CFRP (HFRP) bars], Czasopismo Inżynierii Lądowej, Środowiska i Architektury, JCEEA, 63, 1/1, 2016, pp. 149-156. http://doi.prz.edu.pl/pl/pdf/biis/454

[31] Protchenko K., Szmigiera E.D., Urbański M., Garbacz A. "Development of Innovative HFRP Bars", *MATEC Web of Conf*erences, vol. 196, 2018, pp. 1-6. http://doi.org/10.1051/matec-conf/201819604087

[32] ISO 834-1 (1999), Fire Resistance Tests – Elements of Buildings Construction, Part-1 General Requirements, International Organization for Standardization, Switzerland.

Crossref
Similarity Check
Powered by iThenticate

Orginal Article

Composite beams with indented construction joint – comparison of results of laboratory tests and numerical analysis

Grzegorz Sadowski[1], Piotr Wiliński[2], Anna Halicka[3]

[1] Division of Mechanics of Structures and Building Materials; Faculty of Civil Engineering, Mechanics and Petrochemistry; Warsaw University of Technology; 17 Łukasiewicza Street, 09-400 Płock, Poland; Grzegorz.Sadowski@pw.edu.pl: (iD) 0000-0001-6441-0875

[2] Division of Building Structures and Technologies; Faculty of Civil Engineering, Mechanics and Petrochemistry; Warsaw University of Technology; 17 Łukasiewicza Street, 09-400 Płock, Poland; Piotr.Wilinski@pw.edu.pl: (iD) 0000-0002-8599-5099

[3] Department of Building Structures; Faculty of Civil Engineering and Architecture; Lublin University of Technology; 40 Nadbystrzycka Street, 20-618 Lublin, Poland; a.halicka@pollub.pl (iD) 0000-0001-5526-8862

Abstract: The paper presents a comparative analysis of the behaviour of a composite beam, consisting of a precast element with indented surface and new concrete layer, subjected to 4-point bending. The results obtained from the virtual model of the beam created using the finite element method (Abaqus/CEA 2019 software) were compared with the laboratory test results obtained with use of the digital image correlation (DIC) method for identifying the crack pattern. The virtual model of composite beam was calibrated by the choice of interface parameters ensuring that the value of load resulting in delamination between concrete layers was close to that value obtained in the laboratory tests. The comparative analysis showed that the pattern of bending and shear cracks and the pattern of interface crack obtained with the finite element method reflect the laboratory test results properly. It can be assumed that the crack between concrete layers is related to the appearance and propagation of shear cracks. On the basis of FEM analysis it can be concluded that the phenomena identified as "shear friction" and "dowel action" are significantly activated after the interface cracking.

Keywords: composite concrete beam, interface shear resistance, crack, digital image correlation (DIC), finite element method (FEM)

1. Introduction

The subject of this paper is concrete composite beam consisted of two parts: down part simulating the precast member with indented joint surface and an upper layer of new concrete simulating the *in-situ* concrete. A comparative analysis of the composite beam behaviour under the four-point bending was carried out using digital image correlation method (DIC) and the finite element method carried out with use of Abaqus/CEA 2019.

The joining mechanisms in the indented interface between concrete layers cast at different times is not exactly known. The transfer of stress between concrete layers is a pluricasual phenomenon. Its complexity is increased by the fact that the influence of each individual joint mechanism on the stress transfer is different and depends on the load level [1]–[3]. Based on the above statement, a hypothesis was formulated that it is possible to create a virtual model of composite beam with an indented interface, calibrate it on the basis on test results obtained with the use of the DIC method, and then to read out the stress that causes the interface cracking and to portray the crack pattern. The calibration of a composite beam model was carried out by the choice of interface parameters ensuring the value of load resulting in delamination between concrete layers is close to that value obtained from the laboratory tests.

The literature presents attempts of such an approach. The authors [4], [5] created a virtual model of steel-concrete composite beam, calibrated it and found out that such a scientific approach allows reflecting phenomena in this type of connection. In the paper [6], the authors proposed verification of a FEM 3D model of a reinforced concrete beam with test results carried out using the ARAMIS system. They obtained vertical deflection and cracks pattern similar to experimental results.

The comparison of results of both test methods used for reinforced concrete composite beams with the intended interface presented in this paper allows analysing the cracks and stress in the interface, as well as to describe the mechanism of damage such a composite beam. The interface parameters obtained from the calibration of a virtual model of the assumed geometric parameters of notches can be used for the analysis of composite beams with the notches of different geometry.

2. Materials and methods

2.1. Preparation of elements for testing

The tested beam consisted of a precast element with dimensions of 3000 x 150 x 250 mm, with the upper surface shaped with notches of 80 mm spacing and new concrete of 70 mm thickness.
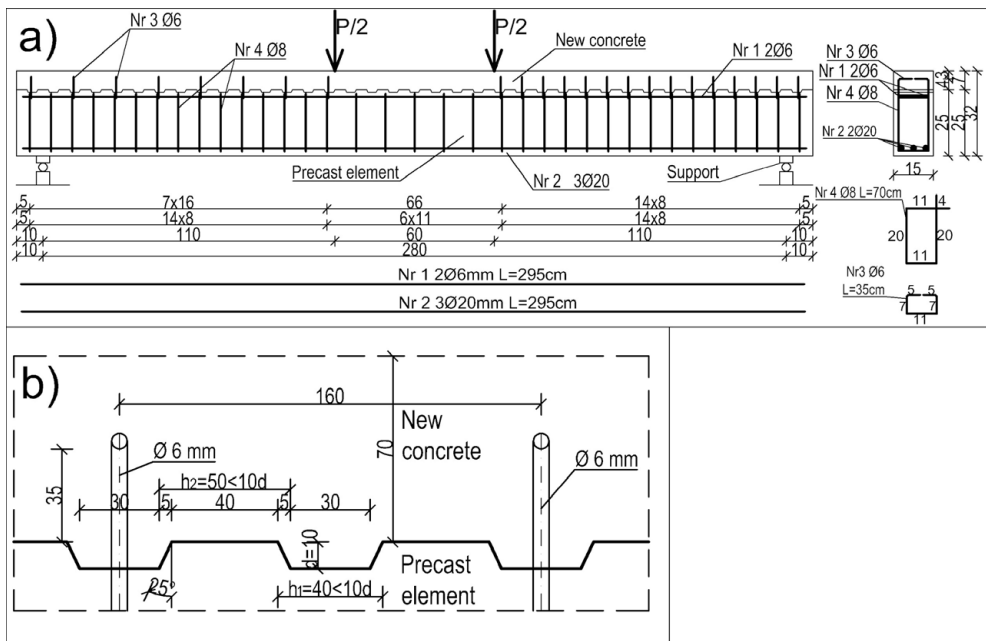
Fig. 1.   Beam element a) dimensions and reinforcement scheme, b) precast surface with notches. *Source: own study*

The bottom reinforcement consisted of 3Ø20 mm ribbed bars made of B500B steel, the stirrups of Ø8 mm ribbed bars made of B500B steel were placed at 80 mm spacing in the support zones (1120 mm of both sides), while in the rest of beam the stirrup spacing was 110 mm. Concrete layers were connected by a joining reinforcement consisting of two-armed Ø6 mm ribbed stirrups made of B500B steel at 160 mm spacing. New concrete was laid after 71 days of precast concrete curing. The precast elements were made of ready-mix class C25/30 concrete made with use of CEMI 42.5R cement. The shape of surface of the precast element as well as dimensions and arrangement of beam reinforcement are shown in Figure 1.

New concrete was made of CEM II/B-V 32.5N-LH/HSR/NA cement (producer Grupa Ożarów S.A.), fine 0–4 mm aggregate and gravel of 4–16 mm. In order to obtain an appropriate consistency of the concrete mix BETOCRETE-F27 (FM) liquefying admixture in the amount of 1% of cement mass was used. The tap water was used. The class of new concrete was determined in accordance with PN-EN 206+A1: 2016-12 [7].

The following concrete parameters were determined using samples taken during concreting:

● compressive strength of concrete (10 samples of 150×150×150 mm),

● tensile strength of concrete in splitting (6 samples of 150×150×150 mm),

● modulus of concrete elasticity (3 cylinders of Ø 150 mm, $h = 300$ mm).

The beam and samples were stored in the laboratory for 113 days (precast element) and 42 days (new concrete) until testing in air-dry conditions. The determined material parameters used later to describe the virtual model were presented in Table 1.

Table 1.   Material parameters of concrete and structural steel. *Source: own study*

Concrete				Steel		
	$f_{cm.cube}$ [MPa]	f_{ctm} [MPa]	E_{cm} [GPa]		f_y [MPa]	E_s [GPa]
New concrete	43.57	2.40	31.85	stirrups φ 6	545	200
Precast concrete	36.30	2.30	27.99	stirrups φ 8	545	200
				main reinforcement φ 20	547	200

2.2. Description of the laboratory stand

The test stand is equipped with Sylvac S_dial SWISS MODE electronic dial sensors for determining the deflections (sensors 7-9), support displacements (sensors 10-13), strain in the middle of the span (sensors 2-6, measuring base ~200 mm). The value of loading force P was read from the dynamometer (sensor 1). The load was applied to the element monotonously with the speed of about 2.7 kN/min until the element was damaged. The measurement results were recorded continuously at a frequency of 1 second and recorded in the data sheet. The diagram of the tested beam, the position of dial indicators and the location of zones for recording the results by digital cameras for image analysis are shown in Figure 2 (dial indicators were on the opposite side of the beam to the zones for image recording).
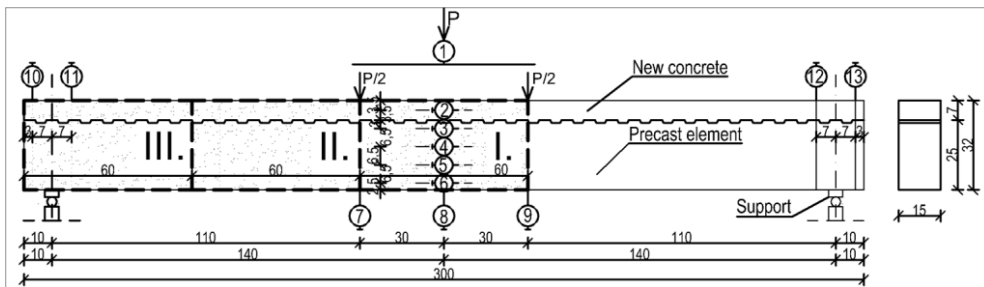
Fig. 2.   The scheme of tested composite beam: position of dial indicators (1-13) and location of zones recorded by digital cameras (I. – III.). *Source: own study*

2.3. Description of the digital image correlation method (DIC)

2D image analysis was carried out using the Digital Image Correlation (DIC) method with GOM Correlate computer software [8]. The digital image correlation method requires an appropriate preparation of elements by painting the surface to be tested with white paint and marking the pattern of black dots, which are markers used in the photo processing.

Three 24-megapixel digital cameras with APS-C size CMOS sensors were used. Each of them took photos of a part of beam surface of approximately 320 x 600 mm (as shown in Figure 2). Each part of the beam was photographed with one camera, then a 2D digital image correlation was executed. The photos were taken automatically every 20 seconds. The synchronization of photos with the results of the dial sensor measurement was achieved by correlating the internal time of digital cameras with a computer.

The method of digital image correlation consists in searching for elements with identical shapes in consecutive photos and determining the change of their coordinates. For this purpose the software assigns square or rectangular fields called "facets". In each field there is a unique pattern, which is directly used to analyse displacements and deformations.

A detailed description of the principle of DIC method, preparation and performance of tests and inaccuracies of the method can be found in publications [2], [6], [9], [10].

2.3. Description of finite element model (FEM 3D)

The virtual model of a composite beam was created using the Abaqus/CEA 2019 software [11]. The symmetry of the beam allowed to model the beam half only as shown in Figure 3.

In order to reflect the concrete performance, the CDP (Concrete Damage Plasticity) model was used. This model allows to reflect the behavior of concrete in both the compressed and tensioned zones, as well as in zones of complex stress-strain state. The basic parameters describing the concrete behavior in the CDP model were presented in Table 2 based on literature sources [3], [12] and manual recommendations [11].
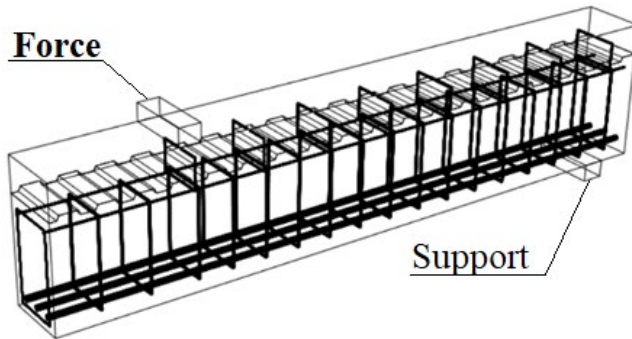
Fig. 3.   3D visualization of the numerical model of beam half. *Source: own study*

Table 2.   CDP concrete model parameters used in numerical analysis. *Source: own study based on [*3]

Parameter name	Value
K_c	0.667
Eccentricity ε	0.1
f_{b0}/f_{c0} (σ_{b0}/σ_{c0})	1.16
Dilation angle Ψ	36°
Viscosity parameter μ	0.0001

In order to correctly emulate the non-linear beam behaviour, it was necessary to assume the relation σ-ε (stress-strain) for concrete and steel. On the basis of the tested parameters (Table 1), the "stress-strain" relationship for concrete under compression and tension, shown in Figure 4, was determined. The model also took into account the elastic degradation of concrete both under compression and tension, which was defined by the parameters d_t (tension) and d_c (compression). For reinforcing steel, an elastic-plastic model with hardening was adopted, which reflected the behaviour of the material in the tensile test of the steel sample. A detailed description of this procedure has been described in publications [3], [13]–[16] and in the manual [11].
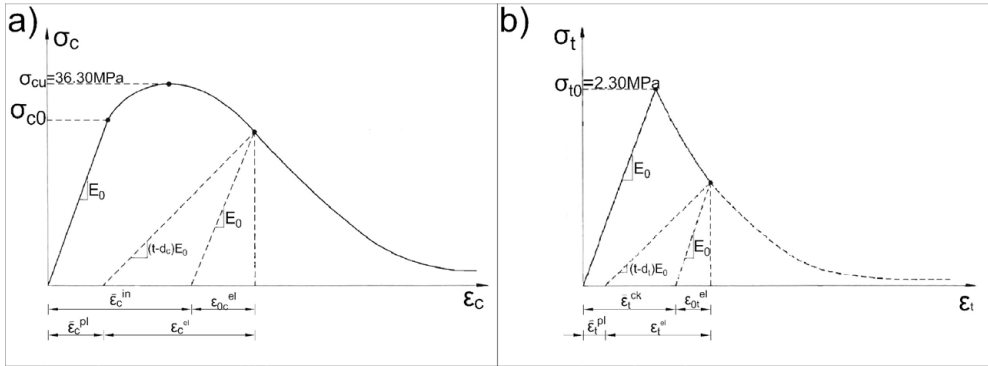
Fig. 4.   "Stress-strain" relationship of the Concrete Damaged Plasticity (CDP) model, a) for single-axis compressed concrete, b) for tension concrete. *Source: own study based on* [11]

The composite beam model discreted in the Abaqus software consisted of steel reinforcement, precast element and new concrete. For the concrete elements, a finite element grid of about 25 mm mesh size was adopted. For its construction, eight-node solid elements of C3DR8 type were used. The steel reinforcement was modelled of beam elements B31 type. The cooperation between the reinforcement and concrete was achieved by adopting the "embedded" option (steel reinforcement was the embedded element and concrete was the base one). The applied forces and reactions of supports were transmitted through 150 x 40 x 40 mm steel pads (as in laboratory tests). A "surface-to-surface" contact model of "exponential" character was chosen to simulate the cooperation between precast elements and new concrete.

The cohesion between the concrete parts was modelled with the "traction-separation" function shown in Fig. 5. This function identifies the displacement of concrete parts in relation to each other ("separation") describing the behaviour of interface due to shear stress ("traction"). The relationship is linear-elastic at the beginning and after the damage initiation it changes into the so-called "damage evolution" state, also characterized by linearity.
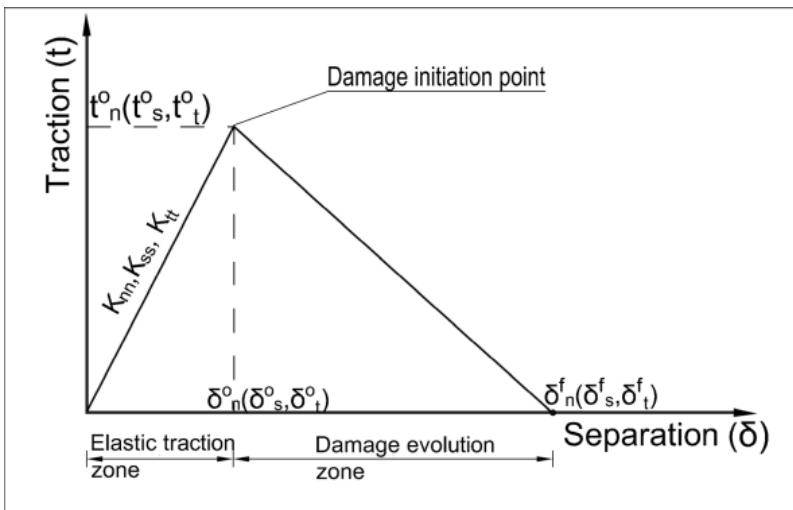
Fig. 5.   The "traction-separation" relationship adopted for description of interface behaviour. *Source: own study based on* [11]

The model calibration process was carried out assuming the friction coefficient of $\mu = 0.7$, the traction at the damage initiation in all directions equal to concrete tensile strength ($t^o_n = t^o_s = t^o_t = 2.3$ MPa) and the separation at damage in all directions (δ^f_n, δ^f_s, δ^f_t) varied from 0.001 to 0.1 mm. The value of stiffness of cohesive surface (K_{nn}, K_{ss}, K_{tt}) is assumed as the default one. The calibration was considered to be satisfactory when the obtained load which caused the interface cracking was similar to that identified by an imaging method. The best compliance with laboratory tests was achieved for a separation value of 0.005 mm.

For the simulation of cracking phenomena, the *SDEG* parameter was used, which describes the stiffness degradation of finite elements in the range from 0 to 1. The stress in steel was presented with *S,Mises* parameter and the normal force in the interface along the Z-axis was depicted with the *CNORMF3* parameter.

The cracks between the new concrete and the precast element were illustrated also by means of the *CSTATUS* parameter, which determined the displacement of adjacent finite element nodes in relation to each other corresponded to the crack appearance. On the basis of model calibration it was assumed that the crack appeared if the slip between the concretes achieved the value of 0.005 mm.

3. Results and discussion

The cracks of the beam identified by the DIC method and obtained with the finite element method were compared at different load levels. In addition, the stress in the interface and stirrups under the load causing interface crack were analysed.

Figure 6 shows cracks patterns of composite beams tested in the laboratory, identified by DIC method and that of the virtual model for different load levels.

The first bending cracks in the composite beam were observed by the DIC method under the load of 9.8 kN, while in the virtual beam model the cracks appeared under the load of 15.5 kN. Figure 6a shows the cracks under 20 kN and 80 kN loads. The perpendicular cracks in the pure bending zone under the load of 80 kN are much more intense (greater range and width) than it was observed under the load of 20 kN. The next cracks appeared in the zone between support and force, but these did not yet crack due to the dominant shear.

For the same loads, the crack pattern shown in Figure 6b using the *SDEG* parameter indicates that the number of cracks in the virtual model and their length was less than that of the DIC method. This may be due to the fact that, according to the stiffness degradation parameter definition, a finite element is completely destroyed, which is identified as crack, after tensile stress in it reached a concrete tensile strength value. Meanwhile, the DIC method shows only the values of points displacements in relation to each other and it cannot be clearly stated whether the crack has already been formed (whether the concrete tensile strength has been achieved).

Under a load of about 80 kN, both methods indicate the appearance of shear cracks and the propagation of bending cracks (Fig. 6).
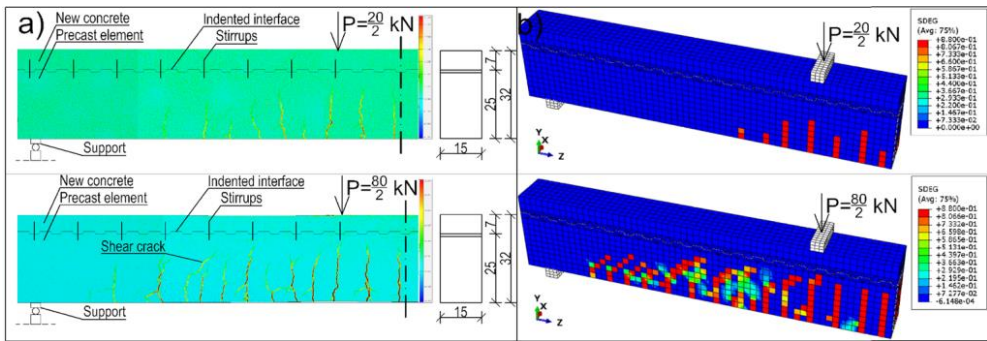
Fig. 6.   Cracks pattern of the composite beam, a) beam displacements illustrated by *GOM* Correlate [8] for 20 kN and 80 kN loads, b) crack pattern generated by *SDEG* parameter for 20 kN and 80 kN loads. *Source: own study*

The first symptoms of crack between new and precast concrete parts were observed at a load of 100.2 kN, as shown in Figure 7a. On detailed drawings of A and B areas, constituting the vertical (parallel to Y-axis) displacement maps, a horizontal crack in the down part of notch is visible. The crack was created in the place where there is no stirrup.

As the load increases, the cracks between concrete parts appear on the successive notches towards the support. The cracks pattern with a load of 180 kN (Figure 7b) includes cracks due to bending, shear and interface cracks (marked with arrows in Figure 7b) on one side of notches without joining stirrups.

The cracks pattern of the virtual composite beam model obtained with use of the *CSTATUS* parameter is presented in Figure 8a. *CSTATUS* equal to 0.005 mm, which was defined as the beginning of the crack (see chapter 2.3), was observed under a load of about 102 kN. Comparing the cracks observed with the DIC method and the *CSTATUS* and *SDEG* parameters, it can be concluded that the place and time of interface cracks formation are related to formation and propagation of shear cracks. The places of separation in the contact plane are located on the line of shear cracks trajectory, where virtual rotation points may form.

The delamination between the concrete parts shown in Figure 8b using the *CSTATUS* parameter for 180 kN load confirms the interface cracking on one side of notches. Similar to the situation of lower load level, the interface cracks were associated with the formation and propagation of subsequent shear cracks. In the numerical model delamination took place in every notch. Therefore it can be concluded that the virtual model performance differed from the laboratory tests, in which the cracks between concrete parts occurred only at the notches, where there were no joining stirrups.
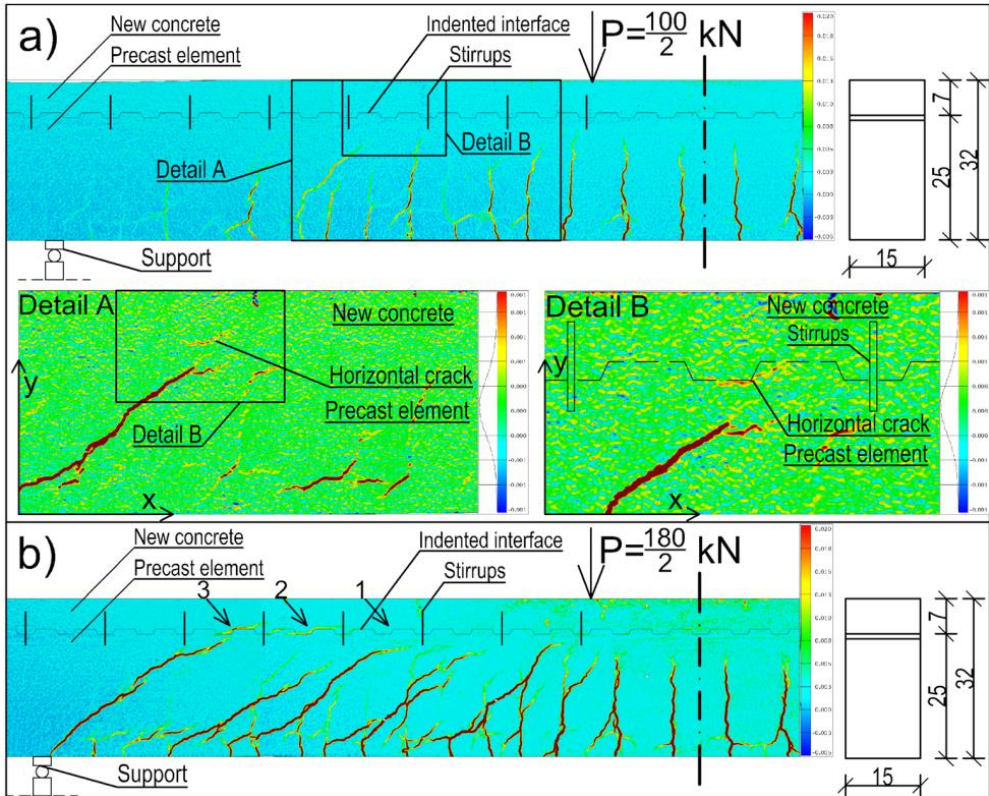
Fig. 7.   Cracks pattern of the composite beam obtained with the *GOM* Correlate software [8] with use of Y-axis displacements, a) extensive view and details A and B under 100.2 kN load, b) extensive view under 180 kN load. *Source: own study*
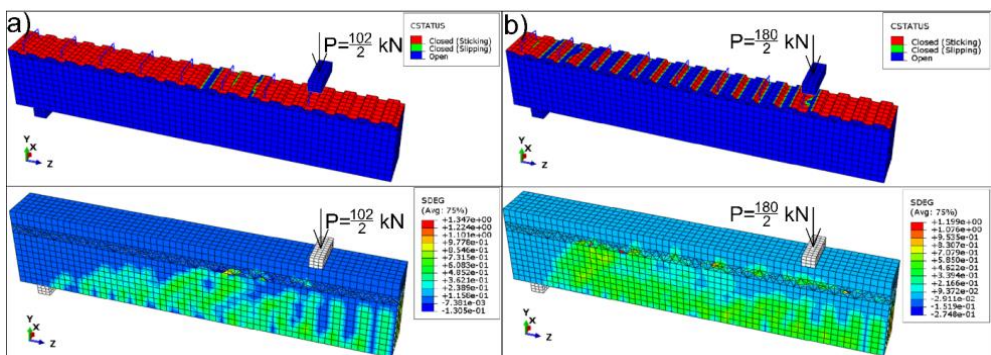
Fig. 8.   Results of FEM analysis – cracks between concretes generated using *CSTATUS* parameter and cracks pattern shown with use of *SDEG* parameter, a) for load of 102 kN, b) for 180 kN load. *Source: own study*

Figure 9 shows the "load-deflection" relationship obtained in the laboratory test and in the virtual model. They are similar to each other up to a load of about 95-100 kN. These relationships differed after the interface cracking and the difference increases along with the increase of load. The deflection of tested composite beam under the ultimate load of 198 kN was equal to 17.3 mm, while under the same load the virtual model deflection was equal to 22.3 mm. Differences in deflections are caused by the fact that interface cracks occur in each notch in the numerical model, whereas in tested beams only in few notches (Fig. 8b).
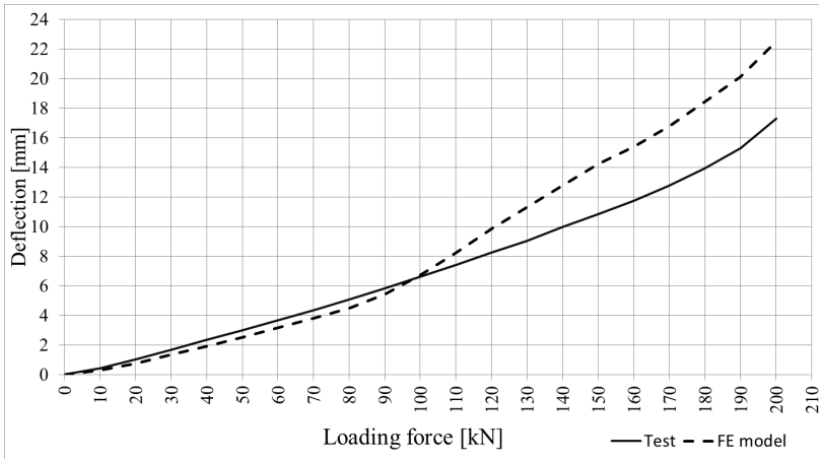
Fig. 9.   "Load- deflection" relationship of the laboratory tested composite beam and its virtual model. *Source: own study*

Figure 10 shows a map of normal forces parallel to *Z*-axis for 102 kN and 180 kN loads expressed by the *CNORMF3* parameter. In those notches where joining stirrups are present, there is a stress concentration which can be interpreted as an effect of "shear friction" phenomenon. As the load increases, normal stress increases and the range of their concentration grows towards the support, successively with the process of separation in successive notches.
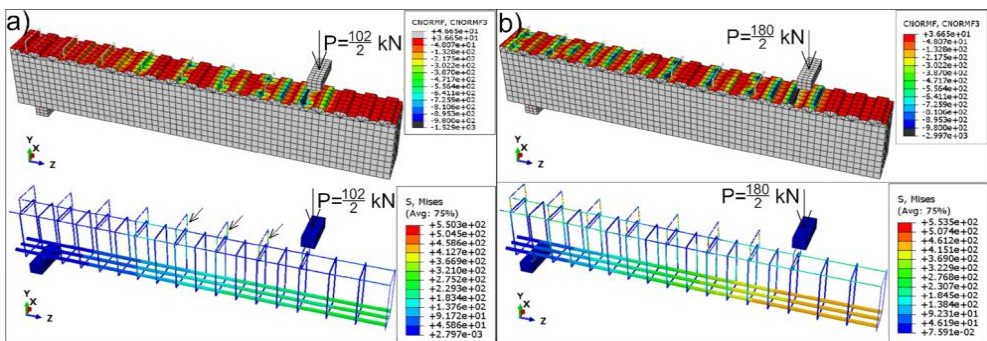
Fig. 10.   Results of FEM analysis: "shear friction" presented using *CNORMF3* and stress in the reinforcing steel presented with *S,Mises* parameter: a) for 102 kN load, b) for 180 kN load. *Source: own study*

The stresses in joining stirrups are shown in Figure 10 with use of the *S,Mises* parameter. Cracks between the concrete parts results in an increase in stress of the joining stirrups

at the points marked with arrows in Figure 10a. This confirms the "dowel action" effect. The increase in stress of the subsequent joining stirrups (Figure 10b) is related to the debonding taking place in the subsequent notches towards the support.

Comparison of the laboratory results identified by the DIC method and finite element calculations shows that the virtual model reflects the composite beam performance properly up to the first crack between precast element and new concrete. In further work, the authors will make an attempt to improve the model in order to ensure that the interface cracks reflect the results of laboratory tests over the entire load range. The interface parameters obtained from the calibration will be used to analyze composite beams with different spacing and size of notches.

4. Conclusion

On the basis of comparative analysis of the performance of the composite beam with indented interface identified by the DIC method in laboratory test and the performance of its virtual model, the following conclusions can be specified:

- Cracks between the precast element and new concrete appear on the down part of that notches on the support side, where there are no joining stirrups. As the load increases, the cracks interface widen and new ones are formed in the subsequent notches towards the support.

- Formation of cracks in indented interface is related to the appearance and propagation of shear cracks.

- The effects of "shear friction" and "dowel action" phenomena are largely activated after interface cracking. The stress concentration on the notches' surface was observed near the joining stirrups, which confirms the occurrence of the above-mentioned phenomena.

- Virtual composite beam model of composite beam with indented interface and its calibration on the basis of laboratory test results identified by DIC method allows for an extended analysis of the composite behavior beam with the indented interface. The comparative analysis has shown that the results of both methods are comparable to the moment when interface cracked. The difference in deflection results from the fact that in a virtual model, the interface cracks occur at each notch, while in laboratory tests only in notches without joining stirrups. In further work make an attempt to improve the FE model by changing the parameters inter alia the friction coefficient, stiffness of cohesive surface and decrease mesh size.

References

[1] Halicka A., *A study of the stress-strain state in the interface and support zones of composite structures with shrinkable and expansive concretes*. Wydawnictwo Politechniki Lubelskiej, Lublin, 2007.

[2] Sadowski G. and Wydra M., "Comparison of methods applied to analysis of crack propagation in reinforced concrete composite beam", *Acta Scientiarum Polonorum Architectura*, vol. 1, no. 18, 2019, pp. 3-12. https://doi.org/10.22630/ASPA.2019.18.1.1

[3] Jabłoński Ł., *Influence of surface parameters on static performance of concrete composite t-shaped beams*. Wydawnictwo Politechniki Lubelskiej, Lublin, 2018.

[4] Henriques J., Simões da Silva L. and Valente I.B., "Numerical modeling of composite beam to reinforced concrete wall joints. Part I: Calibration of joint components", *Engineering Structures*, vol. 52, (July 2013), pp. 747-761. https://doi.org/10.1016/j.engstruct.2013.03.041

[5] Henriques J., Simões da Silva L. and Valente I., "Numerical modeling of composite beam to reinforced concrete wall joints. Part II: Global behavior", *Engineering Structures*, vol. 52, (July 2013), pp. 734-746. https://doi.org/10.1016/j.engstruct.2013.03.040

[6] Szczecina M., Tworzewski P. and Uzarska I., "Numerical modeling of reinforced concrete beams, including the real position of reinforcing bars", *Structure and Environment*, vol. 10, no. 1, 2018, pp. 28-38. https://doi.org/10.30540/sae-2018-003

[7] PN-EN 206+A1:2016-12, *Concrete – Specification, performance, production and conformity*.

[8] *GOM Correlate – Software for 3D Testing Data.* Free trial license. Available: http://www.gom.com/3d-software/gom-correlate/ [Access: 15 Dec 2019]

[9] Aggelis D.G. et al., "Characterization of mechanical performance of concrete beams with external reinforcement by acoustic emission and digital image correlation", *Construction and Building Materials*, vol. 47, 2013, pp. 1037-1045. https://doi.org/10.1016/j.conbuildmat.2013.06.005

[10] Tsangouri E. et al., "Detecting the activation of a self-healing mechanism in concrete by acoustic emission and digital image correlation", *The Scientific World Journal*, vol. 2013, p. 10, 2013. https://doi.org/10.1155/2013/424560

[11] Dassault Systèmes Simulia, *Abaqus 6.1 2*, Abaqus 6.12, 2012.

[12] Kmiecik P., Kamiński M., "Modelling of reinforced concrete structures and composite structures with concrete strength degradation taken into consideration", *Archives of Civil and Mechanical Engineering*, vol. 11, iss. 3, 2011, pp. 623-636. https://doi.org/10.1016/S1644-9665(12)60105-8

[13] Chen G.M., Chen J.F. and Teng J.G., "On the finite element modelling of RC beams shear-strengthened with FRP", *Construction and Building Materials*, vol. 32, (July 2012), pp. 13-26. https://doi.org/10.1016/j.conbuildmat.2010.11.101

[14] Chen G.M., Teng J.G., and Chen J.F., "Finite-Element Modeling of Intermediate Crack Debonding in FRP-Plated RC Beams", *Journal of Composites for Construction*, vol. 15, iss. 3, (June 2011). https://doi.org/10.1061/(ASCE)CC.1943-5614.00001572011

[15] Smarzewski P., "Numerical analysis of inelastic reinforced high-strength concrete beams with low reinforcement ratio", *Budownictwo i Architektura*, vol. 4, no. 1, 2009, pp. 4-30.

[16] Sinaei H. et al., *Evaluation of reinforced concrete beam behaviour using finite element analysis by ABAQUS*, Scientific Research and Essays, vol. 7, no. 20, 2012.

Orginal Article

Thermal performance of rice husk ash mixed mortar in concrete and masonry buildings

Kajanan Selvaranjan[1], J.C.P.H. Gamage[2], G.I.P. De Silva[3], Vajira Attanayaka[4]

[1] *Department of Civil Engineering, University of Moratuwa, Sri Lanka;*
kajansss22@gmail.com 🆔 *0000-0003-3589-6065*
[2] *Department of Civil Engineering, University of Moratuwa, Sri Lanka;*
kgamage@civil.mrt.ac.lk 🆔 *0000-0002-9246-8414*
[3] *Department of Materials Science and Engineering, University of Moratuwa, Sri Lanka;*
indikagip@uom.lk 🆔 *0000-0002-8792-3494*
[4] *Airow Solutions (Pvt) Ltd, Sri Lanka; vajira@airowsolutions.com*

Abstract: Rice Husk(RH) is an agricultural waste which is produced in huge amounts from the milling process of paddy rice. Rice husk ash (RHA) is a by-product material obtained from the combustion of rice husk. The amorphous silica-rich RHA (84-90 wt%) has a wide range of applications. This research focused on the possibility of utilizing RHA in the process of developing a mortar with low thermal conductivity to enhance the thermal comfort in concrete and masonry buildings. The thermal conductivity of mortar was determined by Lee's Disc method, and the results were compared to the data for conventional mortar as well as commercial thermal insulation materials. The results indicate a significant reduction in thermal conductivity in the mortar developed with RHA.

Keywords: rice husk ash, thermal conductivity, mortar, mechanical properties, SEM

1. Introduction

Concerns with sustainable waste management and recycling have become prominent in all sectors of the economy. Thus, the new approaches to energy-efficient design are the development and use of natural materials. Replacement of cement with fly ash, sawdust ash, waste ceramic, recycled plastic, waste tyres, recycled glass and date palm in mortar or concrete are few examples [1]–[6].

Rice husk is one of the agricultural wastes that is used as a major source of biomass for fuel generation. Rice husks are usually dumped in the open area, thas is leading to contamination of water and consumption of huge land space, thereby impacting the environment negatively without any economic benefits. After the combustion of rice husk, ash is produced known as rice husk ash (RHA). When rice husk is incinerated, it produces 17%-20% mass of RHA out of the initial mass, that is a lightweight, bulky, and highly porous material with a density of around 180–200 kg/m³ [7]–[9]. RHA had been one of the wastes that has such excellent pozzolanic characteristics due to its high silica content [10]. The percentage of silica (SiO_2) and the carbon contents in the ash range between 80%-90% and 30%-50% respectively [11].

RHA is thicker as compared to the interior surface, and there is an interlayer that consists of a crisscross mesh of chips between the two surfaces. The chips are arranged in loose honey-combed fashion and contain a large number of holes. Many nanosized pores ranging from several nanometers to several microns are distributed in the interlayer. These pores contribute to the huge specific surface area and high reactivity of RHA when it is ground to powder. RHA is a fine material with particle sizes being generally less than 45 μm and the average particle size being in the range of 6-10 μm [4]. A. Siddika et al. [12] investigated that RHA is suitable as an additional cementitious material, which can be obtained by controlled or natural incineration and used with or without further processing. They have further revealed that the increase of cement replacement with RHA results in decreasing the slump and increasing the water demand.

Most studies [7], [13] have focused on the partial replacement of cement particles with RHA. S. Mayooran et al. [10] reported that the use of rice husk ash at levels of up to 5% as a replacement of cement could improve the mechanical properties of concrete. M. Jamil et al. [14] found that when RHA is applied in the preparation of mortar specimens, the compressive strength of mortar significantly increases due to the filler and pozzolanic actions. However, a lower contribution pozzolanic reaction of RHA to the strength development of mortar is observed at early ages (7 and 14 days). Pozzolanic reactions of RHA depend on their particle size, ageing time and percentage replacement of cement. S.K. Tulashie et al. [15] discussed encouraging the cement and construction industries to partially replace ordinary Portland cement with RHA to enhance the compressive strength of mortar structures. Practically, even in countries with a limited production, RHA can be a valuable addition in special products such as high strength concrete and repair mortars and also RHA addition in concrete is feasible since slump can be retained at target with the small addition of a superplasticizer, strength profile remains competitive [16].

The studies focused on thermal properties of RHA mixed mortars have been very limited. Therefore, the current study aims to investigate the thermal and mechanical properties of mortar containing various amounts of rice husk ash.

2. Experimental program

2.1. Materials

Ordinary portland cement and well-graded river sand with the size range of 0.251.18 mm were used in all the mortar mixtures. RHA used in this study (Fig. 1) was obtained from a factory in the northwestern part of Sri Lanka which has a tropical environment. According to Fig. 2 most pozzolanic particles present in between 10–50 μm. Here, the RHA with particle size less than 75 μm was used for this test program. The grading curve obtained as a result of

the Laser Diffraction analysis. The nature of RHA particles and their size distribution were observed by scanning electron microscopes (SEM) shown in Fig. 3. These SEM images showed that most of RHA have planar and angular shapes with ample smooth surface texture. The chemical composition was analysed by Atomic absorption spectroscopy and results are presented in Table 1. As shown in Table 1, RHA was mainly composed of silica along with major oxides of potassium, calcium and magnesium. Similar observations were reported in previous studies [17].
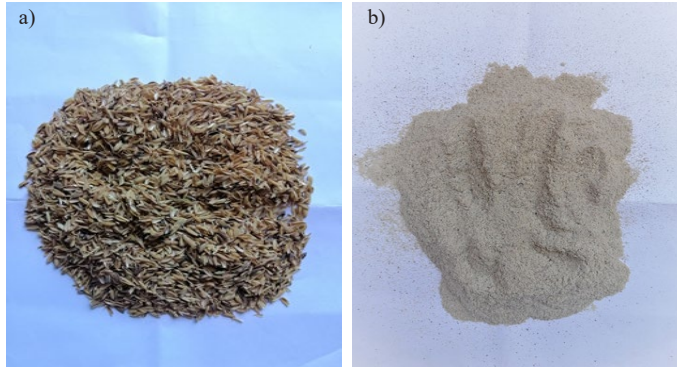
Fig. 1.   Illustration of: a) rice husk, b) rice husk ash used for the experimental program.
Source: own study
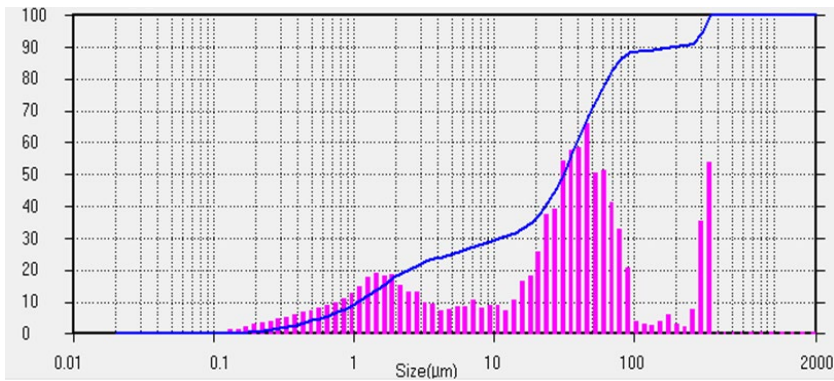
Fig. 2.   The Particle size distribution of RHA obtained by Laser Diffraction analysis. *Source:* own study
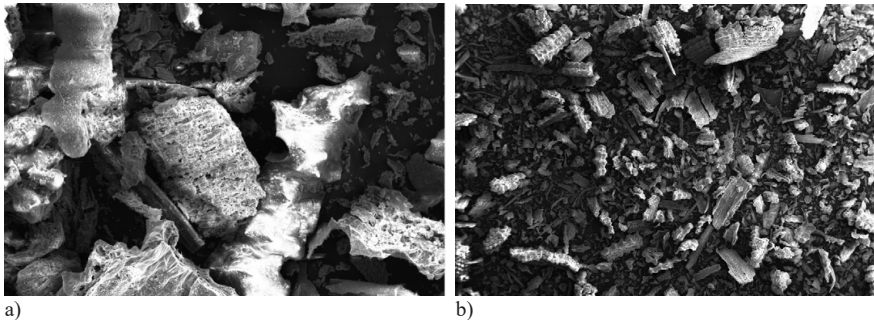
Fig. 3.   SEM observation of RHA: a) at ×75, b) at ×500 magnification level. *Source:* own study

Table 1.   Chemical examination of RHA. *Source:* own study

Chemical composition	SiO$_2$	Al$_2$O$_3$	CaO	Fe$_2$O$_3$	MgO	Na$_2$O	K$_2$O	LOI
%	85.4	1.1	2.6	0.7	1.4	0.8	3.4	7.9

2.2. Sample preparation

The control mortar mixes were prepared by using cement: sand mass ratio of 1:3. Mortar specimens with RHA were prepared using constant and varying water-cement ratios. Initially, the water-cement ratio was 0.5. The details of the specimens are given in Table 2. The flowability of mortar was measured according to ASTM C1437 [18]. The average flow diameter of the control mixture without RHA was 140 mm. Since the workability of mortar mixture decreases with the addition of RHA, a constant flow (140 mm) was maintained by varying w/c.

Table 2.   Mix proportion of mortars. *Source:* own study

Mix designation	RHA (%)	Cement (kg)	Sand (kg)	RHA (kg)	Water (kg)
M0	0	1	3	0	0.50
M10	10	1	2.7	0.3	0.78
M20	20	1	2.4	0.6	0.92
M30	30	1	2.1	0.9	1.24
M50	50	1	1.5	1.5	1.96
M70	70	1	0.9	2.1	2.24
M80	80	1	0.6	2.4	2.68
M100	100	1	0	3	3.06

2.3. Testing and results

In the application of buildings, it is important to ensure better thermal performance with the new product. Hence, the thermal conductivity of samples was measured. According to the mortar classification in ASTM C270 [19], the minimum requirement for average compressive strength for the general purpose at 28 days is 5.2 MPa. Therefore, compressive strength testing was also done in accordance with ASTM C109 [20].

2.3.1.   Thermal conductivity

The specimens were prepared in circular shaped moulds with 60 mm diameter and 5 mm depth as shown in Fig. 4. After 28 days of curing in water, the specimens were tested based on the principle of the lee disc method [21] as shown in Fig. 5. A total of 24 samples were prepared.

Fig. 4.   Specimens to check thermal conductivity. *Source:* own study

Fig. 5.   Test set-up. *Source:* own study

Figure 6 shows the thermal conductivity of mortar with different levels of RHA replacement. It is noted that the addition of RHA into the mortar results in good thermal conductivity of the mortar which exhibited a good thermal insulation property. The thermal conductivity of the 100% RHA mortar was approximately 0.213 W/mK. This is 67.42% lower than the control mixture. The thermal conductivity of porous materials is governed by the voids in the sample [2]. Thus, mortar filled with 100% RHA results in an increase in the number of voids lead to lower conductivity of the final product.
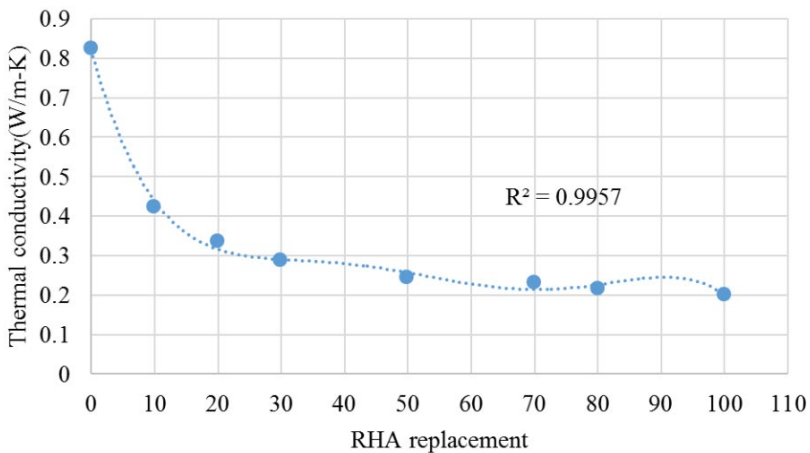
Fig. 6.   Thermal conductivity variation with RHA replacement. *Source:* own study

The coefficient of determination (0.9957) shows a fairly good prediction for thermal conductivity.

2.3.2.   Compressive strength

The preparation of the mixture is made by first mixing the materials cement, sand and RHA was mixed first without adding water when the mixture becomes homogeneous. Then, water is added to the mixture and mixed for 5 min in the mixing machine running with an

angular velocity of 50 rpm. Compressive strength of mortar cube specimens as shown in Fig. 7 (70 × 70 × 70 mm) incorporating RHA were performed in accordance with ASTM C109 [18]. Cubes were cured and tested for compressive strength at 7 and 28 days. A total of 24 samples were prepared.

Fig. 7.   Mortar cube specimens. *Source:* own study

Figure 8 shows the variation of the compressive strength of mortar as a function of RHA replacement at 7-days and 28-days of curing. It is noticed that the compressive strength of mortar decreases drastically with the increase of RHA. Mortar containing 10% to 50% RHA shows a considerable compressive strength, while the replacement of RHA above 50% shows a negative impact on the compressive strength (Fig. 10). The average compressive strength of specimens with 50% RHA replacement is 4.8 MPa, less than the minimum requirement for type N mortar [22]. This behaviour is due to the addition of low-density RHA which leads to an increase in porosity of mortars. A similar trend observed in previous studies [14], [22].
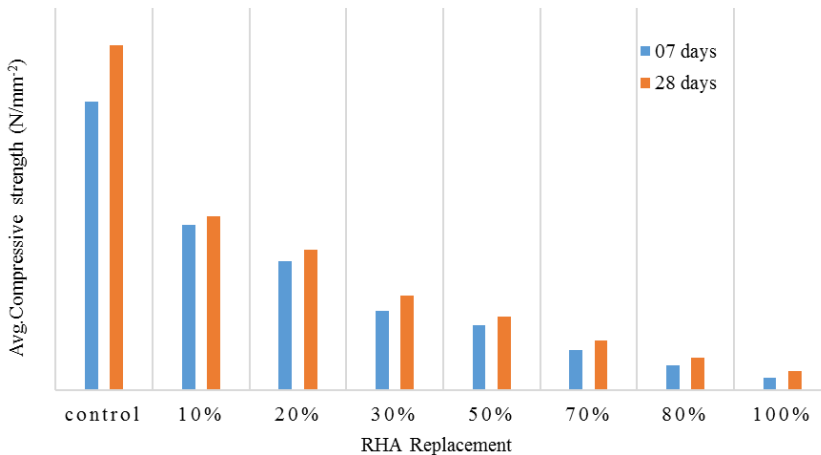
Fig. 8.   Relationship between compressive strength and amount of RHA. *Source:* own study

2.3.3. Density

The density of mortars with the variation of RHA replacement at 28 days also measured (Fig. 9). The result has shown that the density of samples with RHA was lower than that of control samples. Both bulk density and dry density have been decreased with the increase of RHA replacement. When the sand was entirely replaced with RHA, the dry density of mortar was 0.6 g/cm^3 whereas for control sample 2.2 g/cm^3 at the age of 28 days. This is due to the replacement of high-density sand with low-density RHA and also mortars containing RHA absorb more water which forms internal voids in mortars.
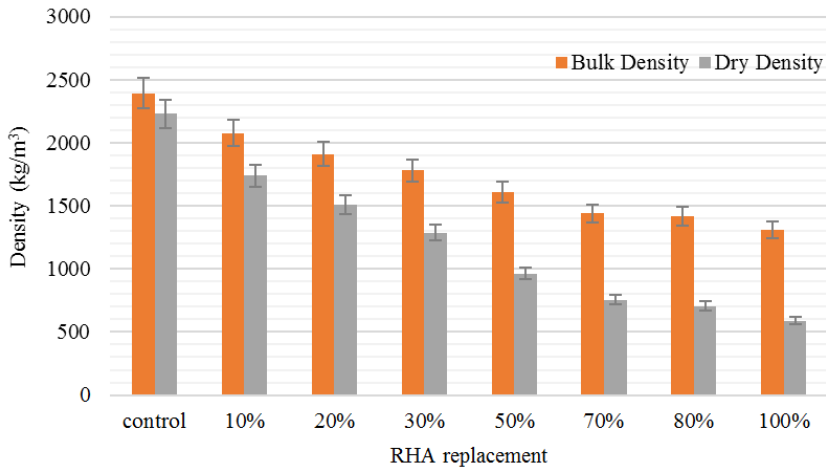
Fig. 9. Relationship between density and percentage of RHA. *Source:* own study

2.3.4. Microstructure examination

Pure RHA and mortar specimens containing a various proportion of RHA tested for thermal conductivity were observed by SEM.

The microstructure of mortars containing 10, 20, 30, 50, 70 and 100% of RHA was examined using a Scanning Electron Microscope (SEM). Figure 10 shows the SEM image of control mortar without RHA. Fig. 11 shows the results of SEM analysis for different percentages of RHA replacement. According to the figures, the size and density of voids had increased with the increase of RHA. This can be explained by the excess water absorbed by the RHA and has resulted in a reduction of compressive strength.
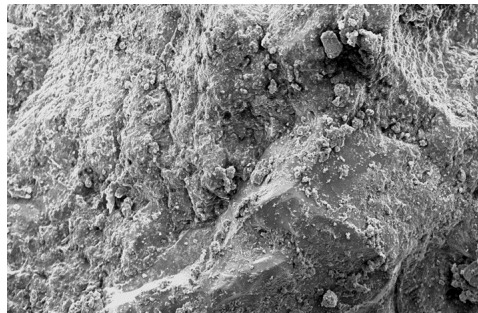
Fig. 10. SEM image of mortar without RHA. *Source:* own study
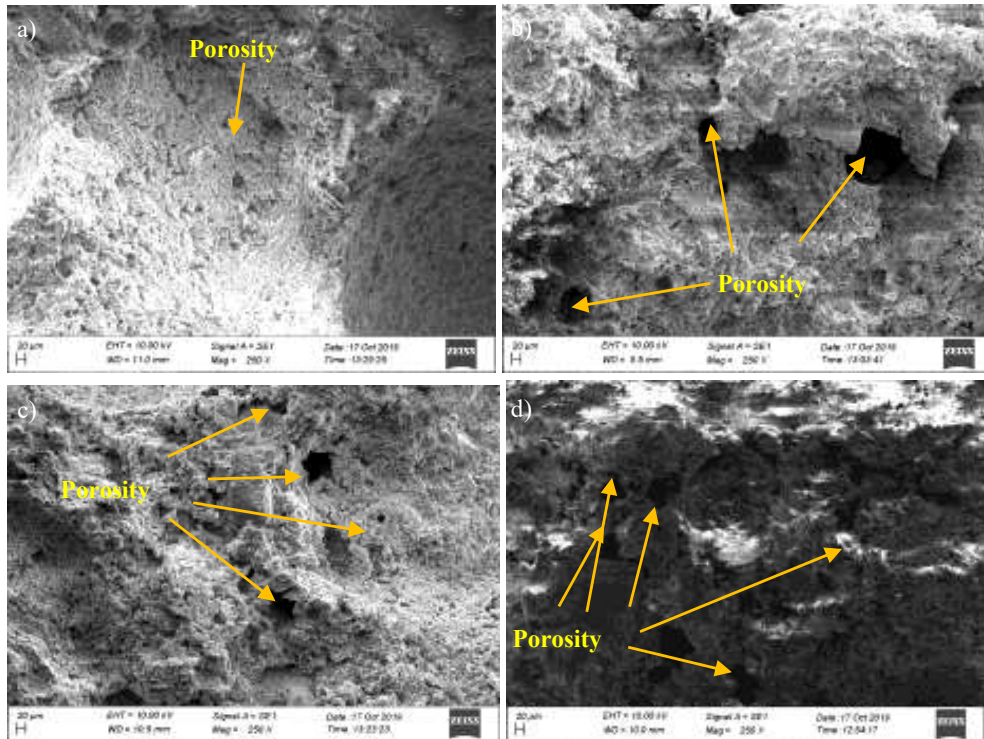
Fig. 11.   SEM images of mortar shows the pores in mortar containing, a) 20%, b) 30%, c) 50%, d) 100% rice husk ash. *Source:* own study

3. Conclusion

This study was focused on the development of an innovation of low cost insulated mortar rice waste result from paddy cultivation. The following conclusion can be made:

1. The composition RHA result from tropical cultivation is also very similar to other parts of the world.

2. The density of mortar with RHA decreases with increase in the percentage of RHA replacement. A reduction of 32.7% of bulk density was noted with the 50% replacement of RHA.

3. Almost a similar reduction in thermal conductivity was noted when the replacement ratio of RHA exceeds 50%. This is about 78.3% reduction when compared to cementitious mortar.

4. SEM results indicate an increase in porosity of mortar with the increase of RHA replacement. This has caused the heavy reduction in compressive strength of RHA replaced mortar when the replacement ratio exceeds 50%.

References

[1]   Mandal A.K., Verma H.R., and Sinha O.P., "Utilization of aluminum plant's waste for production of insulation bricks", *J. Clean. Prod.*, vol. 162, 2017, pp. 949-957.

[2] Torkittikul P., Nochaiya T., and Wongkeo W., "Utilization of coal bottom ash to improve thermal insulation of construction material", *J. Mater. Cycles Waste Manag.*, 2015.

[3] Abu Bakar B.H., Ramadhansyah P.J., and Megat Azmi M.J., "Effect of rice husk ash fineness on the chemical and physical properties of concrete", *Mag. Concr. Res.*, vol. 63, no. 5, 2011, pp. 313-320.

[4] Jaya R.P. et al., "Physical and chemical properties of cement with nano black rice husk ash", in *AIP Conference Proceedings*, 2019, vol. 2151.

[5] Corinaldesi V., Mazzoli A., and Moriconi G., "Mechanical behaviour and thermal conductivity of mortars containing waste rubber particles". *Mater. Des.*, vol. 32, no. 3, 2011, pp. 1646-1650.

[6] Kapur P.C., "Thermal Insulations from Rice Husk Ash, an Agricultural Waste", *Ceramurgia International*, vol. 6, 1953, pp. 75-78. https://doi.org/10.1016/0390-5519(80)90045-9

[7] Patel J.S., Parikh K.B., and Darji P.A.R., "Study on Concrete Using Fly Ash, Rice Husk Ash and Egg Shell Powder", *International Journal for Research*, vol. 5, 2017, pp. 566-570.

[8] Musa M.N., Fikhri M., and Aziz A., "Thermal Conductivity for Mixture of Rice Husk Fiber and Gypsum", *Applied Mechanics and Materials*, vol. 819, 2016, pp. 69-73. https://doi.org/10.4028/www.scientific.net/AMM.819.69

[9] Ruiz-herrero J.L. *et al.*, "Mechanical and thermal performance of concrete and mortar cellular materials containing plastic waste", *Construction and Building Materials*, vol. 104, 2016, pp. 298-310. https://doi.org/10.1016/j.conbuildmat.2015.12.005

[10] Mayooran S., Ragavan S., and Sathiparan N., "Comparative study on open air burnt low- and high-carbon rice husk ash as partial cement replacement in cement block production", *J. Build. Eng.*, vol. 13, (May 2017), pp. 137-145. https://doi.org/10.1016/j.jobe.2017.07.011

[11] Prasara-a J. and Gheewala S.H., "SC," *J. Clean. Prod.*, 2016.

[12] Siddika A., Al Mamun A., and Ali H., "Study on concrete with rice husk ash," *Innov. Infrastruct. Solut.*, vol. 3, no. 3, 2018. https://doi.org/10.1007/s41062-018-0127-6

[13] International T. and Of J., "Experimental Study on Rice Husk as Fine Aggregates in Concrete", no. 1992, 2014, pp. 9-14.

[14] Jamil M., M. Khan N.N., Karim M.R., Kaish A.B.M.A., and Zain M.F.M., "Physical and chemical contributions of Rice Husk Ash on the properties of mortar", *Constr. Build. Mater.*, vol. 128, 2016, pp. 185-198.

[15] Kofi S., Kotoka F., Mensah D., and Kwame A., "Investigation of the compressive strength of pit sand , and sea sand mortar prisms produced with rice husk ash as additives", *Constr. Build. Mater.*, vol. 151, 2017, pp. 383-387. https://doi.org/10.1016/j.conbuildmat.2017.06.082

[16] Antiohos S.K., Papadakis V.G., and Tsimas S., "Cement and Concrete Research Rice Husk Ash (RHA) Effectiveness in Cement and Concrete as a Function of Reactive Silica and Fineness", *Cem. Concr. Res.*, vol. 61-62, 2014, pp. 20-27. https://doi.org/10.1016/j.cemconres.2014.04.001

[17] Gonçalves M.R.F. and Bergmann C.P., "Thermal insulators made with rice husk ashes: Production and correlation between properties and microstructure", *Construction and Building Materials*, vol. 21, 2007, pp. 2059-2065. https://doi.org/10.1016/j.conbuildmat.2006.05.057

[18] ASTM C 1437-07, "Standard Test Method for Flow of Hydraulic Cement Mortar", *Annu. B. ASTM Stand.*, 2009, pp. 6-7.

[19] ASTM C 270-07, "Standard Specification for Mortar for Unit Masonry", *United States Am. Soc. Test. Mater.*, 2007, pp. 2-13.

[20] ASTM Committee, "ASTM C109/C109M-02 Standard Test Method for Compressive Strength of Hydraulic Cement Mortars," *Annu. B. ASTM Stand.*, vol. 4, 2002, pp. 1-6.

[21] Piela L.B.D.C.L., "LEED v 4 for BD and C", 2016, pp. 113-165.

[22] Na O. and Xi Y., "Mechanical and durability properties of insulation mortar with rubber powder from waste tires", *J. Mater. Cycles Waste Manag.*, 2016.

Crack mechanisms in concrete – from micro to macro scale

Marta Słowik[1], Piet Stroeven[2], Amanda Akram[3]

[1] *Department of Structural Engineering; Faculty of Civil Engineering and Architecture;*
Lublin University of Technology; 40 Nadbystrzycka Street, 20-618 Lublin, Poland;
m.slowik@pollub.pl 0000-0001-9627-3625
[2] *Faculty of Civil Engineering and Geosciences; Delft University of Technology;*
Stevinweg 1,2628 CN Delft, the Netherlands;
p.stroeven@tudelft.nl 0000-0003-1283-112X
[3] *Department of Structural Engineering; Faculty of Civil Engineering and Architecture;*
Lublin University of Technology; 40 Nadbystrzycka Street, 20-618 Lublin, Poland;
a.akram@pollub.pl 0000-0001-5619-2927

Abstract: The paper discusses a fictitious crack model of concrete in tension proposed by Hillerborg. This model presents a concept that illustrates the mechanism of crack initiation and its propagation in concrete on meso-level. It has proven to be a very useful tool for practical use, for both numerical and experimental research. The model was derived from findings on crack mechanisms on more advanced micro- and macro-scale, as presented in this paper. One of the paramount issues regarding crack analysis is the influence of aggregate size on mechanical and fracture parameters of concrete, and also on micro-crack development and associated macro-crack formation. Although significant progress in recognizing crack mechanisms in concrete has been achieved, there are still some aspects that should be studied in depth, for example the role of aggregate particles on crack development. This problem is analysed in the paper as well.

Keywords: concrete, crack mechanisms, fictitious crack model

1. Introduction

Cracking is a major aspect of concrete behaviour. The internal structure of hardened concrete is intensely micro-cracked before loading. Once loaded, the further developed crack structure is exposed to environmental influences which endanger its structural integrity. Under loading one may observe the growth of micro-cracks, which, upon further load increase, coalesce until they form a macro-crack. At still higher loadings, the macro-crack can grow and spread which may result in material fracture. Taking into account that concrete is a brittle material, the analysis of cracking mechanisms in concrete, on both micro- and macro-level, is of paramount importance in the knowledge of concrete structures.

2. Micro-level analysis

Concrete is generally intensely cracked in the so-called virgin state. In normal-strength concrete, a major part of these micro-cracks is predominately situated in the surfaces of aggregate grains, while its dispersion and orientation is quite 'random' on engineering level. These cracks are the result of high stresses due to evaporation of pore water. Loading occurs which lead to growth and coalescence of these micro-cracks that yield global damage characteristics typical for the type and intensity of loading. Such load-crack evolution processes have been successfully explained – at least qualitatively – by the concepts of elastic material. Examples based on Timoshenko's elastic stress solution for an inclusion (*i.e.*, the aggregate grain) in a semi-infinite body have been employed for this purpose in the case of completely bonded or partly debonded cylindrical grains ([1]–[5], among others). For the direct tension case, this reveals crack extension/growth in the particle-matrix interface around the zenith zones of the particle. At a certain extension, the crack leaves the interface to grow further perpendicularly to the loading direction. For a group of particles in concrete this leads to a multitude of out-of-plane cracks roughly perpendicular to the loading direction. For further crack growth, out-of-plane coalescence takes place in the fracture process zone (Fig. 1).
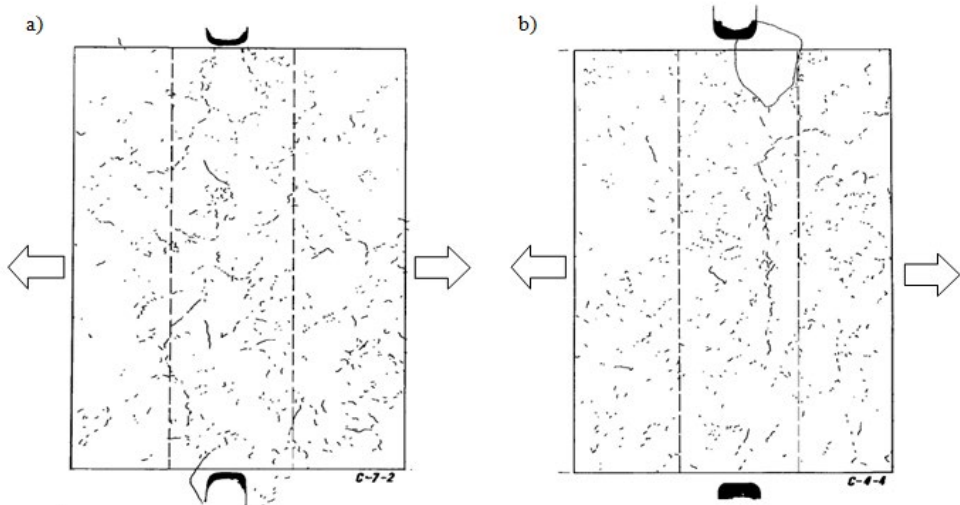
Fig. 1.   Damage states in vertical sections of the central part of two-sided notched prismatic concrete specimen (with 50 mm between the notches, visible at top and bottom) subjected to continuously increasing uniaxial tensile strains (in horizontal direction): a) stress state about three quarters of ultimate, and b) about halfway, both along the descending branch of the stress-strain curve. Contrast was improved by a fluorescent spray and thereupon photographed under illumination by UV light. Observable crack patters were eventually hand-copied. For additional experimental details, see [6]. Above, one can observe the fracture process zone in which the final fracture path is developing during yielding of the specimen. *Source:* [6]

In direct 'vertical' compression, equatorial zones are subjected to tensile stresses, leading to crack growth/coalescence at the interface. The similar action happens for a large group of aggregate particles outside the tri-axially compressed zones in zenith areas of the particles. Material tends to slip along the slopes of these compressed cone-shaped zones. This is, however, a *secondary phenomenon*, because the zones are also pre-cracked in axial direction. So, the slip takes place along the so called 'en échelon' crack arrays, thereby stimulating growth/

coalescence of axial cracking at the tops of the cones. This process of growth/coalescence of axial crack continues until the fracture, and ultimately, fracture process zones are formed. Figure 2 shows the stages of this process.

a)

b)

c)

d)
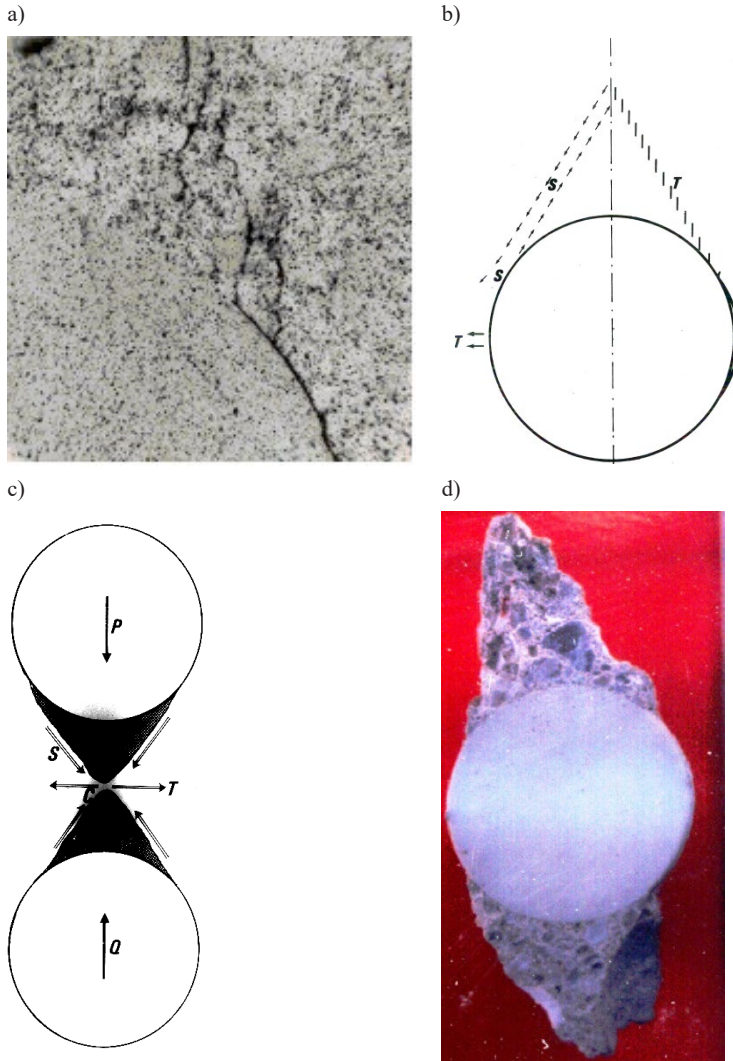
Fig. 2.   Crack mechanisms in concrete in direct compression. Under increasing loading, particles (also of gravel or sand) are ultimately completely released from material body. a) interface crack of a large spherical grain enters matrix, where vertically oriented surfaces of smaller particles are pre-cracked in an "en échelon" array, shown by the model in b). The effect of the slip on structure formation in vicinity of particle (P, Q – compressive loads, S – shear, T – tension) is depicted in c). These conically-shaped elements are found among the debris at full collapse of the specimen d). *Source:* [5], [7]–[11]

3. Macro level analysis

Concrete is a brittle material, unable to resist the high tensile stresses that are important when considering cracking. The low tensile capacity can be attributed to the high stress concentrations in concrete under loading, so that a relatively high stress level is observed in some parts of the specimen, whereas other parts are subjected to low stress. The higher strain concentration under loading is observed in an active zone of the specimen, where microscopic cracks tend to grow and coalesce (Fig. 3b). This zone is called the fracture process zone (FPZ) and it is often referred to as a progressive micro-cracking zone between the real crack and the non-cracked portion of concrete (Fig. 3a).

Micro-cracks in the fracture process zone run not linearly but over tortuous paths due to the heterogeneity of concrete. In the composite structure of concrete, there is hardened cement matrix with pores and micro-cracks, 'randomly' distributed aggregate particles, and an interfacial transition zone (ITZ). The ITZ is a weak area between cement matrix and aggregate; therefore, this is the place where micro-cracks start developing. Development of cracks is connected with the process of energy dissipation. From energetic point of view, the weakest zones in the heterogeneous structure of the concrete composite material are subjected to the processes of crack initiation and propagation. In normal-strength concrete it can be observed that cracks concentrate along weak interfaces surrounding the aggregate grains, and then join and propagate through the cement matrix, as discussed above. When the aggregate is weaker than cement matrix, like in high strength concrete or lightweight concrete, cracks also propagate through the aggregate grains. Thus, we can observe more brittle character of failure, *e.g.*, in high-strength concrete. The example of crack path propagation obtained during the splitting tensile test is presented in Fig. 3c [12].

a)   b)   c)
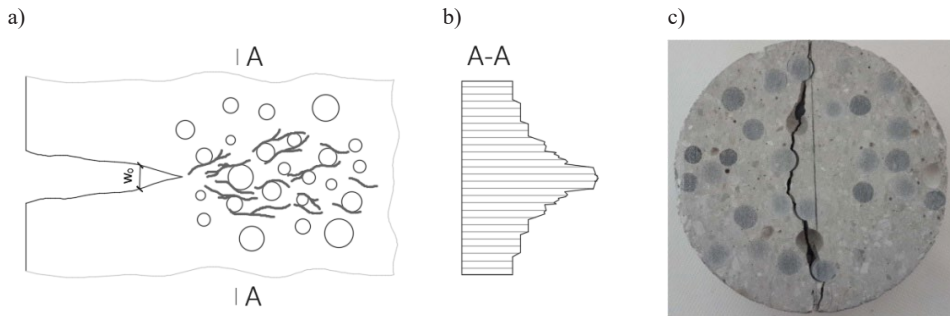
Fig. 3.   Visualization of the fracture process zone, a) in the zone of progressive micro-cracking, micro-cracks are formed along weak interfaces surrounding the aggregate grains, and then join and further propagate through the cement matrix, b) the strain distribution in the fracture process zone and its vicinity, c) experiment result of a tensile splitting test. Crack tends to pass around the aggregate grains. The latter is due to existing interface cracks that may have been formed in the virgin state or developed shortly thereafter. *Source:* [12]

Crack mechanisms are still the subject of ongoing studies on both micro- and macro-level. The advanced insight into crack mechanisms makes it possible to implement the findings into engineering practice. The brittle nature of concrete was the main problem in designing of concrete structures. The main mechanical parameters such as compressive strength f_c, tensile strength f_{ct}, and Young's modulus E_c, have proven to be not sufficient for describing

the phenomenon of concrete behaviour. If concrete had been a perfectly brittle material, every crack would lead to sudden, catastrophic failure. Therefore, concrete should be treated as a quasi-brittle material. Furthermore, it was realized that the concrete material reveals a complex structural response subjected to several important non-linear characteristics. Most of all, highly non-linear stress-strain behaviour leading to tensile cracking and compression crushing should be considered when analysing the failure processes in concrete structures.

One of the first theoretical models that took into consideration non-linearity of the crack propagation in concrete was the fictitious crack model proposed by Hillerborg [13]. The model was derived from researches on ductile fracture mechanics of metals. However, it was realized that the model for metals could not be directly applied to concrete. The main discrepancy was the presence of a significantly larger fracture process zone (FPZ) in concrete than in metals. The development of the FPZ made the application of linear elastic fracture mechanics not suitable for describing cracking in concrete. Hillerborg's model presents it as the zone where also strain-softening occurs (as the tensile stress decreases in the fracture process zone, whereas the strain, i.e., the crack tip opening displacement, increases). The strain–softening phenomenon is illustrated in Fig. 4. The picture also presents the stress-separation law in the post-peak range.
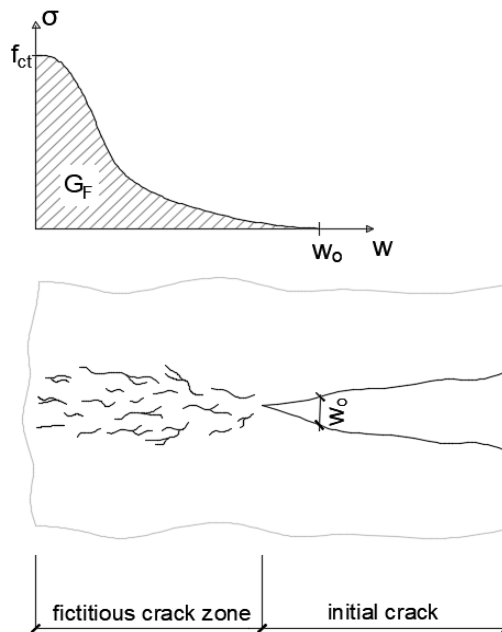
Fig. 4. Fictitious crack model for concrete in tension. Strain-softening in tension of concrete in the post-peak range is manifested by the declining stress-crack opening curve. The shaded area defines the fracture energy G_F; *Source:* [13]

The stress-opening displacement curve (σ-w) is a very useful tool in describing and illustrating the key elements in the fictitious crack model, such as the shape of the σ-w curve, tensile strength f_{ct}, and fracture energy G_F. When the stress exceeds the tensile strength, crack propagation takes place in the initiation phase. For the next step of crack formation, beyond the peak load, a certain amount of energy is needed. The energy which is absorbed per unit

area of crack face is defined as the fracture energy G_F. Fracture energy is defined as the area under the descending curve of σ-w relationship and may be estimated from

$$G_F = \int_0^{w_o} \sigma(w)\mathrm{d}w \tag{1}$$

Fracture energy can be determined experimentally in three-point bending tests on concrete beam specimens with a notch, according to the RILEM Draft Recommendation 1985 [14]. Then, G_F is given by the area under the load-deflection relationship divided by the net cross-section of the specimen above the notch.

4. Application of the fictitious crack model

On the basis of the model proposed by Hillerborg and further developments in non-linear fracture mechanics ([15], [16]), the description of the tensile behaviour of concrete was codified. The design model of concrete subjected to tensile stresses was proposed in CEB FIP Model Code 1990 [17]. As tensile failure of concrete is a discrete phenomenon, the model allows describing strain softening of concrete in tension with a bi-linear stress–strain diagram for uncracked concrete and a bi-linear stress-crack opening diagram for the cracked material. The diagrams are presented in Fig. 5 where:

G_F – fracture energy [Nm/m²], which may be estimated from Eq. 2;

w_1 – crack opening [mm], which may be calculated from Eq. 3;

w_o – crack opening [mm] for $\sigma_{ct} = 0$ as given in Tab. 1.
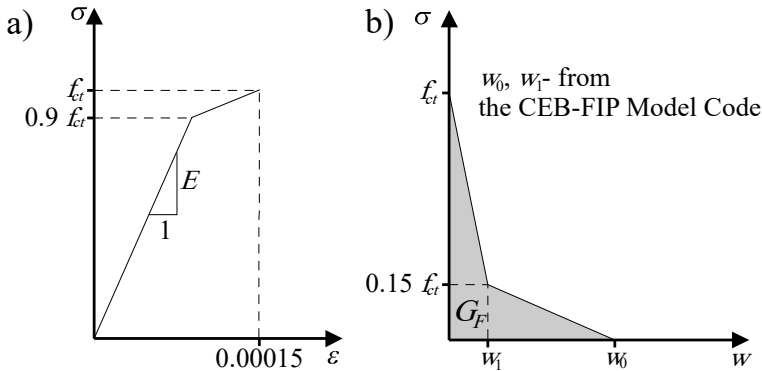
Fig. 5.   Diagrams recommended in CEB-FIP Model Code1990 for the tensile zone of concrete: a) stress versus strain, b) stress versus crack opening. *Source:* [17]

$$G_F = \alpha_F f_c^{0,7} \tag{2}$$

$$w_1 = \frac{G_F - 22 w_c \left(\frac{G_F}{\alpha_F}\right)^{0.95}}{150\left(\frac{G_F}{\alpha_F}\right)^{0.95}} \tag{3}$$

Fracture energy G_F and crack opening w_o were found to depend on the maximum aggregate size D_{max} [18]. This finding was taken into account in the code (see Tab. 1).

Table 1. Coefficients α_F and crack openings w_o according to CEB FIB Model Code. *Source:* [17]

No.	Maximum aggregate size, D_{max} [mm]	Coefficient α_F	Crack opening w_o [mm]
1	8	4	0.12
2	16	6	0.15
3	32	10	0.25

The concrete model proposed in CEB FIP Model Code [17] was successfully applied to several numerical analyses of concrete structures.

The use of the softening model in the analysis by Finite Element Method (FEM) rendered possible to describe more thoroughly fracture processes underlying the development of failure in concrete members. Also high crack resistance observed during the experiments as compared to cracking forces calculated on the basis of linear elastic theory could be properly explained [19].

The significant progress in describing size effects was possible after performing numerical simulations by means of the fictitious crack model. For various types of loading, the bigger member size, the smaller cracking forces. However, this effect is often ignored. Advanced understanding of fracture mechanics of concrete gave the possibility to rationally derive cracking forces in structural concrete members from the complete range of sizes ([20]–[22]).

Numerical simulations also helped to find a reason why the cracking moment in a lightly reinforced concrete beam is higher than in a plain concrete member ([19], [23]). Significant differences in tensile stress distribution between non-reinforced and lightly reinforced concrete beam were obtained (see Fig. 6). These differences have been noticed at load stages when strain-softening starts to develop. The numerical analysis has shown that the process of crack formation is more stable in the beam with reinforcement. Reinforcing steel bars reduce the progress in crack propagation due to the effect of bonding between concrete and the reinforcing bars. The final result is that the cracking resistance of a lightly reinforced concrete member is higher than in a plain concrete one. The comparison of tensile stress of concrete and lightly reinforced concrete beam is shown in Fig. 6.

The performed FEM-analysis showed another phenomenon connected with numerical simulation. When the progressive micro-cracking of concrete is modeled as a smeared crack band, the width of the crack band appears as an additional parameter. This is called the width of fracture process zone (w_c):

$$w_c = \frac{2G_F}{f_{ct}^2}\left(\frac{1}{E} - \frac{1}{E_t}\right)^{-1} \tag{4}$$

The performed numerical analyses ([24], [25]) have shown that the width of the fracture process zone has an influence on the FEM results. The proper selection of this parameter during the numerical calculations depended on obtaining correct results by finite element method. When examining the beam presented in Fig. 6a, the analysis of the influence of the width of the fracture process zone on the results of the numerical calculations was made. Different widths were selected for modelling this zone: w_c = 5; 10; 20; 26.5; 50; and 100 mm. Taking into account the minimum potential energy in a member, it may be stated that a best approach would be to select the smallest elongation within the localized micro-cracking zone ahead of the major crack. In the analysed beams, this condition occurs when w_c is 10 mm. When one takes $w_c = 3D_{max}$, as proposed in the literature: [15], such assumption does not fit this criterion. Note that in the analysed beam, it would be w_c = 100 mm, because D_{max} = 32 mm. Unfortunately, so far, neither a standard method of experimental determination of the width of fracture process zone has been proposed, nor the analytical

method has been described in depth. There are also no definite conclusions for the influence of aggregate size on the width of the fracture process zone. Therefore, there are no consistent rules how to define the width of micro-cracked zone in modelling concrete structures.

The presented examples of numerical simulations confirm that fictitious crack model can be successfully employed when analysing crack mechanism of concrete. Although several new concepts on describing concrete fracture have been proposed (*e.g.* [15], [26]–[29]), the "classical" Hillerborg model still finds useful application in concrete engineering (for example: [30]–[33]).
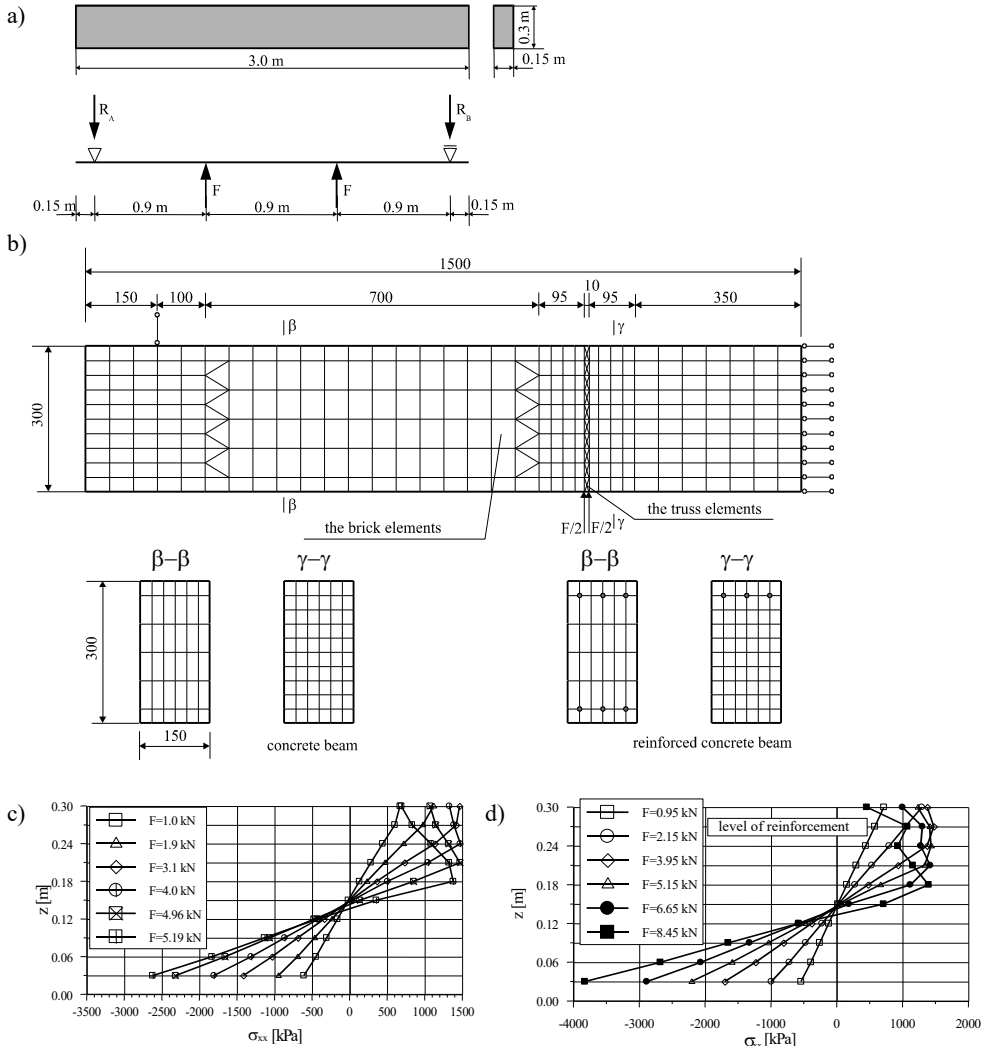
Fig. 6.   The comparison of normal stress diagrams in the fracture process zone at different load stages for c) plain concrete beam, and d) for reinforced concrete beam. a) Static scheme of the beam specimen; because of the reversed load application, the tension zone and reinforcing bars are in the upper part of the beam, b) the FEM-mesh. The numerical calculations were performed as a 3D simulation on one half of the beam, since the four-point bending test is symmetrical. The fracture process zone was modelled in the region of the highest bending moment by truss elements with non-linear characteristics of the concrete; the bulk material was modelled by brick elements as elastic material. *Source:* [19], [23]

5. Conclusions

The fictitious crack model of concrete in tension proposed by Hillerborg is a concept incorporating the mechanism of crack initiation and propagation in concrete on meso-level. This concept was found to be very useful for practical implementations, for both numerical and experimental investigations. In laboratory testing it is often denoted as the work-of-fracture method. The model was derived from the findings on crack mechanisms on more advanced micro- and macro-scale, as it was presented in this paper. One of the paramount issues connected with crack analysis is the influence of aggregate size on mechanical and fracture parameters of concrete and furthermore on micro-crack development and associated macro-crack formation. Although significant progress in recognizing crack mechanisms of concrete has been achieved, there are still some aspects that should be resolved in depth, for example the influence of aggregate particles size on crack development. This problem is supposedly associated with (sub-level) micro-crack formation resulting from the virgin state, and predominantly leading to partly debonded aggregate grains at the start of the test. The latter is definitely depending on aggregate size because a quasi-fractal phenomenon.

References

[1] Perlman A.B. and Sih G.C., "Elastostatic problems of curvilinear cracks in bonded dissimilar materials", *International Journal of Engineering Science*, no. 5 (II), 1967, pp. 845-867.

[2] Willis J.R., "Fracture mechanics of internal cracks", *Journ. Mech. Phys. Solids*, no. 19(6), 1971, pp. 353-368.

[3] Vile G.W.D., "The strength of concrete under short-term static biaxial stress", *Proc. Int. Conf. Structure of Concrete. (Eds. A.E. Brooks, K. Newman). Cem. Concr. Assoc.*, 1968, pp. 275-288.

[4] Shah S.P. and Winter G., "Inelastic behaviour and fracture of concrete", *Journ. Am. Concr. Inst.*, no. 63(9), 1966, pp. 925-930.

[5] Stroeven P., "Some aspects of the micromechanics of concrete", PhD Thesis, Delft University of Technology, Delft Univ. Press, 1973.

[6] Stroeven P., "Geometric probability approach to the examination of micro-cracking in plain concrete", *Journal of Materials Science* 14, 1979, pp. 1141-1151.

[7] Stroeven P., "Some observations on micro-cracking in concrete subjected to various loading regimes", *Engineering Fracture Mechanics*, vol. 35(4/5), 1990, pp. 775-782.

[8] Stroeven P., "Damage mechanisms in fiber reinforced concrete composites", in *Comptes rendus des neuvième journées nationales sur les composites (Eds. J.-P. Favre, A. Vautrin)*, AMAC, JNC 9 (in French), 1994, pp. 925-938.

[9] Stroeven P. "Damage evolution in compressed concrete", in: *Proceedings of the International Conference on Fracture (Ed. A. Carpinteri)*, University of Turin, Italy (on CD), 2005.

[10] Stroeven P., *50 years' focus on concrete – from meter- to nano-scale*, Media Center Rotterdam, 2015.

[11] Perry C. and Gillott J.E., "The influence of mortar aggregate bond strength on the behaviour of concrete in compression", *Cement and Concrete Research*, vol. 7(5), 1977, pp. 553-564.

[12] Benkemoun N., Khazraji H.A., Poullain P., Choinska M. and Khelidj A., "3-D mesoscale simulation of crack-permeability coupling in the Brazilian splitting test", *International Journal for Numerical and Analytical Methods in Geomechanics*, vol. 42(1), 2017, pp. 1-20.

[13] Hillerborg A., Modeer M. and Petersson P.E., "Analysis of Crack Formation and Crack Growth in Concrete by Means of Fracture Mechanics and Finite Elements", *Cement and Concrete Research*, vol. 6, 1976, 773-782.

[14] *RILEM Draft Recommendation*, *Determination of the fracture energy of mortar and concrete by means of three-point bent tests on notched beams*, *Matériaux et Constructions*, vol. 18(106), 1985, pp. 258-290.

[15] Bažant Z.P. and Oh B.H., "Crack Band Theory for Fracture of Concrete", *Matériaux et Constructions*, vol. 16(193), 1983, pp. 155-177.

[16] Cedolin L., Poli S.D. and Iori I., "Experimental Determination of the Fracture Process Zone in Concrete", *Cement and Concrete Research*, vol. 13, 1983, pp. 557-567.

[17] *CEB-FIP Model Code* 1990, *Bulletins d'information*, no. 196.

[18] Kleinschrodt H.D. and Winkler H., "The Influence of the Maximum Aggregate Size and the Size of Specimen on Fracture Mechanics Parameters", *Fracture Toughness and Fracture Energy of Concrete*. Ed. by F.H. Wittmann, Elsevier Science Publishers B.V., Amsterdam, 1986, pp. 391-402.

[19] Słowik M., "The analysis of failure in concrete and reinforced concrete beams with different reinforcement ratio", *Archive of Applied Mechanics*, vol. 89, 2019, pp. 885-895.

[20] Kwon H., Zhao Z. and Shah S.P., "Effect of specimen size on fracture energy and softening curve of concrete: Part II. Inverse analysis and softening curve", *Cement and Concrete Research*, vol. 38 (8-9), 2008, pp. 1061-1069.

[21] Kumar S. and Bara V.S., "Size-effect of fracture parameters for crack propagation in concrete: a comparative study", *Computers and Concrete*, vol. 9(1), 2012, pp. 1-19.

[22] Hoover C.G. and Bažant Z.P., "Cohesive Crack, Size Effect, Crack Band and Work-of-Fracture Models Compared to Comprehensive Concrete Fracture Tests", *International Journal of Fracture*, vol. 187(1), 2014, pp. 133-143.

[23] Słowik M., "The analysis of Crack Formation in Concrete and Slightly Reinforced Concrete Member in Bending", in *Brittle Matrix Composites* 8. Edited by A.M. Brandt, V.C. Li, I.H. Marshall, Woodhead Publishing Limited, Cambridge and Zturek Research-Scientific Institute, Warsaw, 2006, pp. 351-360.

[24] Słowik M. and Błazik-Borowa E., "The Influence of Aggregate Size on the Width of Fracture Process Zone in Concrete Members", in *Brittle Matrix Composites* 9, Woodhead Publishing Limited, Cambridge and IFTR, Warsaw, 2009, pp. 429-438.

[25] Słowik M., "Numerical analysis of the width of fracture process zone in concrete beams", *Computational Materials Science*, vol. 50, 2011, pp. 1347-1352.

[26] Hu X.Z. and Wittmann F.H., "Fracture energy and fracture process zone", *Materials and Structures*, vol. 25, 1992, pp. 319-326.

[27] Bažant Z.P. and Planas, J., *Fracture and Size Effect in Concrete and Other Quasibrittle Materials*. London: CRC Press, 1998.

[28] Rossello C., Elices M. and Guinea G.V., "Fracture of model concrete: 2. Fracture energy and characteristic length", *Cement and Concrete Research*, vol. 36(7), 2006, pp. 1345-1353.

[29] *Mechanical Behavior of Concrete*, Edited by Torrenti J.M., Pijaudier-Cabot G. and Reynouard J.M., John Wiley & Sons, Inc., 2013, pp. 63-120.

[30] Carloni C., "Analyzing bond characteristics between composites and quasi-brittle substrates in the repair of bridges and other concrete structures", *Advanced Composites in Bridge Construction and Repair*, vol. 3, 2014, pp. 61-93.

[31] Zhong H., Li H., Ooi E.T. and Song C., "Hydraulic fracture at the dam-foundation interface using the scaled boundary finite element method coupled with the cohesive crack model", *Engineering Analysis with Boundary Elements*, vol. 88, 2018, pp. 41-53. https://doi.org/10.1016/j.enganabound.2017.11.009

[32] Carloni C., Cusatis G., Salviato M., Le J.-L., Hoover C.G. and Bažant Z.P., "Critical comparison of the boundary effect model with cohesive crack model and size effect law", *Engineering Fracture Mechanics*, vol. 215, 2019, pp. 193-210. https://doi.org/10.1016/j.engfracmech.2019.04.036

[33] Cornetti P., Muñoz-Reja M., Sapora A. and Carpinteri A., "Finite fracture mechanics and cohesive crack model: Weight functions vs. cohesive laws", *International Journal of Solids and Structures*, vol. 156-157, 2019, pp. 126-136. https://doi.org/10.3390/met9050602

An innovative approach to a safety format for the estimation of structural robustness

Andrei Tur[1], Viktar Tur[2], Stanislav Derechennik[3], Aliaksandr Lizahub[4]

[1] Department of Building Structures; Faculty of Civil Engineering; Brest State Technical University; Moskovskaya 267, 224017 Brest, Belarus; aturphd@gmail.com
[2] Department of Building Structures; Faculty of Civil Engineering and Environmental Sciences; Bialystok University of Technology; 45E Wiejska Street, 15-034 Bialystok, Poland; profturvic@gmail.com 🆔 0000-0001-6046-1974
[3] Department of Computers and Computer Systems; Faculty of Electronic Information Systems; Brest State Technical University; Moskovskaya 267, 224017 Brest, Belarus; cm@brest.by
[4] Department of Building Structures; Faculty of Civil Engineering; Brest State Technical University; Moskovskaya 267, 224017 Brest, Belarus; p_332_14lizogub@mail.ru

Abstract: The estimation of structural robustness remains one of the most important stages of the design of structural systems. Recommended design strategies for the robustness assessment are based on the provisions specified in the actual EN 1991-1-7 and ISO 2394:2015. Currently, the EN 1991-1-7 and ISO2394:2015 allows the use of indirect tie-force method, but normally, non-linear pseudo-static analysis is widely used, because it is based on more realistic constitutive relations for basic variables, which enables a simulation of the real structural behaviour. Implementation of the non-linear pseudo-static analysis for the assessment of a structural system in accidental design situations requires to adopt a different approach to safety format.

The paper presents an innovative approach to safety format calibration for non-linear analysis of RC-structures subjected to accidental loads. The proposed method of the robustness estimation is based on the joint energy-saving (conversion) approach and the full probabilistic method for the estimation of a safety format for pseudo-static non-linear response of modified (damaged) structural system. The proposed probabilistic considerations are based on the Order Statistic Theory.

Keywords: robustness, progressive collapse, reliability, safety format, pseudo-static response

1. Introduction

The progressive collapse of a damaged structural system immediately after sudden loss of a column can be prevented or mitigated using the following methods:

1) TF-method (indirect tie-force method);

2) ALP-method (direct Alternate Load Path method);

3) risk-based method;

4) key-element design method.

The indirect TF-method consists of improving the structural integrity of a building by providing redundancy of Load Path and ductile detailing. Currently, the EN 1991-1-7 and ISO2394:2015 allows the use of the indirect method, some regulations concerning this subject are also contained in the EN 1992-1-1.

In this case, criteria are devised to assess the local resistance to withstand a specific assumed accidental load. The direct method, referred in [1] as "Alternate Load Path (ALP) – method" is most widely used in the practical design and based on criteria for evaluating "the capability of a damaged (modified) structural system to bridge over or around the damaged volume of area without progressive collapse developing from the local damage". This direct method requires the designer to prove that a structure is capable to fulfil its performance objectives by bridging over one or more failed (or notionally removed) structural elements, with a potential additional damage level lower than the specified limit (EN2394:2015). The ALP strategy concerns the situation where one or more structural elements (beams, columns, walls) have been damaged, for whatever reason, to such an extent that their normal load bearing capacity has vanished completely. Structural robustness and integrity are commonly defined as the sensitivity of structural system to local failure. The ALP-method consists in the assessment of redistribution of internal forces in a structural system following the sudden loss of a vertical support element on the basis of the non-linear analysis.

According to Starossek [21], the current design methods are inadequate for the assessment of progressive collapse resistance, which can be summarized as follows:

1. Current codes [10], [12], [22], [23] are based on local instead of global failure. Global structural safety against collapse of an entire system or its major part is a function of safety of all the elements against local failure.

2. The second shortcoming of the current design methods is that low-probability events and unforeseeable incidents – i.e. event E for which $P(E)$ is very small – are not taking into account. Starossek [21] argues that for a slender high-rise building, the initial local failure is the simultaneous failure of all vertical elements of a floor, thus the probability of collapse is the sum of probability of a failure of all elements. And if the number of floors is large enough, even very low probabilities of global failure resulting from accidental circumstances can sum up to a probability of the global failure large enough to be seriously considered [21].

3. The third inadequacy of the current design procedures concerns the fact that the probabilistic concept requires the specification of acceptable failure probabilities.

An excellent detailed review of all aspects concerning the regulations and research on progressive collapse and robustness of building structures is presented in [2].

In the general case, the proposed robustness assessment procedure [3] consists of the following steps:

1. determination of the non-linear static response of a considered system;

2. dynamic assessment, using a simplified approach [4] based on energy balance and on obtaining pseudo-static response;

3. determination of the ultimate (pseudo-static) gravity load (response) for the assessment of the robustness of a structural system based on the ultimate value of the static displacement u_{ult} (or ψ_{ult} for punching assessment of sudden column removal based on the [3]);

4. assessment of ductility of connections on the basis of conditions of compatibility between system and subsystem;

5. assessment of safety format for non-linear analysis of a damaged structural system. It should be emphasized that the first five steps and their adaptations are widely considered in numerous international publications, but limited number of works are devoted to safety format assessment at accidental design situation.

This paper briefly presents the main steps of assessing the robustness of a structural system based on classical energy-conservation approach, while focusing on ensuring the target safety format during the use of non-linear analysis for obtaining pseudo-static response in accidental design situation. Taking into account that safety formats for non-linear analysis implemented in currently developed codes have many uncertainties and statistically incorrect and vague formulations, this publication aims to propose a new approach to calibration of the value of the global safety factor related to computational uncertainty for NLFEAs of RC-structures in accidental design situation.

2. Determination of the non-linear response

As discussed in detail in [3], the static response under gravity loading may be established either from detailed non-linear FEM-analysis (non-linear static or non-linear dynamic) or from simplified models, as it is performed, for example, in case of the flat slabs punching [3].

As shown in [2] and [5], non-linear analysis takes into account deformation properties of RC-sections and physical constitutive relations for materials (for example, "σ-ε" for materials based on the mean values of the parameters) and allows a simulation of a real structural behaviour. It reflects an integral response, where all local sections interact and, therefore, it requires an adequate approach for safety assessment.

It should be underlined that non-linear analysis gives a possibility of assessment of global resistance and requires a safety format for global resistance [6]. In accordance with [6], the term global resistance (global safety) is used for "assessment of structural response on higher structural level than cross-section". It should be mentioned that the global resistance format is considered the best practical tool for the safety assessment of RC-elements or structural systems by means of NLFEA within the semi-probabilistic or full-probabilistic approaches.

3. Pseudo-static response of a damaged structural system

According to the approach proposed by [4], sudden loss of a column is considered to be similar in effect to sudden application of the gravity load on a damaged (modified) structure with a removed column. This damaged system can be treated as a single degree of freedom (SDOF) system consisting of vertical deflections at the point of a removed column.

Assuming that the maximum dynamic deflection u_{dyn} at the point of the joint of a removed column is equal to ultimate static displacement u_{st} obtained from the non-linear static response,

pseudo-static gravity load $F_{ps,u}$ can be calculated (Fig. 1). The following assumption is formulated on the basis of the proposed approaches [4], [7].

A modified (damaged) structural system with SDOF has the required robustness in accidental design situation, if the gravity load applied immediately after sudden column loss does not exceed ultimate pseudo-static reaction (response) $F_{ps,u}$ which is obtained from the equality balance of the external work over dynamic displacement, and internal energy absorbed by the system (substructure) over the maximum (ultimate) static deflection u_{ult}. Estimation of the Limit State of robustness performed from the following inequality:

$$F_{st} \leq F_{ps,u} \tag{1}$$

where F_{st} is a design value of the generalized gravity load, applied to a structure immediately after sudden column loss.

In general, based on energy-conservation consideration (Fig. 1), the ultimate pseudo-static response is equal:

$$F_{ps,u} = \frac{1}{u_u} \int_0^{u_u} P(u) \cdot du \tag{2}$$

where u_u is the ultimate value of the static deflection (displacement) obtained on the basis of non-linear static response.
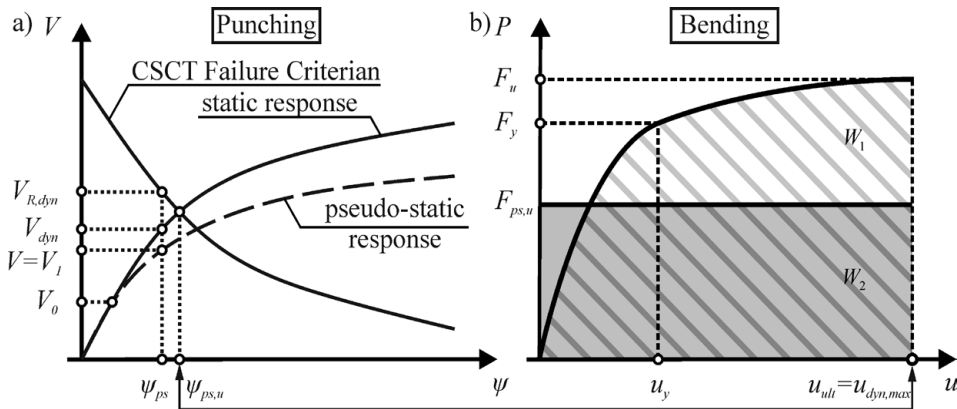
Fig. 1.   The principle of assessing the robustness of a structural system with flat slabs based on a combined approach

In case of the flat slab robustness assessment, the following combined procedure is recommended. The maximum dynamic displacement $u_{dyn,max}$, which is used for calculation of the pseudo-static ultimate gravity load $P_{ps,ult}$ in case of the bending failure mode is obtained from the corresponding pseudo-static rotation $\psi_{ps,u}$ calculated on the basis of CSCT-model for punching shear [8] (Fig. 1a).

It should be noted that this approach proposed the system pseudo-static capacity as the single measure of structural robustness, and, therefore, the energy-conservation approach might be criticised. Nevertheless, the results of the detailed analysis given in [3] shows that the implicit error due to these simplifications is relatively small (no more than 5 to 8%) and only slightly affects the final robustness assessment.

4. Safety format for the non-linear analysis

4.1. Reliability index or probability of failure

As shown in [1], the first-generation probability-based Limit Design Criteria (Limit State Design) (such as, for example, EUROCODES) are all based, to varying degrees, on reliability of individual structural members and components.

However, to implement reliability-based design criteria against progressive collapse (for robustness limit state assessment) in the field, the limit state probability (or the reliability index) should be evaluated for a structural system. In contrast to member reliability, this evaluation *"is difficult (complicated) even at the present state of art and with computational resources available"* [1].

As shown in [1], the probability of structural system failure is an order of magnitude which depends less on the redundancy of the system and the degree continuity between members. The recommended value of the acceptable reliability index β_{tag} is based on the design situation, and normally is not specified in design codes.

These threshold values were proposed by [1], assuming that the accepted unconditional probability of failure for extreme (accidental) loads is the same as the one accepted for the failure of structural elements subjected to appropriate load combinations. For example, if the mean rates of occurrence of the accidental event is: $\lambda_i = 10^{-6}\ldots10^{-5}$ (according to [1]), conditional failure probability for a structural system should be an order of $10^{-2}\ldots10^{-1}$, and the target value of reliability index β_{tag} should be an order of 1.5 (for state function $g(x)$ in case of the Normal or Lognormal distribution function for resistance). From the other hand, the maximum acceptable target failure probability (reliability index) should be estimated on the basis of LQI-acceptance criterion according to ISO2394:2015.

4.2. Safety factor for global resistance (pseudo-static response)

4.2.1. *Available methods for estimation γ_{global}*

The global resistance approach was initiated by the introduction of non-linear analysis, which is based on the global structural model and offers appropriate tools for the safety assessment [9].

In general case, the design criterion, in line with the global resistance format [10], may be expressed as the following inequality:

$$F_d \leq R_d \tag{3}$$

with $R_d = R_{rep} / (\gamma_R \cdot \gamma_{Rd})$, where: F_d is the design value of actions (effects of actions); R_d – the design value of global resistance; R_{rep} – the representative global resistance of a structure (evaluated according to a selected safety format); γ_R – the global resistance safety factor accounting for the uncertainties related to the inherent randomness of material properties (i.e. aleatory uncertainties); γ_{Rd} – the global safety factor representing the model uncertainties (i.e. epistemic uncertainties).

Various methods based on different levels of implementation of the probabilistic theory can be employed to evaluate the design structural resistance, R_d. According to the general approach of the global resistance format proposed by *fib* MC2010 [10], the design resistance R_d may be estimated by different safety format such as the probabilistic method (PM), iden-

tified as an exact approach or by one of the global resistance methods (GRM), identified as simplified approaches [11].

If the probabilistic method (PM) [9] is used, [10] the global structural resistance R is represented by an appropriate probabilistic distribution defined with the use of the non-linear FE-analysis. According to the required target level of reliability, the design of global structural resistance R_d can be evaluated directly as:

$$R_d = \frac{1}{\gamma_{Rd}} R(\alpha_R \cdot \beta) \qquad (4)$$

where: $R(\alpha_R \cdot \beta)$ is the desired quantile of the adopted distribution of the global structural resistance R corresponding to the target reliability index β value and α_R is the FORM sensitivity factor [12] ($\alpha_R < 1.0$).

As shown in our studies [13], the probabilistic method (PM) by [12] is not exact, as declared, and has many disadvantages:

1. The global resistance factor used in this safety format is not represented by a single value and must be calculated each time a new analysis is performed;

2. Probabilistic simulation is time-consuming, and therefore its use requires economic justification;

3. The adoption of the LN probability distribution functions may not be correct. The practice of calculations using simulations shows that the distribution of resistance has a so-called *"heavy tails"*. It is calculated with an unknown confidence level γ (for limited groups of results calculations). Every estimated value of the design resistance R_d which is obtained by the probability method based on the limited set of numerical results of non-linear analysis (from $n = 15$ to $n = 35$) represents only an individual value $R_{d,i}$ from probability distribution function of R_d with unknown confidence level γ.

As for the global resistance method (GRM's), different methodologies have been proposed to reduce the computational effort required by the PM, mainly: (I) the partial factor method (PFM) [10], [14], [15], (II) the method of estimating the coefficient of variation of the structural resistance ECOV [9], [10], [14], (III) the global resistance factor (GRF) [10], [15], (IV) the global safety factor (GSF) [16], and (V) the failure mode-based safety factor [11].

The most of the presented methods were analysed and compared in details in the numerous international publications [11], [12], [17]–[20] and in the authors' own studies [13].

Following the "partial factor method (PFM)", the design resistance R_d is obtained by employing a single non-linear analysis performed with the use of the design values of the material strength $f_{d(i)}$.

It can be argued that design values (f_{cd}, f_{yd}) represent extremely low material properties, which does not signify real material behaviour and thus can lead to distorted failure modes.

This method is addressed directly to target design value and thus no extrapolation is involved. Probability of global design resistance R_d is not evaluated and therefore unknown.

According to the "global resistance factor (GRF)" method, the global resistance is defined as follows:

$$R_d = \frac{1}{\gamma_{GL}} R_{rep}(f_{cmd}; f_{ym}) \qquad (5)$$

where: γ_{GL} is the global resistance factor, equal to 1.27 (constant value).

In this method a reduced value f_{cmd} for concrete compressive strength is used as follows: $f_{cmd} = 0.85f_{ck}$. It should be mentioned that the value of concrete compressive strength f_{cmd} does not represent a mean value. The partial factors for both steel and concrete failure recommended by [15] are equalized, and, therefore, "global resistance factor (GRF)" method is approximately consistent with the PFM and has the same uncertainties (mainly only compression type of failure).

Following both the "Estimate of the Coefficient of variation (ECOV)" method and the "Global Safety Format (GSF)" method [16] the design value of the global resistance R_d applies:

$$R_d = R_m / (\gamma_R \cdot \gamma_{Rd}) \tag{6}$$

where: R_d – the design value of global resistance; R_m – the structural resistance predicted by a non-linear resistance model considering the mean values of the material properties ($R_d = R(f_{cm}, f_{ym},…, a)$); γ_R – the global resistance safety factor according to the uncertainties related to the inherent randomness of material properties.

Assuming a lognormal distribution (LN) of the global resistance of the structure, the global resistance factor γ_R can be estimated as:

$$\gamma_R = \exp(\alpha_R \beta \cdot V_R) \tag{7}$$

where: V_R is the coefficient of variation of the distribution of the probability of the global structural resistance.

Taking into account LN global resistance distribution, the value V_R can be estimated as:

$$V_R = \frac{1}{1.65} \ln(R_m / R_k) \tag{8}$$

where: R_k is the structural resistance predicted by the non-linear analysis *performed using the characteristic values of the material properties* to define the structural model (i.e. $R_k = R(f_{ck}, f_{yk},…, a)$).

It should be noted that the ECOV is the most widely-mentioned and used method. This method is implemented in *fib* MC2010, prEN1992, and other guides. At first glance, the proposed method seems to be very appealing. Following authors [9] and codes [12], the keystone of the method is the determination of the mean (R_m) and characteristic (R_k) values of the global resistance only (two non-linear analyses). *However, the achieved results and detailed analysis of the proposed ECOV-method show that it is based on one incorrect statistical statement. It is known from the classical probability theory that the sum of the two 5-percentiles in not 5-percentile, and that global resistance R_k, calculated with the characteristic values of the basic variables (f_{ck}, f_{yk}) is not a characteristic value (not 5-quantile) of the global resistance distribution* (see Annex).

For comparison of the presented methods, the numerical study of the global resistance of the statically indeterminate reinforced concrete beam ($b \times h = 300 \times 500$ mm, $L = 6$ m) with the pinned ends was performed.

Based on 121 results of the numerical simulations, it was stated that in the case if characteristic values of materials strengths are used (f_{ck}, f_{yk}), the resulting global resistance R_k is in accordance with near 1-quantile (but, not 5), which, obviously, does not give the right to use the statistic value $t = 1.65$ in Eq. (8). Therefore, Eq. (8) should be rewritten as follows:

$$V_R \cong \frac{1}{c} \ln(R_m / R_k) \tag{9}$$

where: c is the statistic t (for 1-percentile, near $t = 2.15$, as shown in study [17]).

The summarized results of the comparison of safety formats recommended by the codes [10], [12], [14], [15] are given in Tab. 1.

The Tab. 1 does not show the results obtained with the method proposed by Schlune [17] (for beam element mean value of reliability index $\bar{\beta} = 4.14$ with the coefficient of variation of 3.9% was obtained).

Table 1. Comparison of the safety formats

Method	Statistical parameters of resistance, [kN]			Reliability index	Global factors	
	R_m	R_k	R_d	β_i	γ_Rd^*	γ_Rd
Probabilistic (direct 121 assessment)	280	260	243.47	3.8	1.15 [(1)]	
prEN1992-2; *fib*MC2010; ECOV	280	252	218.75	5.1	1.21	1.06 [(2)]
ECOV with $c = 2.15$	280	–	242.40	3.8	1.16	1.06
EN1992-2	266	–	209.45	5.88	1.27	

Notes: 1) the factor was calculated by Eq. (5), with $V_\mathrm{fc} = 4{,}68\%$, and $\alpha_\mathrm{R}\beta = 3.04$;
2) $\gamma_\mathrm{Rd} = 1.06$ was adopted in accordance with prEN1992, Appendix F.

In calculations with the use of EN1992-2 method (with f_yk and $f_\mathrm{cmd} = 0.85f_\mathrm{ck}$), the resulting "mean" resistance $R_\mathrm{mf} = 266$ kN almost corresponds to the characteristic value $R_\mathrm{k} = 260$ kN obtained by Probabilistic method (PM). In this case, the obtained resistance function has a standard deviation that is the same as the standard deviation of the strength of the steel reinforcement (in case of the tension failure mode). However, in the authors' opinion, the more significant problem is that concrete in this method has the same standard deviation as steel reinforcement. Such large value of the reliability index ($\beta = 5.1$) obtained with ECOV-method can be justified by incorrect statistical assessment of the characteristic resistance R_k.

The design values of the global resistance R_d obtained with Probabilistic Method (PM) had an unknown confidence level γ.

4.2.2.   *Assessment of resistance non-linear FEM-model uncertainties*

As shown in [7], the result of estimation depends on assumptions and criteria for the model used in the non-linear analysis. It should be noted that the different FEM-software, which was applied for non-linear structural analysis (obtaining of the static non-linear response), will have its own different level of FEM-model uncertainties in addition to local cross-section resistance model that covers all relevant failure mechanisms. So, the effects of computer model uncertainties should be treated separately. The coefficient variation V_vR and mean values of the computer model uncertainties are estimated on the basis of theoretical background described in [7]. It is suggested that these features are derived from the comparison of the experimental test data and numerical calculation results but through probabilistic consideration.

The set of the test results obtained with the experimental investigations of the different types of statically indeterminate structures [7] demonstrates that different failure mechanism was collected from some references and used for assessment of the coefficient variation V_vR and model uncertainty factor γ_Rd (Tab. 2). The model uncertainty factor γ_Rd takes into account the

difference between the real behaviour of structure and the results of the numerical modelling suitable for a specific structure.

It should be noted that values of γ_{Rd} are different for different FEM software. These values for FEM-program should be estimated on the basis of full probabilistic approach, taking into account statistical parameters of the FEM-model uncertainties and included in Program Manual.

Table 2. Statistical parameters of the NL FE-model uncertainties according to [7] and values of γ_{Rd}

Type of structure	β_{tag}	α_R	μ_{Rd}	V_{Rd}	σ_{Rd}	distr.	γ_{Rd}
beams, frames	1.5	0.32	1.00	0.157	0.157	LN	1.08
slabs			1.03	0.066	0.066		1.03

Notes: 1) $\beta_{tag} = 1.5$ for accidental design situation;
2) α_R – sensitivity factor, assumed equal 0.32 in case of a non-dominant resistance variable, and 0.8 – in case of a dominant variable; 3) factor γ_{Rd} calculated as follows:

$$\gamma_{Rd} = \frac{1}{\mu_{Rd}} \exp(\alpha_R \cdot \beta_{tag} \cdot V_{Rd})$$

4.2.3. *Probabilistic analysis with the use of non-parametric (order) statistics*

As shown in [6], [7] the full probabilistic analysis is the general tool for safety assessment of RC-structures, and thus it can be applied in case of non-linear analysis.

Generally, a probabilistic analysis based on numerical simulations includes the following steps:

1. numerical model formulation based on non-linear finite elements. This model describes the resistance function *r(r)* and can perform deterministic analysis of resistance for a given set of input variables;

2. randomization of input variables (random properties are defined by random distribution type and its statistical parameters);

3. probabilistic analysis of resistance (this can be performed, for example, by numerical method of Monte-Carlo-type of sampling, such as LHS sampling). Results of this analysis provide set of random parameters of resistance (and actions);

4. evaluation of safety level using reliability index β or probability of failure. A disadvantage of this approach is the fact that the target value of design resistance is located in the tail of probability distribution function (PDF), determined best fit for the sampling. The design value of the resistance is obtained by extrapolation and strongly depends on the choice of PDF of resistance.

According to the proposed approach [5], the global resistance factor γ_{glob} should be determined with the following equation:

$$\gamma_{global} = \frac{R_{m(0.5)}}{R_{d(0.01)}} \tag{10}$$

where $R_{d(0.01)}$ is design resistance (0.01-percentile of the probabilistic distribution function (pdf) of resistance); $R_{m(0.5)}$ is mean (median) value of resistance (as 0.5-percentile). Based on the Order Statistic (nonparametric) the theory of original procedure for estimation of the desired *p*-th percentile assuming arbitrary confidence level (γ) was developed and presented in detail in [5]. The main advantage of the order nonparametric statistics consists in its independence from the type of probability density function (PDF) as well as from the main statistical parameters of the continuous population.

According to the proposed approach [5], the estimator of resistance $\hat{R}_{p,\gamma}$ (in case of accidental design situation in terms of the ultimate pseudo-static response $F_{ps,u}$) of p-th percentile with desired confidence level γ can be represented as a normalized linear combination of the first three order statistics:

$$\hat{R}_{p,\gamma} = R_{lowest} - \lambda_{(1),\gamma}\Delta_{2-1} - \lambda_{(2),\gamma}\Delta_{3-2} \tag{11}$$

where $R_{lowest} = R_{(1)}$ is the lowest value of resistance in the ordered sample (set of numerical results);

$\Delta_{2-1} = R_{(2)} - R_{(1)}$ and $\Delta_{3-2} = R_{(3)} - R_{(2)}$ are non-negative differences;

$R_{(1)}, R_{(2)}, R_{(3)}$ – the first, second and third order statistics, respectively;

$\lambda_1 = \lambda(\gamma, n)$; $\lambda_2 = \lambda(\gamma, n)$ – a dimensionless coefficient, which depends on sample size n and specified confidence level γ.

Calibration of the coefficients λ_1, λ_2 for the wide range of confidence level γ performed with the use of a set of n-size random samples obtained by numerical Monte-Carlo simulations is shown in detail in [5].

Values of dimensionless coefficients λ_1, λ_2 (rounded to the hundredth place) for the assessment of the 0.01-percentile with different confidence levels γ are listed in Tab. 3.

Substituting (11) to (10) gives:

$$\gamma_{global(\gamma)} = \frac{1 - \lambda_{1(0.5;\gamma)}\delta_1 - \lambda_{2(0.5;\gamma)}\delta_2}{1 - \lambda_{1(0.01;\gamma)}\delta_1 - \lambda_{2(0.01;\gamma)}\delta_2} \tag{12}$$

with $\delta_1 = \dfrac{\Delta_{2-1}}{R_{lowest}}$, $\delta_2 = \dfrac{\Delta_{3-2}}{R_{lowest}}$.

Table 3. Values of the coefficient λ_1, λ_2 for different confidence levels γ for p-th percentile estimation ($N = 35$)

γ	0.1	0.2	0.3	0.4	0.5	0.6	0.7	0.75	0.8	0.9
					$p = 0.01$					
$\lambda_{1(\gamma)}$	-0.46	-0.28	-0.11	0.09	0.32	0.63	1.05	1.35	1.75	4.32
$\lambda_{2(\gamma)}$	-0.14	+0.03	0.19	0.37	0.58	0.86	1.26	1.53	1.9	4.29

Using the proposed approach for the assessment of robustness of a damaged structural system, a non-linear analysis of two-span frame (2 × 6 m) with beams with a cross-section of 300 × 500 mm and reinforcement ratio of $\rho_l = 0.33\%$ ($\rho_l' = 0.66\%$) was performed. The following input data were adopted in accordance with EN 1992-1-1: concrete compressive strength class C20/25, reinforcement steel B500, and constitutive relationship "σ-ε" for materials.

At the *first stage*, the series of separate deterministic non-linear analyses of the modified structural system were performed with the use of NL FEM-software for a given set of input variables. The probabilistic models of basic variables included in a non-linear state function are listed in Tab. 4.

For each of the deterministic non-linear static response, a pseudo-static response was obtained on the basis of the provisions [5] given above, and then the ultimate value of the pseudo-static gravity load $F_{ps,u}$ corresponding to the maximum dynamic displacement $u_{dyn,max}$ equal to the ultimate static displacement $u_{st,ult}$ was calculated.

As a result, a set of random values (in proposed example, $N = 35$) of ultimate pseudo-static loads (resistance) was obtained. This set of ultimate pseudo-static loads for the global safety factor γ_{global} obtained with the proposed procedure (12) was used.

Table 4. Probabilistic models of basic variables

Variable		Unit	Parameters of probability distribution function (*pdf*)			
			dist	Characteristic value	mean	COV
f_c	concrete compressive strength	MPa	N	20	28	0.173
f_y	yield strength of reinforcement steel	MPa	LN	500	560	0.054
b	width	m	N	0.3	0.3	0.033
h	height	m	N	0.5	0.5	0.033
k_R	model uncertainty for resistance: for beams for slabs	-	LN	-	1.00 1.03	0.167 0.066

Note: N – normal distribution; LN – lognormal distribution.

4.2.4. Assessment of the global safety factor

The following two approaches of determining the global safety (resistance) factor γ_{glob} were examined:

– Approach 1 – the values of the factors γ_{Rd} and γ_R were determined separately (according to [6] and proposed procedure (12), respectively), and then the value of the global safety factor γ_{glob} was calculated as the product $\gamma_{Rd}\,\gamma_R$;

– Approach 2 – the value of the global safety factor was determined in accordance with (12). In this case, the model uncertainty is considered as the basic variable of the non-linear resistance model (see k_R in Tab. 4). Tab. 5 shows influence of the confidence level of estimation γ on the global safety factor γ_{glob}, obtained with the Approach 1 and Approach 2.

For the purpose of comparison, the values of the global safety factor (global resistance factor) obtained by other methods were listed in Tab. 5.

Table 5. Influence of the confidence level γ on the global safety factor γ_{glob}

Approach	Confidence level, γ						Notes
	0.5	0.6	0.7	0.75	0.9	unknown	
Approach 1	1.22	1.23	1.26	1.31	1.49	-	$\gamma_{glob} = \gamma_{Rd}\,\gamma_R$
Approach 2	1.41	1.46	1.49	1.73	3.00	-	from simulation with k_R as basic variable
ECOV [6]	-	-	-	-	-	1.225	$\exp(\alpha_R\,\beta V)$
EN 1992-2 *fib* MC 2010	-	-	-	-	-	1.26	constant value with $f_{cm} = 0.85 f_{ck}$

The primary analysis of obtained results shows that the procedure of calibrations according to the Approach 2 gives sufficiently larger values of the global safety factor γ_{glob} than according to the Approach 1, especially with increased confidence level of estimation. This is obviously due to the fact that the statistical parameters of a model uncertainty (μ_{Rd}, σ_{Rd}) in "varying degrees" affect the final value of the global safety factor when it is estimated based on the Approach 1 or Approach 2.

When the Approach 2 is applied, the model uncertainty becomes the dominant basic variable (k_R in Tab. 4), whereas according to Approach 1, when the coefficient of variation V_{Rd} changes from 6.6% to 16.7%, calculation $\exp(\alpha_R \beta V_{Rd})$ leads to change of the value of factor γ_{Rd} from 1.03 to 1.08 (only). It was found that the global safety factor γ_{glob} values according to EN 1992-2, *fib* MC 2010, and ECOV-method are very close to value γ_{glob}, obtained by the Approach 1 for different confidence level (γ_{glob} from 1.22 to 1.29, see Tab. 5), but differ from γ_{glob} – the values obtained by the Approach 2.

The use of the values of the global safety factors in accordance with the Approach 1 to mean values of resistance $\hat{R}_m$ obtained from non-linear analysis can increase the risk of over-estimation the design value of resistance $\hat{R}_d$. The application of the calibration procedure, based on the proposed approach of interval estimation of percentile by the method of order (non-parametrical) statistics, creates the foundation for more objective assessment of the value of γ_{glob} . It allows one to perform *p*-th percentile estimation with a desired confidence level γ without resorting to the selection of the resistance distribution function type.

5. Conclusions

The simplified pseudo-static column removal scenario with appropriate gravity load combination may be used for checking of the structural systems robustness and progressive collapse prevention in accidental design situation. When performing a nonlinear analysis (NLFEA) of a modified structural system, one of the main problems remains to ensure the required safety format. It should be noted that for different FEM-software, the values of factor γ_{Rd} will be different and should be included in a Software Manual. Based on the performed studies it could be concluded that all proposed and implemented in recently developed codes safety formats for NLFEA of RC-structures are contained. An innovative calibration procedure of the global safety factor γ_{glob} was proposed on the basis of the Order Statistics (non-parametric) estimation method. The main advantage of the proposed approach is that the result of the percentile estimation does not depend on the choice of the probability distribution function (PDF). There are significant differences (up to 230% depending on the confidence level) in the γ_{glob} value for the approach when the model uncertainty k_R is considered as a basic variable in the non-linear resistance model and for the approach when the value of the global safety coefficient is defined as the product $\gamma_{Rd}\gamma_R$.

References

[1]   Ellingwood B.R. and Dusenberry D.O., "Building Design for Abnormal Loads and Progressive Collapse", *Computer – Aided Civil and Infrastructure Engineering*, vol. 20, no. 3, 2004, pp. 194-205.

[2]   Adam J.M., Parisi F., Sagaseta J., & Lu X., "Research and practice on progressive collapse and robustness of building structures in the 21st century", *Engineering Structures*, 173, 2018, pp. 122-149. doi.org./10.1016/ j.engstruct. 2018.06.082.

[3]   Olmati P., Sagaseta J., Cormie D., & Jones A.E.K., "Simplified reliability analysis of punching in reinforced concrete flat slab building under accidental action", *Engineering Structures*, vol. 130, 2017, pp. 83-98. dx.doi.org./10.1016/ j.engstruct 2016.09.061

[4]   Izzuddin B.A., Vlassis A.G., Elghazouli A.Y., & Nethercot D.A., "Progressive Collapse of Multi-Storey Buildings Due to Sudden Column Loss – Part 1: Simplified Assessment Framework", *Engineering Structures*, vol. 30, no. 5, 2008, pp. 1308-1318.

[5]   Tur V.V., Derechennik S.S., "An Innovation Conformity Criterion for Assessment of the Concrete Strength Under Uncertainty Conditions", in *High Tech Concrete: Where Technology and Engi-*

neering Meet: Proceeding of the 2017 fib Symposium, held in Maastricht, The Netherlands, June 12-14, 2017, D.A. Hordijk and M. Lukovic (eds.) – Springer International Publishing AG, 2018, pp. 1628-1635.

[6] Červenka V., "Reliability – based non-linear analysis according to fib Model Code 2010", *Structures Concrete, Journal of the fib*, vol. 14, 2013, pp. 19-28.

[7] Tur A., Tur V., "Reliability Approaches to Modelling of the Nonlinear Pseudo-static Response pf RC-structural Systems in Accidental Design Situations", *Journal of Sustainable Architecture and Civil Engineering*, vol. 1, no. 22, 2018, pp. 76-87. https://doi.org/10.5755/j01.sace.22.1.20194

[8] Micallef K., Sagaseta J., Ruiz M.F., & Muttoni A., "Assessing punching shear failure in reinforced concrete flat slabs subjected to localized impact loading", *Int. J. Impact Eng.*, vol. 71, 2014, pp.17-33.

[9] Červenka V., "Global safety formats in fib Model Code 2010 for design of concrete structures", in *Proceedings of the 11th International Probabilistic Workshop 2013*, Brno, pp. 30-41.

[10] *fib*Model Code for Concrete Structures 2010, International Federation for Structural Concrete (*fib*), Lausanne, Switzerland, 2010.

[11] Castaldo P., Gino D., Mancini G., "Safety formats for non-linear finite element analysis of reinforced concrete structures: discussion, comparison and proposals", *Engineering Structures*, vol. 193, 2019, pp. 136-153. https://doi.org/10.1016/j.engstruct.2019.05.029

[12] prEN 1990: Eurocode 0 – Basic of structural Design. Brussels, Belgium.

[13] Tur V.V., Tur A.V., Derechennik S.S., "Checking of structural system robustness based on pseudo-static full probabilistic approach", in *Proceedings of the Symposium 2019: Concrete – Innovations in Materials, Design and Structures*, Kraków, 2019, pp. 2126-2133.

[14] prEN 1992: Eurocode 2 – Design of concrete structures – Part 1-1: General rules and rules for buildings, European Committee for standardization, Brussels.

[15] EN 1992-2: Eurocode 2 – Design of concrete structures – Part 2: Concrete bridges–design and detailing rules, British Standard.

[16] Allaix D.L., Carbone V.I., Mancini G., "Global safety format for non-linear analysis of reinforced concrete structures", *Structural Concrete*, vol. 14, no. 1, 2013, pp. 29-42.

[17] Schlune H., *Safety evaluation of Concrete Structures with Nonlinear analysis*. Chalmers University of Technology, 2011.

[18] Concrete and reinforced concrete structures: SNB 5.03.01–02, Minsk, Minstrojarchitectura (in Russian).

[19] Blomfors M., *Global Safety Assessment of Concrete Structures using Nonlinear Finite Element Analysis*, Master's thesis, 2014.

[20] Nilsen-Nygaard I., *Structural Safety Assessment of Reinforced Concrete Structures with Nonlinear Finite Element Analyses and the Significance of the Modeling Uncertainty-Application to Structural Walls*, Master's thesis, 2015.

[21] Starossek U., Haberland M., *Evaluating measures of structural robustness. Proc., 2009. Structures Congress*, Austin, TX, 2009.

[22] Department of Defense. Design of building to resist progressive collapse. Washington, DC: 2009, UFC 4-023-03.

[23] American Society of Civil Engineers (ASCE). ASCE/SEI 7-10. Reston, VA: 2010. Minimum desig loads for buildings and other structures.

Assessment of the early-age strains and stresses in 2D restrained self-stressed members

Viktar V. Tur[1,2], Volha H. Sannikava[3]

[1] *Department of Concrete Technology and Building Materials; Faculty of Civil Engineering;*
Brest State Technical University; 267 Moskovskaya Street, 224017 Brest, Belarus;
profturvic@gmail.com [iD] *0000-0001-6046-1974*
[2] *Department of Building Structures; Faculty of Civil and Environmental Engineering:*
Bialystok University of Technology; 45 E Wiejska Street;15-034; Bialystok, Poland
[3] *Department of Geotechnics and Transport Communications; Faculty of Civil Engineering;*
Brest State Technical University; 267 Moskovskaya Street, 224017 Brest, Belarus; volhasann@gmail.com

Abstract: The paper presents the implementation of the modified strains development model (MSDM) for the two-way restrained self-stressed members such as expansive concrete-filled steel tubes and expansive concrete plane elements with arbitrary orthogonal reinforcement. The analytical approach allows defining the restrained strains and stresses in any 2D restraint conditions by following the iterative procedures and accounting for the elastic-plastic behaviour of expansive concrete at an early age. The consistency of the proposed method was confirmed by assessing the experimental results of the two series of the expansive concrete-filled steel tubes and three series of the expansive concrete plane members with mesh reinforcement in the centre of gravity.

Keywords: expansive concrete, strains, stresses, restraint conditions, analytical model

1. Introduction

The actual design models predict the stress-strain parameters of the expansive concrete elements under biaxial restraint conditions in a variety of ways. All known approaches can be grouped against the basic concept as follows: a) models based on the chemical energy conservation law [1]–[5]; b) empirical exponential function models [6], [7]; c) semi-empirical models [8]; d) fuzzy inference system model (FIS) [9]. It is noticeable, that majority of models ignore the elastic-plastic behaviour of the expansive concrete elements under confinements during the hydration period as well as different boundary conditions in the wide range of self-stressing elements [1]–[7]. In most cases, design models allow defining the restrained expansion strains only by the end of the expansive concrete stabilization period ignoring the development of ones at an early age of expansive concrete [1]–[7]. Moreover, in case of models based on the chemical energy conservation law, for example, the design self-stress of expansive concrete is considered

as a basic parameter while a different correlation between the values of free expansion strains and self-stressing grade arises [1]–[5]. It should also be noted, that all design methods contain the empirical coefficients that are based on the restricted experimental data so the incorrect results can arise concerning the wide range of expansive concrete elements under 2D confinement.

Thus the development of a comprehensive calculation method for the estimation the restrained expansion strains and stresses is an important problem during the design of expansive concrete elements under 2D restraint conditions.

2. The modified strain development model for the biaxial restraint conditions

2.1. The modified strains development model for the case of uniaxial restraint conditions (MSDM)

The most efficient calculation method for the estimation of the restrained expansion strains and stresses has been presented in the research paper [10] for the case of uniaxial restraint conditions. When the elastic-plastic parameters of the expansive concrete at an early age are taken into consideration, the restrained expansion strain in the x-direction at the i-*th* time interval is expressed as follows:

$$\varepsilon_{s.x}(t_{i+1/2}) = \sum_{j=1}^{i}\left[(\Delta\sigma_{c.x})_j \cdot J(t_{i+1/2}, t_j)\right] + \varepsilon_{cf}(t_{i+1/2}, t_{1/2}) \tag{1}$$

where:

$(\Delta\sigma_{c.x})_j$ – incremental self-stress in the x-direction at the j-*th* time interval;

$\varepsilon_{cf}(t_{i+1/2}, t_{1/2})$ – the difference of the free strain due to the temperature change and shrinkage or expansion of the expansive concrete in the x-direction from the time interval $t_{1/2}$ to the $t_{i+1/2}$;

$J(t_{i+1/2}, t_j)$ – creep compliance function.

Based on the above model, the modified early age strains development model (MSDM) for the case of uniaxial restraint, arrangements have been worked out [11]. The distinctive idea of MSDM concerns the presence of cumulative elastic force induced by the restraint at the end of the preceding time interval. The mentioned cumulative force accounts for the additional confinement of concrete expansion which is especially noticeable in case of high level of restraint in elements with high energy capacity of expansive concrete.

According to the MSDM for expansive concrete elements under uniaxial restraint conditions, the restrained expansion strain at any i-*th* time interval $\varepsilon_s(t_{i+1/2})$ can be performed as an algebraic sum of free expansion strain $\varepsilon_{cf}(t_{i+1/2})$, elastic strain at an i-*th* time interval $\varepsilon_{el}(t_{i+1/2})$, creep strain at i-*th* time interval under constant self-stress applied at t_0 days $\varepsilon_{pl}(t_{i+1/2}, t_0)$ and additional strain $\varepsilon_{cum}(t_{(i-1)+1/2})$ caused by the restrictive force induced by the restraint at (i-1)-*th* time interval:

$$\varepsilon_s(t_{i+1/2}) = \varepsilon_{cf}(t_{i+1/2}) + \varepsilon_{el}(t_{i+1/2}) + \varepsilon_{pl}(t_{i+1/2}, t_0) + \varepsilon_{cum}(t_{(i-1)+1/2}) \tag{2}$$

2.1. The modified early age strains development model for the case of biaxial restraint conditions

This paper presents the calculation model for assessment the restrained expansion strains in expansive concrete elements under 2D restraint conditions that is based on the modified strains development model (MSDM) for the case of uniaxial reinforcement arrangement.

The main assumptions of the proposed model are as follows:

1. confinement in orthogonal directions is considered utilizing the Poisson's ratio of early age expansive concrete $v = 0.2$ concerning the elastic strain at an i-*th* time interval ($\varepsilon_{el.x}(t_{i+1/2})$ in x-direction, $\varepsilon_{el.y}(t_{i+1/2})$ in y-direction);

2. restrained expansion strain at any i-*th* time interval in the directions x and y is an algebraic sum of free expansion strain ($\varepsilon_{cf}(t_{i+1/2})$), elastic strain ($\varepsilon_{el.x}(t_{i+1/2})$ in x-direction, $\varepsilon_{el.y}(t_{i+1/2})$ in y-direction), creep strain ($\varepsilon_{pl.x}(t_{i+1/2}, t_0)$ in x-direction, $\varepsilon_{pl.y}(t_{i+1/2}, t_0)$ in y-direction) at i-*th* time interval and additional strain caused by the restrictive force induced by the restraint ($\varepsilon_{cum.x}(t_{(i-1)+1/2})$ in x-direction, $\varepsilon_{cum.y}(t_{(i1)+1/2})$ in y-direction) at (i-1)-*th* time interval:

$$\begin{cases} \varepsilon_{s.x}(t_{i+1/2}) = \varepsilon_{cf}(t_{i+1/2}) + \left[\varepsilon_{el.x}(t_{i+1/2}) - v \cdot \varepsilon_{el.y}(t_{i+1/2}) \right] + \varepsilon_{pl.x}(t_{i+1/2}, t_0) + \varepsilon_{cum.x}(t_{(i-1)+1/2}) \\ \varepsilon_{s.y}(t_{i+1/2}) = \varepsilon_{cf}(t_{i+1/2}) + \left[\varepsilon_{el.y}(t_{i+1/2}) - v \cdot \varepsilon_{el.x}(t_{i+1/2}) \right] + \varepsilon_{pl.y}(t_{i+1/2}, t_0) + \varepsilon_{cum.y}(t_{(i-1)+1/2}) \end{cases} \quad (3)$$

3. equilibrium condition between resultant forces in restrictive reinforcement and expansive concrete section takes place because of the bond conditions in directions x and y at any i-*th* time interval.

The restrained expansion strains in x-direction and y-direction are calculated in accordance with the following expression:

$$\begin{cases} (\Delta\varepsilon_{s.x})_i = (\Delta\varepsilon_{cf})_i - \left[(\Delta\sigma_{c.x})_i - v \cdot (\Delta\sigma_{c.y})_i \right] \cdot J(t_{i+1/2}, t_i) - \\ \quad -\sum_{j=1}^{i-1}\left[(\Delta\sigma_{c.x})_j \cdot \dfrac{\Delta\varphi(t_i, t_j)}{E_{c.28}} \right] - \dfrac{\sum_{j=1}^{i-1}(\Delta\sigma_{c.x})_j}{E_c(t_{(i-1)+1/2})} \\ (\Delta\varepsilon_{s.y})_i = (\Delta\varepsilon_{cf})_i - \left[(\Delta\sigma_{c.y})_i - v \cdot (\Delta\sigma_{c.x})_i \right] \cdot J(t_{i+1/2}, t_i) - \\ \quad -\sum_{j=1}^{i-1}\left[(\Delta\sigma_{c.y})_j \cdot \dfrac{\Delta\varphi(t_i, t_j)}{E_{c.28}} \right] - \dfrac{\sum_{j=1}^{i-1}(\Delta\sigma_{c.y})_j}{E_c(t_{(i-1)+1/2})} \end{cases} \quad (4)$$

where:

$(\Delta\sigma_{c.x})_j$ and $(\Delta\sigma_{c.y})_j$ – incremental self-stress in the x-direction and the y-direction correspondingly at the j-*th* time interval;

$(\Delta\varepsilon_{cf})_i$ – incremental free strain of expansive concrete at the i-*th* time interval;

$E_{s.x}$ and $E_{s.y}$ – Young's modulus of reinforcement in the x-direction and the y-direction correspondingly;

$\rho_{s.x}$ and $\rho_{s.y}$ – reinforcement ratio in the x-direction and the y-direction correspondingly.

It can be noted that in formula (4) the values of self-stresses $(\Delta\sigma_{c.x})_j$ and $(\Delta\sigma_{c.y})_j$ at the j-*th* time interval have already been obtained, taking into account the Poisson's ratio of expansive concrete.

Because of the bond conditions, the expansive concrete and the reinforcement deform compatibly. Thus the incremental self-stresses at the i-*th* time interval in the principal axes directions are calculated by:

$$\begin{cases} (\Delta\sigma_{c.x})_i = (\Delta\varepsilon_{s.x})_i \cdot E_{s.x} \cdot \rho_{s.x} \\ (\Delta\sigma_{c.y})_i = (\Delta\varepsilon_{s.y})_i \cdot E_{s.y} \cdot \rho_{s.y} \end{cases} \quad (5)$$

where:

$(\Delta\varepsilon_{s.x})_i$ and $(\Delta\varepsilon_{s.y})_i$ – incremental restrained expansion strains at the i-*th* time interval in the x-direction and y-direction correspondingly.

The values of the restrained expansion strains and stresses in the x-direction and y-direction at a given time interval are obtained as follows:

$$\begin{cases}(\varepsilon_{s.x})_i = (\varepsilon_{s.x})_{i-1} + (\Delta\varepsilon_{s.x})_i \\ (\varepsilon_{s.y})_i = (\varepsilon_{s.y})_{i-1} + (\Delta\varepsilon_{s.y})_i \end{cases} \quad \begin{cases}(\sigma_{c.x})_i = (\sigma_{c.x})_{i-1} + (\Delta\sigma_{c.x})_i \\ (\sigma_{c.y})_i = (\sigma_{c.y})_{i-1} + (\Delta\sigma_{c.y})_i \end{cases} \quad (6)$$

The iterative calculation continues until the end of the expansive concrete stabilization period.

2.2. The modified early age strains development model for the case of the steel tube symmetrical restraint conditions

Based on the assumptions [11], [12], for the case of the steel tube symmetrical restraint arrangement (see Fig. 1), the basic equations for calculating of the incremental restrained strains in the circumferential direction $(\Delta\varepsilon_{s.\theta})_i$ and the axial direction $(\Delta\varepsilon_{s.z})_i$ at any i-*th* time interval with regard to the vertical reaction can be expressed as follows:

$$\begin{cases}(\Delta\varepsilon_{s.\theta})_i = (\Delta\varepsilon_{cf})_i - (\Delta\sigma_{c.\theta})_i \cdot J(t_{i+1/2}, t_i) - \sum_{j=1}^{i-1}\left[(\Delta\sigma_{c.\theta})_j \cdot \dfrac{\Delta\varphi(t_i, t_j)}{E_{c.28}}\right] - \dfrac{\sum_{j=1}^{i-1}(\Delta\sigma_{c.\theta})_j}{E_c(t_{(i-1)+1/2})} \\[4mm] (\Delta\varepsilon_{s.z})_i = (\Delta\varepsilon_{cf})_i - (\Delta\sigma_{c.z})_i \cdot J(t_{i+1/2}, t_i) - \sum_{j=1}^{i-1}\left[(\Delta\sigma_{c.z})_j \cdot \dfrac{\Delta\varphi(t_i, t_j)}{E_{c.28}}\right] - \dfrac{\sum_{j=1}^{i-1}(\Delta\sigma_{c.z})_j}{E_c(t_{(i-1)+1/2})}\end{cases} \quad (7)$$

Fig. 1.   2D symmetrical restraint in case of the expansive concrete-filled steel tube. *Source:* own study

Incremental self-stresses can be calculated according to the expressions:

$$\begin{cases}(\Delta\sigma_{c.\theta})_i = \dfrac{t}{r_0}\dfrac{E_s}{(1-v_s^2)}\left[(\Delta\varepsilon_{s.\theta})_i + v_s(\Delta\varepsilon_{s.z})_i\right] \\[4mm] (\Delta\sigma_{c.z})_i = \dfrac{2t}{r_0}\dfrac{E_s}{(1-v_s^2)}\left[(\Delta\varepsilon_{s.z})_i + v_s(\Delta\varepsilon_{s.\theta})_i\right]\end{cases} \quad (8)$$

where:

E_s – modulus of elasticity of steel tube;

v_s – Poisson's ratio of steel tube;

r_0 – initial radius of steel tube;

t – thickness of steel tube.

Substituting Eq.(8) in Eq. (7), incremental restrained expansion strains $(\Delta\varepsilon_{s.\theta})_i$ and $(\Delta\varepsilon_{s.z})_i$ at any i-th time interval are expressed as follows:

$$
\begin{cases}
(\Delta\varepsilon_{s.\theta})_i = (\Delta\varepsilon_{cf})_i - \dfrac{t}{r}\dfrac{E_s}{(1-v_s^2)}\left[(\Delta\varepsilon_{s.\theta})_i + v_s(\Delta\varepsilon_{s.z})_i\right]\cdot J(t_{i+1/2},t_i) - \\[4mm]
-\displaystyle\sum_{j=1}^{i-1}\left[(\Delta\sigma_{c.\theta})_j\cdot\dfrac{\Delta\varphi(t_i,t_j)}{E_{c.28}}\right] - \dfrac{\displaystyle\sum_{j=1}^{i-1}(\Delta\sigma_{c.\theta})_j}{E_c(t_{(i-1)+1/2})} \\[8mm]
(\Delta\varepsilon_{s.z})_i = (\Delta\varepsilon_{cf})_i - \dfrac{2t}{r_0}\dfrac{E_s}{(1-v_s^2)}\left[(\Delta\varepsilon_{s.z})_i + v_s(\Delta\varepsilon_{s.\theta})_i\right]\cdot J(t_{i+1/2},t_i) - \\[4mm]
-\displaystyle\sum_{j=1}^{i-1}\left[(\Delta\sigma_{c.z})_j\cdot\dfrac{\Delta\varphi(t_i,t_j)}{E_{c.28}}\right] - \dfrac{\displaystyle\sum_{j=1}^{i-1}(\Delta\sigma_{c.z})_j}{E_c(t_{(i-1)+1/2})}
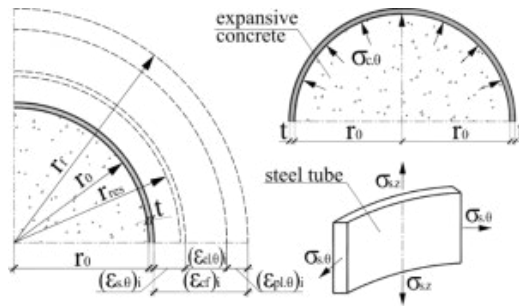\end{cases}
\tag{9}
$$

3. Verification of the modified strain development model for the biaxial restraint conditions

3.1. Expansive concrete plane elements with arbitrary orthogonal restraint

Three series of the expansive concrete plane specimens with the mesh reinforcement in the mid-depth of the cross-section were investigated during the expansive concrete hydration period. The rate of confinement in the orthogonal directions was taken as the variable parameter of test samples.

Geometry and characteristics of reinforcement and expansive concrete of the test elements are presented in the Table 1.

Table 1.   Geometry and material characteristics of plane specimens. *Source:* own study

Specimen marking	Specimen geometry, mm, bx $l$xh	Reinforcement				Expansive concrete	
		x-direction		y-direction			
		$A_{s.x}$, mm^2	reinforcement ratio $\rho_{s.x}$, %	$A_{s.y}$, mm^2	reinforcement ratio $\rho_{s.y}$, %	ε_{cf}, %	$E_{c.28}$, GPa
P1		339	0.97	58.9	0.16	0.117	42.66
P2	500x500x70	339	0.97	339	0.97	0.437	23.1
P3		58.9	0.16	58.9	0.16	0.334	33.3

$A_{s.x}$ – reinforcement area in the x-direction; $A_{s.y}$ – reinforcement area in the y-direction; ε_{cf} – free strain at the concrete expansion stabilization; $E_{c.28}$ – Young's modulus at 28 days age.

Development of the experimental values of the restrained expansion strains during the hydration period along with the calculated according to the 2D MSDM ones for the test specimens

is shown in Fig. 3. In the same Figure, the calculated according to the model [10] data are also shown to demonstrate the influence of additional cumulative force on the restrained expansion strains. It should be pointed out that the calculation of the stress-strain parameters following model [10] was carried out, taking into account the Poisson's ratio concerning the elastic part of concrete deformation.
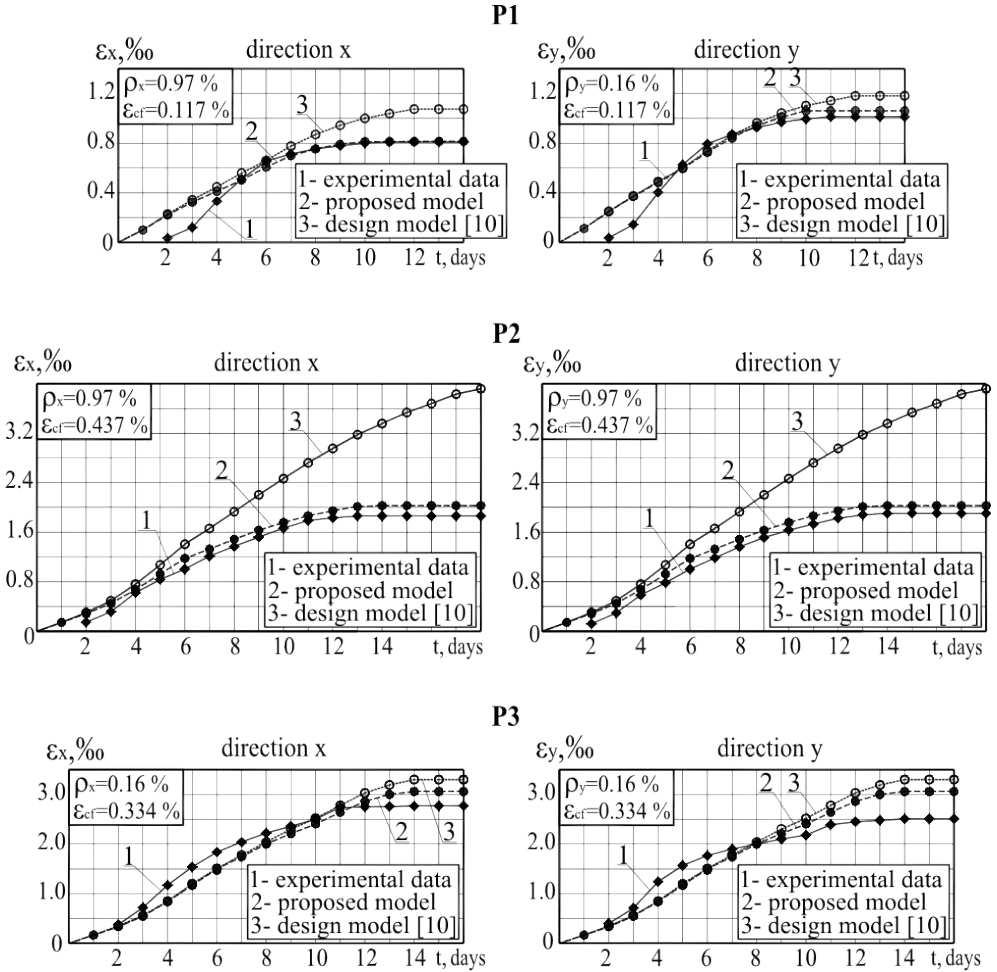
Fig. 2.   Development of the restrained expansion strains for samples P1, P2 and P3. *Source:* own study

It is useful to demonstrate the comparison of experimental and calculated values of the restrained expansion strains at the end of the expansive concrete hydration period for all test samples (see Table 2). The calculated values of the restrained expansion strains were obtained based on the model 2D MSDM as well as based on the models [3], [5], [10]. Note that the models [3] and [5] are based on the chemical energy conservation law and allow defining the stress-strain parameters of the expansive concrete elements only by the end of expansion concrete stabilization period.

Table 2.   Experimental and calculated values of the restrained expansion strains. *Source:* own study

Source	Specimen marking					
	P1 $\rho_{s.x} = 0.97\%,$ $\rho_{s.y} = 0.16\%$		P2 $\rho_{s.x} = 0.97\%,$ $\rho_{s.y} = 0.97\%$		P3 $\rho_{s.x} = 0.16\%,$ $\rho_{s.y} = 0.16\%$	
	Values of the restrained expansion strains (‰) in the direction:					
	x	y	x	y	x	y
Experimental data	0.811	1.013	1.883	1.906	2.770	2.512
Calculated values, according to the model 2D MSDM	0.813	1.061	2.031	2.031	3.063	3.063
Calculated values, according to [3]	0.860	3.070	1.470	1.470	4.610	4.610
Calculated values, according to [5]	0.792	2.850	1.240	1.240	3.793	3.793
Calculated values, according to [10]	1.074	1.183	3.915	3.915	3.286	3.286

3.2. Expansive concrete-filled steel tubes

Experimental studies were carried out on the two series of expansive concrete-filled steel tubes (EC FST) with the diameter 200 mm, length 300 mm and 600 mm and steel tube wall thickness 1.0 mm, 1.5 mm and 2.0 mm. The variation of the following parameters is considered: effective restraint ratio $\rho_{l.\theta}$ and $\rho_{l.z}$; length of steel tube (300 mm and 600 mm); self-stressing grade of expansive concrete; influence of internal curing.

Development of restrained expansion strains in time under different restraint conditions in longitudinal and circumferential directions is shown in Fig. 3.
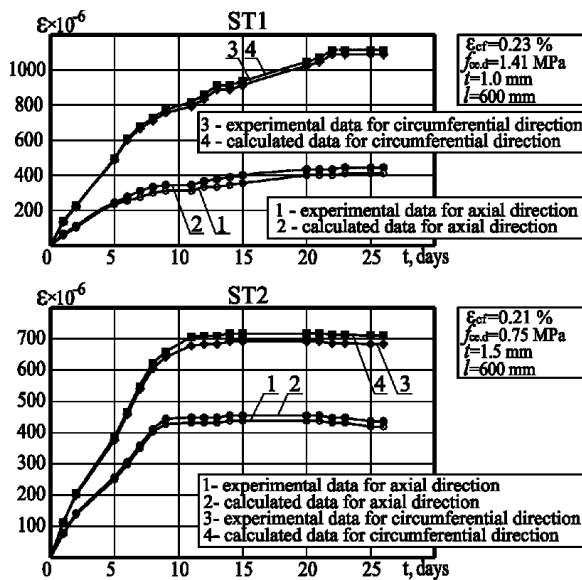
Fig. 3.   Development of the restrained expansion strains tube samples. *Source:* own study

Restrained expansion strains obtained in the experimental campaign (see Fig. 3) were compared to those calculated following the proposed model for the expansive concrete-filled steel tubes. As follows from the comparison of the results, the restrained expansion strains value calculated in accordance with the proposed model shows a good agreement with experimental data.

4. Conclusions

The modified early age strains development model for the biaxial restraint conditions based on the initial early age strain calculation approaches is universal and allows obtaining an adequate solution for any boundary conditions.

The free expansion strains development law of the expansive concrete from the early age to the end of stabilization period is accepted as the basic parameter when defining the stress-strain parameters of expansive concrete elements under biaxial restraint conditions.

The suitability of the proposed model was confirmed by the own experimental investigations of expansive concrete elements under two-way restraint conditions as well as the experimental results of expansive concrete-filled steel tubes. The difference between the experimental and calculated values of the restrained expansion strains did not exceed 25.5%.

References

[1]   Mikhailov V. and Litver S., *Expansive and self-stressing cements and self-stressed reinforced structures*. Stroyizdat, Moscow, 1974, p. 312 (in Russian).

[2]   Mikhailov V. and Gershvald V., "Plane self-stressed structures", in *Researches and usage of self-stressing concrete and self-stressed structures: NIIZHB*, 1984, pp. 62-67 (in Russian).

[3]   TCP 45-5.03-158-2009, concrete and reinforced concrete structures from self-stressing concrete: design rules, Minsk, 2010 (in Russian).

[4]   Ishikava Y., Shibata K. and Tanabe T., "Initial stress analysis of expansive material under restrictions based on chemical conservation law", in *Creep, Shrinkage and Durability Mechanics of Concrete and Concrete Structures*, 2009, pp. 437-443.

[5]   Marchuk V., *Strains and stresses of plane self-stressing concrete elements under nonsymmetrical biaxial restraint at the expansion stage*, (PhD thesis), BSTU, Brest, Belarus, 2002 (in Russian).

[6]   Litver S. and Petukhov A., "Stresses under bi-axial restraint conditions", in *Researches and usage of self-stressing concrete and self-stressed structures: NIIZHB*, 1984, pp. 67-78 (in Russian).

[7]   Man T., Wang B., Jin H. and Zhang X., "Expansion behavior of self-stressing concrete confined by glass-fiber composite meshes", in *Construction and Building Materials*, no. 128, 2016, pp. 38-46. https://doi.org/10.1016/j.conbuildmat.2016.10.022

[8]   Okada K., Ohta M., Nagafuchi T., Yata A. and Tamai S., "Characteristics of expansive concrete under bi-axial restraint", *Journal of the Society of Material Science*, no. 32, 1983, pp. 182-187.

[9]   Wang V., Han T. and Jin H., "Prediction of expansion behaviour of self-stressing concrete by artificial neural networks and fuzzy inference system", *Construction and Building Materials*, no. 84, 2015, pp. 184-191. https://doi.org/10.1016/j.conbuildmat.2015.03.059

[10] Ito H., Maruyama I., Tanimura M. and Sato R., "Early age deformation and resultant induced stress in expansive high strength concrete", *Journal of Advanced Concrete Technology*, 2004, vol. 2, no. 2, pp. 155-174.

[11] Semianiuk V., Tur V., Herrador M.F. and Paredes G.M., "Early age strain and self-stresses of expansive concrete members under uniaxial restraint conditions", *Construction and Building Materials*, 2017, no. 131, pp. 39-49.

[12] Lei H., Chengkui H. and Yi L., "Expansive performance of self-stressing and self-compacting concrete confined with steel tube", *Journal of Wuhan University of Technology-Mater. Sci. Ed.*, 2007, pp. 341-345. https://doi.org/10.1007/s11595-005-2341-2

Ductility and internal forces redistribution in lightweight aggregate concrete beams

Tomasz Waśniewski[1], Ewelina Kołodziejczyk[2]

[1] *Department of Concrete Structures; Faculty of Civil Engineering, Architecture and Environmental Engineering; Lodz University of Technology; 6 Politechniki Avenue, 90-924 Lodz, Poland; tomasz.wasniewski@p.lodz.pl* (iD) *0000-0001-7303-4920*

[2] *Department of Concrete Structures; Faculty of Civil Engineering, Architecture and Environmental Engineering; Lodz University of Technology; 6 Politechniki Avenue, 90-924 Lodz, Poland; ewelina.kolodziejczyk@p.lodz.pl* (iD) *0000-0002-3533-4145*

Abstract: Lightweight Aggregate Concrete (LWAC) is typically defined as concrete having a density smaller than or equal to 2200 kg/m^3 and can be obtained by mixing natural or artificial lightweight aggregates. There is a general scepticism regarding the use of lightweight aggregate concrete (LWAC) for structural applications. This concern is attached to the more brittle material behaviour which leads to lower ductility.

This article presents a numerical parametric analysis of the behaviour of the reinforced LWAC cross-sections under the immediate load taking into account the density of the LWAC concrete, concrete strength and tensile reinforcement ratio.

Numerical analysis of the beams was conducted in OpenSees, an open–source nonlinear finite element method framework. One-dimensional elements, with three degrees of freedom at each end, were used. Bending stiffness in the integration points was calculated based on the sectional moment – curvature relationship.

The analysis showed that there is a relationship between the ductility of the cross-sections made of lightweight concrete and its density class. It is associated with limited compressive strains and the brittle behavior of LWAC. The limited rotation capacity of the reinforced concrete sections made of LWAC also affects the ability of redistribution of internal forces in statically indeterminate beams.

Keywords: lightweight, concrete, ductility, redistribution, beams

1. Introduction

The ductility of the reinforced concrete elements can be defined as the ability to plastic deformation, in the area of permissible loads and also above it. High ductility means that the structure can transfer loads despite the overloading of its critical sections. Admittedly, excessive displacements and deflections may occur, but the load capacity of the structure will be maintained. In the statically indeterminate systems, adequate ductility ensures the ability to rotate of critical cross-sections, which allows the proper redistribution of the internal forces.

Lightweight Aggregate Concrete (LWAC) is typically defined as concrete, having a density smaller than or equal to 2200 kg/m³ and can be obtained by mixing natural or artificial lightweight aggregates [1]. There is a general scepticism regarding the use of lightweight aggregate concrete (LWAC) for structural applications. This concern is attached to the more brittle material behaviour, which leads to lower ductility [2]–[5].

This article presents a numerical parametric analysis of the behaviour of the reinforced LWAC cross-sections under the immediate load taking into account the density of the LWAC concrete, concrete strength and tensile reinforcement ratio.

Numerical analysis of the deformations and internal forces redistribution of the double-span beams made of LWAC and reinforced with different reinforcement ratio is presented. The moment-curvature relationship is used as a constitutive sectional law.

2. Material characteristics and ultimate strains in LWAC

Lightweight aggregate concrete is classified according to its density into six classes [1]. For each class and compressive strength, the material parameters such as modulus of elasticity or ultimate compressive strains are obtained from parameters of the corresponding normal weight concrete by multiplying them by coefficient:

$$\eta_E = \left(\frac{\rho}{2200} \right)^2 \tag{1}$$

where:

ρ – is the oven-dry density for the relevant class of the LWAC.

This approach results in a very large diversity of ultimate compressive strains. In figure 1, a general relationship between ultimate compressive strains, compressive strength and density of the lightweight concrete is presented. The value of the ultimate strain extends from the lowest value $\varepsilon_{lcu} = 1.13‰$ for $f_{lc} = 20$ MPa and $\rho = 2000$ kg/m³ up to the highest value $\varepsilon_{lcu} = 10.7‰$ for $f_{lc} = 80$ MPa and $\rho = 1000$ kg/m³.
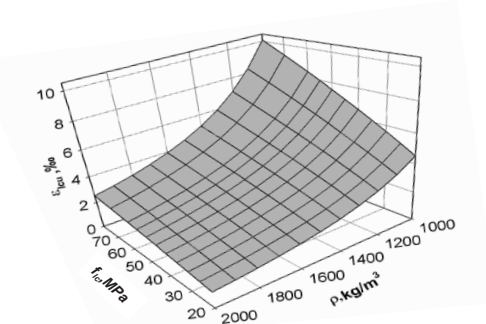

Fig. 1.   Relationship between $\varepsilon_{lcu} - f_{lc} - \rho$ for LWAC according to [1]. *Source:* own study

Figure 2 presents sigma – epsilon characteristics determined according to [1] for lightweight concrete with compressive strength $f_c = 30$ MPa and *80 MPa*. Six density classes are included. As can be observed, for both classes, as the density increases, the modulus of elasticity of lightweight aggregate concrete increases, and in all cases material characteristic is almost linear. This type of material behaviour is confirmed in several tests for different aggregates [6]. Compared to normal-weight concrete, lightweight concrete characteristic has a very steep post-peak, softening branch. For this reason, [1] requires the rejection of this part of the characteristic and assumes the strains at maximum stress are equal to the ultimate. This is similar to the behaviour of the higher strength classes of ordinary concrete.

It should be said that part of the combination of compressive strength and density of lightweight concrete, although possible to take into account according to [1], is not possible to obtain using available aggregates. However, [1] does not introduce any restrictions.
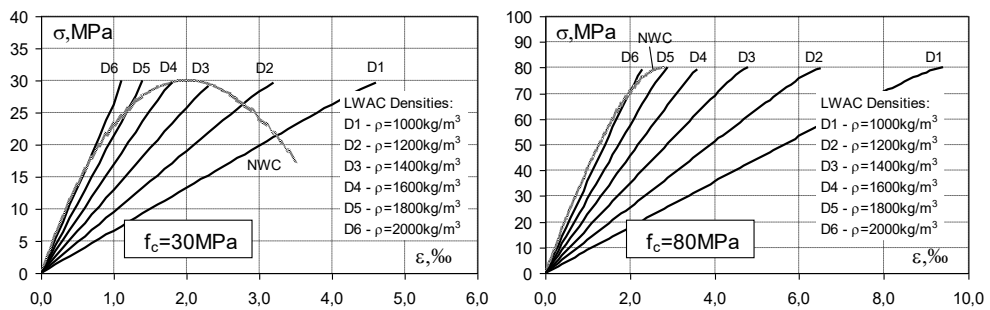

Fig. 2.   Sigma – epsilon characteristics of LWAC concrete for two selected strength classes and densities.
Source: own study

3. Ductility index

Generally, according to conventional methods of determining the ductility index, it is a function of the ultimate deformability of the concrete and the plasticity of the reinforcing steel. In practical applications, two of the most popular approaches to determining this index can be distinguished.

The first method of determining the ductility index is based on a comparison of strains or displacements corresponding to the ultimate moment M_u, and the values of these strains or displacements determined at the yielding point of the tensile reinforcement.

The second method of determining the ductility index, proposed in [7], is based on comparing the total energy needed to deform an element or cross-section to the elastic part of this energy.

In this case, the ductility index can be expressed by the following equation:

$$\mu_n = 0{,}5\left(\frac{E_{tot}}{E_{ela}} + 1 \right) \tag{2}$$

where:

E_{tot} – total energy needed for deformation, defined as the area under the graph of the force – displacement or moment – curvature relationship up to the ultimate force or moment,

E_{ela} – elastic energy determined as the area of the triangle created at the point of ultimate force or moment by a straight line; the slope of this line can be determined from the data when the element is unloaded, or from the formula:

$$S = \frac{F_{cr}S_1 + (F_y - F_{cr})S_2}{F_y} \tag{3}$$

In figure 3, a graphic interpretation of this method is presented. If the reinforcement is not plasticized in the above formula, F_u can be substituted for F_y. This method allows determining the ductility index both in elements reinforced with elastic-plastic materials and reinforced materials with purely elastic characteristics, e.g. composites.
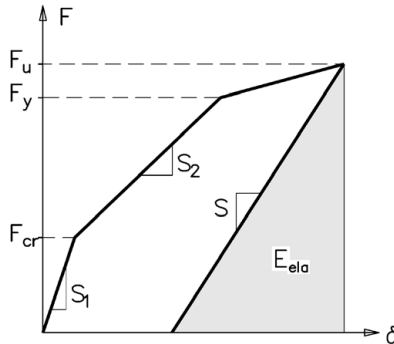

Fig. 3.   Graphical interpretation of the ductility index determination according to [7]. *Source:* [7]

Later in this article, ductility indexes will be determined using the energy method.

4. Nonlinear analysis of the cross-sections

4.1. Basic assumptions

Parametric nonlinear analysis of the reinforced cross-sections behaviour and their ductility was performed, taking into account the following parameters:

- tensile reinforcement ratio,
- compressive strength and its ultimate compressive strains,
- density of the concrete.

4.2. Calculation assumptions

In this study, the layered model of the reinforced section is presented according to [8]. This way of calculation gives good compatibility of the calculations and test results.

This method assumes the following assumptions:

- only normal stress is considered,
- the load is monotonic, singular and irreversible,
- principle of maintaining a flat cross-section is valid throughout the entire load range,
- material relationships of concrete and reinforcing steel were obtained in the uniaxial state of stresses,
- strains of the reinforcement and surrounding concrete are the same,
- non-linear stress – strain characteristic of the compressed normal and lightweight aggregate concrete is used according to [1],

- principle of tension stiffening is valid; the model is adopted according to [8],
- stress-strain relationship of tensile reinforcing steel is used according to [9],
- in sections with top reinforcement a compressed steel bars model was used according to [10].

The moment – strain or moment – curvature relationships are determined by considering subsequent levels of strain in the cross-section and obtaining by the iteration the internal forces (normal force and bending moment), which are in balance to external forces in section.

$$\sum_{i=1}^{n} P_i = N \qquad \sum_{i=1}^{n} P_i \bar{y}_i = M$$
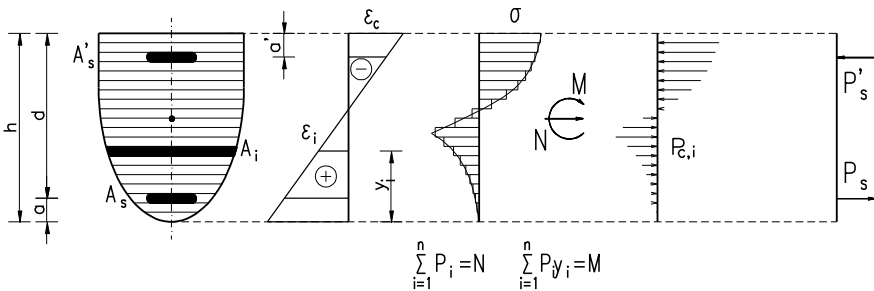
Fig. 4.   Discretization of the section and strains and stress state in the layers

The considered cross-section is divided into layers. In figure 4, the discretization of the section and example of strain and stress states in the layers are presented.

Reinforcement bars are treated as a separate layer (or several layers) of known location and cross-sectional area.

4.3. Results of the calculations

Figure 5 shows the calculated relative M-κ relationships for section reinforced with low tensile reinforcement ratio ($\rho_s = 0.01$), made of LWAC with different densities. The compressive strength of the concrete is $f_{lc} = 30$ MPa. For comparison results for normal-weight concrete are also presented.

Fig. 5.   Moment – curvature relationships for section reinforced with $\rho_s = 0.01$. *Source:* own study

As you can see, in all cases, before the yielding of the reinforcement steel, the impact of a decreasing elastic modulus along with a decrease in the density of concrete is visible.

After the steel yielding, a strong influence of the ultimate compressive strain of the concrete on the ability to plastic deformation of the cross-secti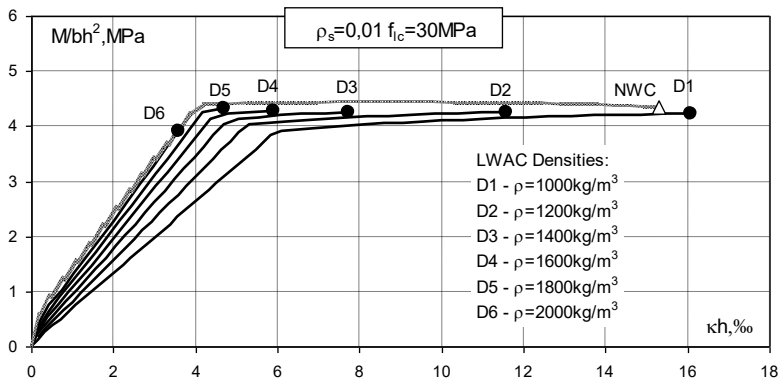on is revealed. For concretes with the highest density, the plastic branch is very short, unlike the concretes with the lowest density, where the plastic branch is clearly longer. The length of the plastic branch directly affects the ductility of the section. It can be seen that for the highest density class ($\rho_s = 2000$ kg/m^2), reinforcement is not yielding at all, and the cross-section loses any ductility.

Interestingly, compared to normal concrete, the closest cross-sectional behaviour was obtained for lightweight concrete with the lowest density class.
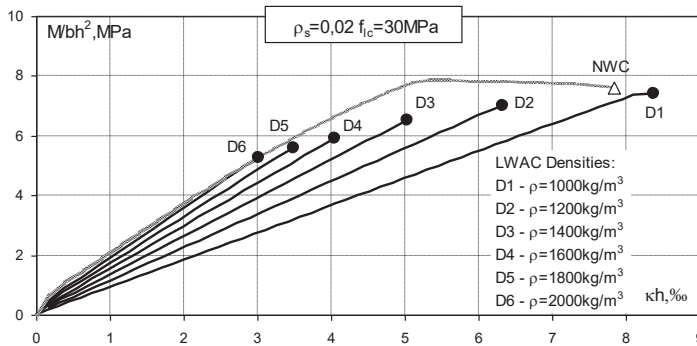
Fig. 6.   Moment – curvature relationships for section reinforced with $\rho_s = 0.02$. *Source:* own study

The impact of the limited ultimate strains is even more visible in the case of sections with a higher reinforcement ratio. Figure 6 shows the calculation for the section reinforced with $\rho_s = 0.02$. For concrete with a density above 1200 kg/m^3, the reinforcement does not yield, and the cross-section loses its ability to plastic deformation. Meanwhile, normal-weight concrete with the same reinforcement ratio still shows good ductility.

Figure 7 shows the general relationship between the ductility index and the density of concrete for two lightweight concrete compressive strengths. Calculations were carried out for several degrees of reinforcement.

Fig. 7.   The general relationship between ductility index and density for two LWAC strength. *Source:* own study

In both cases, a strong dependence of the ductility index on the density of lightweight aggregate concrete is revealed. The lower the density class, the higher the ductility. This relationship is more visible for cross-sections with a lower tensile reinforcement ratio.

In the case of concrete with compressive strength $f_{lc} = 30$ MPa, in more heavily reinforced cross-sections, where tensile reinforcement is higher than 0.01, the ductility index is very low. This is because the reinforcemen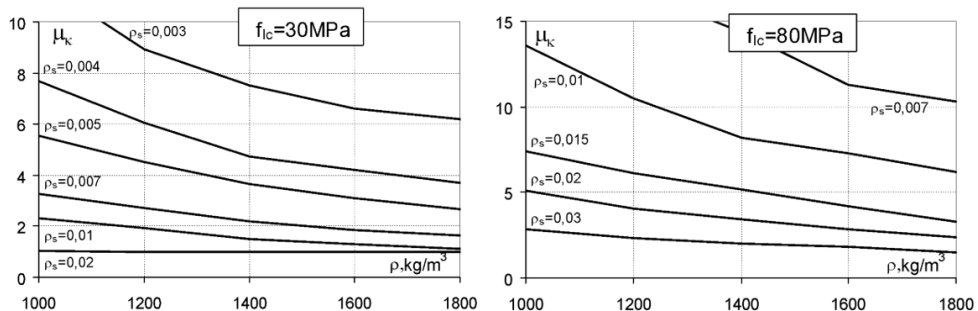t does not yield, even if the ultimate compressive strains are greater than in normal-weight concrete. In the cross – sections made of concrete with increased compressive strength ($f_{lc} = 80$ MPa), cross-sections lose their plasticity at higher levels of the reinforcement ratio. ($\rho_s > 0.03$).

5. Internal forces redistribution in the double-span beams

If in any cross-section of the statically indeterminate element or system, the bending moment values are not constantly proportional to the loads at every step load, it means that the rearrangement of internal forces or the redistribution of the bending moments occurs. In the reinforced concrete structures, the main reason for the redistribution of internal forces is the increasing change in stiffness due to cracking and reinforcement yielding.

In [1], the coefficient of redistribution, δ, is defined by eq. (3), and the degree of moment redistribution, η (in %), is defined by eq. (4):

$$\delta = \frac{M_{red}}{M_{elast}} \tag{3}$$

$$\eta = (1 - \delta) \cdot 100 \tag{4}$$

where M_{red} is the moment in the support or span section after redistribution, and M_{elast} is the moment in the same section calculated according to the theory of elasticity.
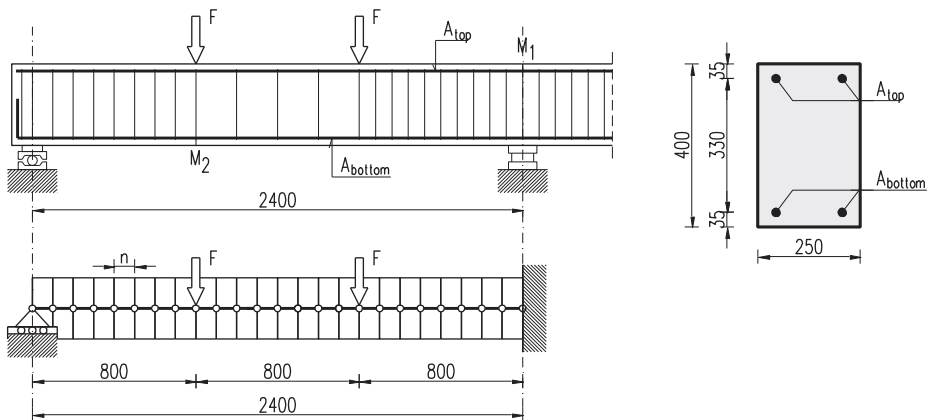
Fig. 8.   Beam geometry and the FEM discretization. *Source:* own study

Numerical analysis of the beams was conducted in OpenSees, an open–source non-linear finite element method framework. One-dimensional elements, with three degrees of freedom at each end, were used. Bending stiffness in the integration points was calculated based on the sectional moment–curvature relationship.

For analysis, the symmetrical two-span beam with a total width of 480 cm was selected. The beam was loaded in each span with two concentrated forces at a spacing of 80 cm. The cross-section of the element is 40 cm high and 25 cm wide.

Figure 8 shows the beam geometry and the discretization method for FEM analysis.

Table 1.   Summary of the geometrical and material parameters of the beams. *Source:* own study

Beam	Geometry			Reinforcement				Concrete						
	L_{span}	h	b	A_{top}	ρ_{top}	A_{bottom}	ρ_{bottom}	f_y	f_t	$f_c=f_{lc}$	ε_{lcu}	ε_{cu}	E_{lcm}	E_{cm}
	m	cm	cm	-	-	-	-	MPa	MPa	MPa	‰	‰	GPa	GPa
B1				2#16	0.0044	4#16	0.0088							
B2	2.4	40	25	4#16	0.0088	2#16	0.0044	500	675	30	1.47	3.5	20.5	30.5
B3				3#20	0.0138	2#16	0.0044							

For comparative purposes, calculations were made for beams made of lightweight concrete with a density of ρ = 1800 kg/m³ as well as normal-weight concrete. Three types of reinforcement layout were assumed for both materials. Table 1 shows a summary of all geometrical and material parameters of the beams.
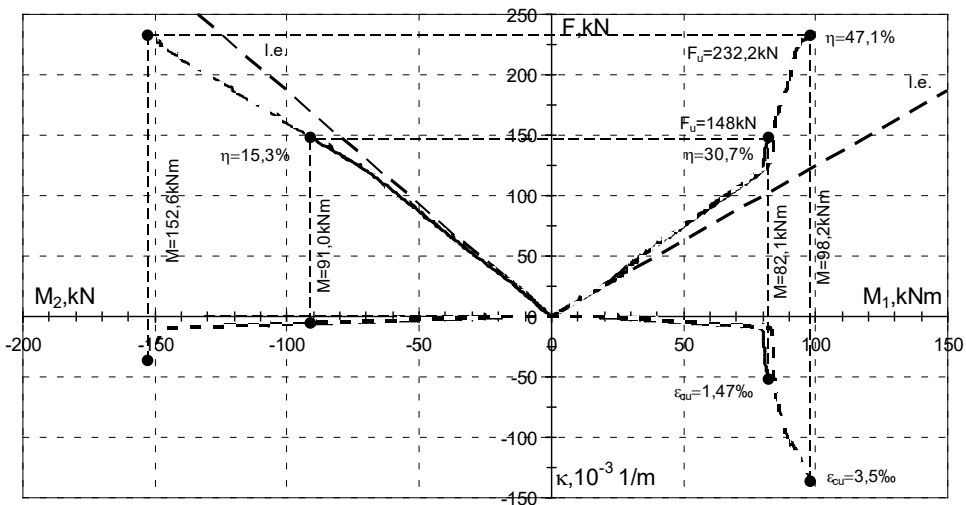
Fig. 9.   Calculated redistribution of the moments in the beam B1. *Source:* own study

Figure 9 shows the calculated impact of the ultimate curvatures on the moment redistribution and load-bearing capacity of the beam B1. The reinforcement arrangement in this beam forces the redistribution of the bending moments from the support to the spans. As we can see, the load capacity of a beam with such a reinforcement system is determined by its ability to deform the support section, both in a beam made of lightweight or normal weight concrete. However, rotation capacity depends on the ultimate compressive strains of the concrete, and those for LWAC with a density of ρ = 1800 kg/m³ are twice as low as for the normal concrete. At the ultimate curvature of the middle-support cross-section made of lightweight concrete, reinforcement does not yield in the span, and the beam's load capacity is F_u = 148 kN. Degree of redistribution at failure is η = 30.7%.

In the case of a beam made of normal concrete, for the ultimate curvature in support, the load-bearing capacity of the beam is F_u = 232.2 kN, and the reinforcement in the span starts to yield. In this case, the degree of redistribution increases to 47.1%.

The reinforcement system in B2 type beams is close to elastic – consistent, i.e. that the load capacity of the support section will be achieved simultaneously with the load capacity of the span sections.
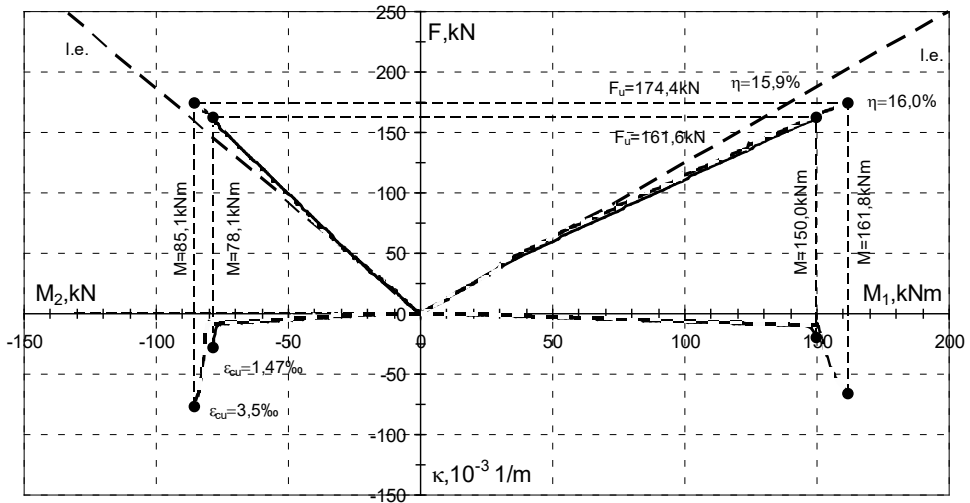
Fig. 10.   Calculated redistribution of the forces in the beam B2. *Source:* own study

In this case (Fig. 10), in both beams, made of lightweight and normal concrete, the reinforcement becomes yielding, both in the span cross-sections and in the middle support section. The differences between the load-bearing capacities are no longer as large as in the case of the B1 beam, and they are respectively F_u = 161.6 kN for a beam made of lightweight concrete, and F_u = 174.4 kN for a beam made of normal concrete. The levels of moment redistribution are the same, at η = 16%.
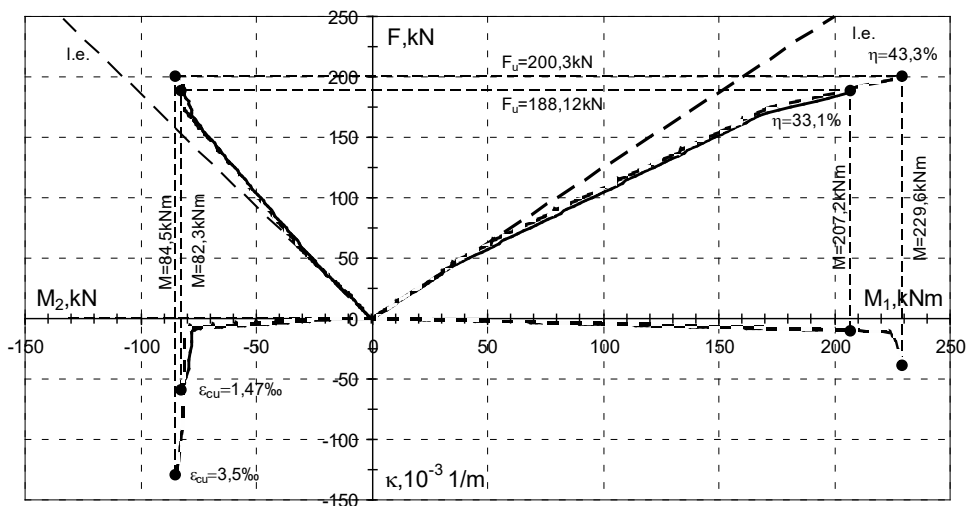

Fig. 11.   Calculated redistribution of the forces in the beam B3. *Source:* own study

In the last analyzed beam B3, the reinforcement was selected to force a strong redistribution of bending moments from the span to the middle support. Figure 11 shows the calculated impact of the ultimate curvatures on the moment redistribution in this beam.

As can be observed, in this case, the load-bearing capacity of the beam is determined by the ultimate deformability of the cross-sections in the span. For a beam made of normal concrete, the load capacity was $F_u = 200.3$ kN, and for a beam made of LWAC, the limit curvature of cross-sections in the span allowed to achieve the load capacity $F_u = 188.1$ kN. The redistribution degrees were 43.3% and 33.1%, respectively. The lower deformability of the sections made of LWAC again reduced the redistribution of moments relative to ordinary concrete.

6. Conclusions

The following conclusions can be drawn from the computational analysis of sections and beams made of lightweight concrete:

- the ductility of the cross-sections made of lightweight aggregate concrete depends on the density of the concrete and associated with it ultimate compressive strains,
- smaller ultimate compressive strains of the LWAC reduces the plastic branch length of the moment – curvature relationship; this affects the ductility index,
- the lower the density of lightweight concrete, the greater the ductility index of the cross-section,
- tendency mentioned above is more visible for cross-sections with a lower reinforcement ratio,
- the limited deformation capacity of the cross-sections made of lightweight aggregate concrete limits the redistribution of bending moments in the statically indeterminate beams compared to the beams made of normal weight concrete. This is especially visible in the beams reinforced in the non-elastic-consistent way (over-reinforced span or support cross-sections),
- in some extreme cases, the limited rotational capacity if the cross-section in middle support will not allow yielding of the reinforcement in the spans and will strongly reduce the load capacity,

It should be said that normal-weight concrete cannot be freely replaced with LWAC only taking into account compressive strength. When designing reinforced concrete elements made of lightweight aggregate concrete, it is necessary to take into account its limited deformation capabilities and the associated redistribution of internal forces. It is recommended that the rotational capacity of the cross-sections in statically indeterminate elements should be controlled in each case.

References

[1]   European Committee for Standardization. EN 1992-1-1 Eurocode 2: Design of concrete structures Part 1-1: General rules and rules for buildings. CEN, Brussels, 2004.

[2]   Øverli J.A., Jensen T.M., "Increasing ductility in heavily reinforced LWAC structures", *Engineering Structures*, vol. 62-63, (15 March 2014), pp. 11-22.

[3]   Carmo N.F., Costa H., Simões T., Lourenço C., Andrade D., "Influence of both concrete strength and transverse confinement on bending behavior of reinforced LWAC beams", *Engineering Structures*, vol. 48, (March 2013), pp. 329-341.

[4]   Dias-da-Costa D., Carmo R.N.F., Graça-e-Costa R., Valença J., Alfaiate J., "Longitudinal reinforcement ratio in lightweight aggregate concrete beams", *Engineering Structures*, vol. 81, (15 December 2014), pp. 219-229.

[5]   Øverli Jan A., "Towards a better understanding of the ultimate behaviour of LWAC in compression and bending", *Engineering Structures*, vol. 151, (15 November 2017), pp. 821-838. https://doi.org/10.1016/j.engstruct.2017.08.063

[6]   Liu, X., Wu, T., & Liu, Y., „Stress-strain relationship for plain and fibre-reinforced lightweight aggregate concrete", *Construction and Building Materials*, vol. 225, 2019, pp. 256-272. https://doi.org/10.1016/j.conbuildmat.2019.07.135

[7]   Naaman A.E., Jeong S.M., "Structural ductility of concrete beams prestressed with FRP tendons", in *2nd Int. RILEM Symp. (FRPRXS-2), Non-Metric (FRP) Reinforcement for Concrete Structures*. RILEM, Bagneux, France, 1995, pp. 379-386.

[8]   Czkwianianc A., Kamińska M.E., „Metoda nieliniowej analizy żelbetowych elementów prętowych", *Studia z zakresu inżynierii*, nr 36 (Institute of Fundamental Technological Research Polish Academy of Sciences, Warsaw, Poland, 1993).

[9]   Mander J.B., Chang G., "Seismic energy based fatigue damage analysis of bridge columns: Part I – evaluation of seismic capacity", Technical Report 94-0006, NCEER, 1994.

[10]   Maekawa K., Dhakal P.R., "Path-dependent cyclic stress-strain relationship of reinforcing bar including buckling", *Engineering Structures*, vol. 24, 2002, pp. 1383-1396. https://doi.org/10.1016/S0141-0296(02)00080-9

[11]   The Open System for Earthquake Engineering Simulation Manual, Berkeley University of California, Available: https://opensees.berkeley.edu/wiki/index.php/OpenSees_User [Accessed: 01 February 2020]

Crossref
Similarity Check
Powered by iThenticate

The buildings of the John Paul II Centre
– a challenge for civil engineering and architecture

Bogumił Wrana[1], Jan Wrana[2]

[1] *Department of Faculty of Civil Engineering; Cracow University of Technology; 24 Warszawska Street, 31-155 Cracow, Poland; bwrana@interia.pl* iD *0000-0001-6311-1937*
[2] *Department of Faculty of Civil Engineering and Architecture; Lublin University of Technology; 40 Nadbystrzycka Street, 20-618 Lublin, Poland; j.wrana@pollub.pl* iD *0000-0002-4884-0418*

Abstract: The buildings of the John Paul II Centre (CJPII) are located in Cracow-Łagiewniki on a heap of limestone sediments from the former "Solvay" Sodium Plant in Kraków. The area is called "Białe Morze" (White Seas) and is located in the natural depression of the Wilga river valley, between Św. Józefa hill in the north and Góra Borkowska hill in the southwest. The limestone sediments as a building substrate for CJPII buildings is unprecedented ground in the world and thus a challenge for civil engineering.

The height of the heap reaches about 15 m and has retained the consistency of a white pulp until today. CJPII buildings are objects of the third geotechnical category, founded on a foundation slab of 0.8-m thickness, and in the central part of 0.45-m thickness. The slab is based on 200 reinforced concrete CFA-type drilled piles with a diameter of 1000 mm and 650 mm and length up to 26 m. The load-bearing structure of the CJPII buildings is a reinforced concrete frame and shell structure.

The symbolism of the urban complex (e.g. the scale of the market square in Wadowice) located on a system of 200 piles, above the post-industrial landfill/heaps of sediments – ensuring its protection by architectural solutions referring to places connected with the life of JPII (the Wawel Cathedral, St. Mary's Basilica in Cracow) with the adopted natural material solutions (brick and white stone) recalling the ways of combining them, and used on the facades of the emerging JPII buildings.

Keywords: John Paul II Centre in Cracow, limestone sediments, CFA-type drilled piles, reinforced concrete, natural material solutions, respect for context and identity of the place

1. Introduction

The John Paul II Centre complex is set in very unusual geotechnical conditions. Located in Krakow's Łagiewniki district, it is known as the "White Seas". The ground is a massif built of post-production waste from the former "Solvay" Sodium Plant in Cracow, in the form of

limestone sediments in a plastic state, locally rocked, with a thickness of up to 20 m. The surface of the area has been subject to reclamation by laying about 0.5 m of soil.

According to the Polish pile standard (PN-83/B-02482), the layer of sediments was regarded as a non-built embankment with zero load capacity. The monumental character of the investment was not without significance here – it was one of the most important factors why the designer of the foundation decided to take such far-reaching precautions. The Polish standard and Eurocode 7 (PN-EN 1997-1 and 2) were used to design the foundation. For the purposes of the project, the testing of the substrate was extended to CPTU static test. The level of foundation was assumed in the layers of native soils, located below the embankments. The following pictures Fig. 1 to 3 show archival photographs of the "White Seas" area.

Fig. 1.   White Seas in the 1970s. *Source:* the archive of Bogumił Wrana

Fig. 2.   White Seas in the 1990s. *Source:* the archive of Bogumił Wrana

Fig. 3.   The ground before starting construction works. *Source:* the archive of Bogumił Wrana

2. Geotechnical parameters of soil

Test drillings

As part of the field research, 6 holes were drilled with the rotary-percussive system using a mechanical drilling rig in casing pipes with a diameter of ø = 225 mm in the depth range from 26.0 m to 33.0 m. Soil samples were taken every 2 m (Nu – from non-cohesive soils, NW – from cohesive soils). Soil samples had a volume of about 1.0 dm³. Soil samples of intact structure (NNS) were taken from limestone and cohesive soils for laboratory tests of mechanical parameters.

CPT static penetration test was performed in 7 research profiles in the depth range from 14.3 m to 22.7 m BGL The interpretation of the soil profile (division into cohesive and non-cohesive soils) was performed according to Robertson's nomogram [1986], while the soil types were determined taking into account the adjacent drilling profiles and the measured values of the friction coefficient R_f. For the limestone sediments, the undrained shear strength s_u was calculated.

Hydrogeological conditions

In the analyzed area there is one quaternary aquifer related to sand and gravel formations of river accumulation. The water table is slightly stretched by silt layers drilled at the depth of 15.3 m to 24.1 m. Chemical analysis of the water sample showed slight concentrations of heavy metals (chromium, zinc, copper, nickel, lead). The water had a weak level of chemical aggressiveness in relation to concrete.

Division into geotechnical layers

Four main geotechnical layers were distinguished:

Geotechnical layer I - anthropogenic soils formed as part of the development of a limestone landfill. This layer includes about 0.3 m to 0.5 m of humus and sand, rubble and slag embankment in the OW-3 borehole to the depth of 4.2 m.

Geotechnical layer II – limestone sediments heterogeneous in terms of composition and density. The sediments are characterized by the CPT cone resistance q_c = 2-3 MPa, locally

occurring layers with values q_c = 10-20 MPa. The results of strength testing of sediments indicate that they are low-strength soils. Moreover, their high sensitivity to changes of humidity should be taken into account. Under the influence of water, they quickly become plasticized, which causes a deterioration of strength parameters.

Geotechnical layer III – Wilga river sediments located directly under the limestone sediments with a thickness of about 10 m. Within this layer, four sublayers were separated:

(Layer III a) – silt, locally peat in the hard plastic state I_L = 0.25;

(Layer III b) – clay, silt with sand intercalations, locally silt in the hard plastic state I_L = 0.0-0.1;

(layer III c1) – medium sands, with clays intercalations, in the medium-dense state I_D > 0.6;

(layer IIIc2) – medium density sand gravels and clayey sand-gravel mix, I_D > 0.6.

Geotechnical layer IV – Miocene silt developed as silt, silt, compact clay, clay.

3. Solution of building foundations

The following method of building foundation was adopted:

a) **The St. John Paul II Church** – a third geotechnical category building, founded on a foundation slab which is 0.8 m thick, and in the middle part 0.45 m thick. The slab is based on CFA type drilled piles with a diameter of 1000 mm and 650 mm and a length of up to 23 m. Due to the importance of the building and weak soil in layer II (limestone sediments), the piles are embedded in layer III, carrying the full permanent and usable load of the building.

b) **The Volunteer Centrebuilding** – a third geotechnical category building, founded on a 0.8 m thick foundation slab. The slab is based on CFA-type drilled piles of 650 mm diameter and 23 m length. Due to weak soil in layer II (limestone sediments), the piles are submerged in layer III, carrying the full permanent and usable load of the building.

c) **The Institute building** – a third geotechnical category object, founded on a 0.8 m thick foundation slab. The slab is based on CFA type drilled piles of 650 mm diameter and 23 m length. Due to weak soil in layer II (limestone sediments), the piles are submerged in layer III, carrying the full permanent and usable load of the building.
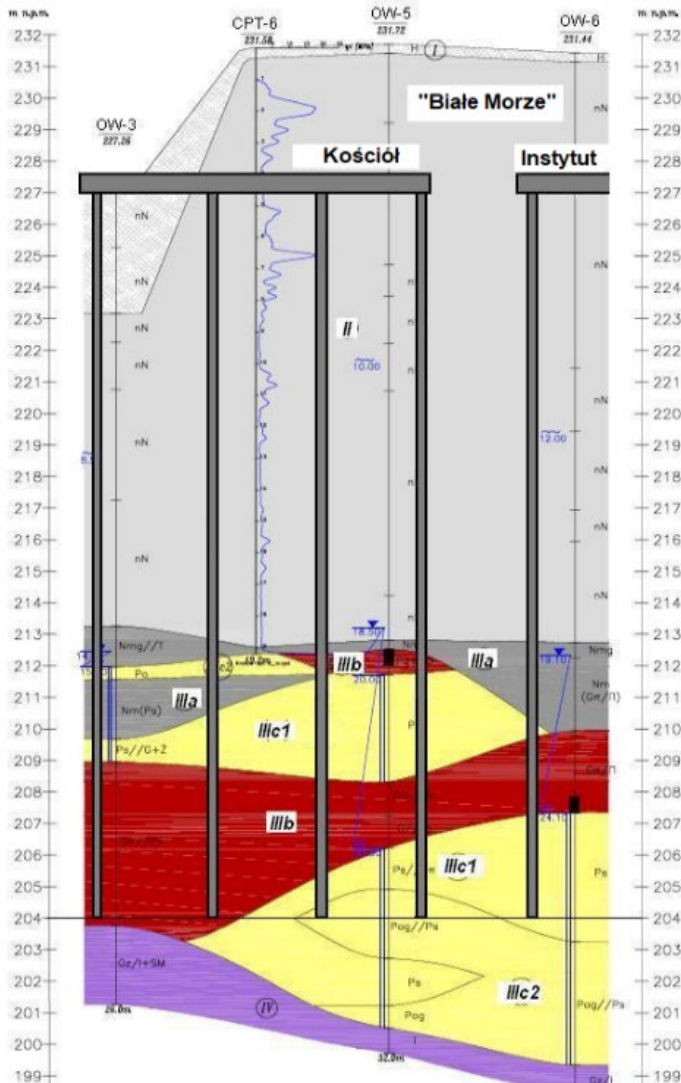
Fig. 4.   Geotechnical cross-section with foundations of John Paul II Centre facilities (The church, White
Seas, The Institute). *Source:* the archive of Bogumił Wrana. (glossary see to side. no 3)

4. Load-bearing system

The load-bearing system of the buildings is a reinforced concrete slab-column-disk
system with stiffening walls, staircases with a lift shaft and a system of transverse and longi-
tudinal reinforced concrete walls. The layout of the walls has been adapted to the layout of
the rooms approved in the construction design. The thickness of reinforced concrete walls:
external 30 cm, internal 25 cm and 20 cm of C30/37 concrete.

The construction of the underground part consists of external reinforced concrete walls
35 cm and 30 cm thick, internal reinforced concrete walls 30 cm, 25 cm, 20 cm thick and
reinforced concrete pillars.

5. Foundation of the buildings

Table 1 presents the type of foundation of the John Paul II Centre buildings.

Table 1.   Foundation of the buildings of the John Paul II Centre

Building	The area of foundation slab	Volume of concrete
The church	80 cm thick slab – 1 910 m^2 45 cm thick slab – 560 m^2	1 780 m^3
John Paul II Institute	80 cm thick slab – 1 400 m^2	1 120 m^3
The Volunteer Centre	80 cm-thick slab – 592 m^2	474 m^3
Total	4 462 m^2	3 374 m^3

The slabs are based on CFA type drilled reinforced concrete piles with a diameter of 650 mm and 1000 mm of C30/37 concrete with a length of 26.0 m.
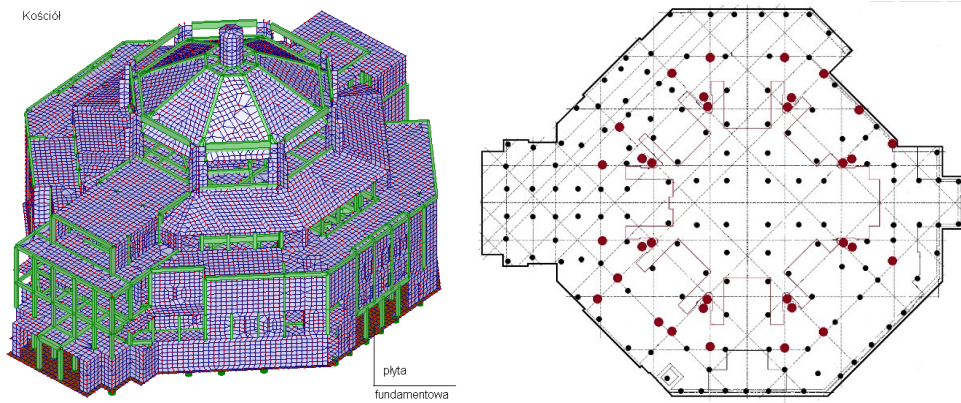

Fig. 5a.   The church. *Source:* the archive of Bogumił Wrana. (see to table no 2)
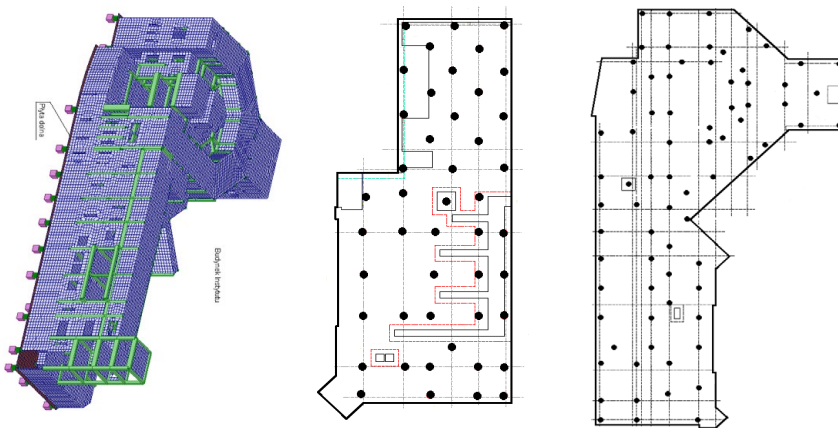

Fig. 5b.   The Centre building. *Source:* the archive
of Bogumił Wrana. (see to table no 2)

Fig. 5c.   The Institute building.
Source: the archive of Bogumił
Wrana. (see to table no 2)

6. Test plot – pile bearing capacity test

The standards for calculating the load bearing capacity of foundation piles are based on the results of field tests of the load bearing capacity of many thousands of piles. In the case of untypical construction soil, occurring only in particular areas, the design standards do not provide a credible way to determine the load bearing capacity.

The area of the White Seas has an atypical, particular soil. In this case, it was proposed that piles were constructed, and their load-bearing capacity were tested in the area of the future investment before the commencement of the design and construction process. It was proposed to construct test piles in the area of the future investment. The soil layers were removed up to the foundation level and 7 test piles and 10 retractable piles were constructed for the load-bearing capacity test.

The following test piles were made:

- in CFA technology: 2 piles $\Phi = 650$ mm; 2 piles $\Phi = 800$ mm; 1 pile $\Phi = 1000$ mm;
- in VDP technology (Vibrex): 2 piles $\Phi = 408$ mm;
- 10 retractable piles $\Phi = 650$ mm.

Fig. 6.   Test plot – pile bearing capacity testing. *Source:* the archive of Bogumił Wrana. (see above)

Table 2 below presents the results of the load bearing capacity tests of test piles.

Table 2.   Results of load bearing capacity tests of piles

Pile no.	P3	P4	P2	P6	P5	P1	P7
Production technology	CFA	CFA	CFA	CFA	CFA	VDP	VDP
Diameter [mm]	650	650	800	800	1000	406	406
Length [m]	23.0	23.0	23.0	23.0	23.0	15.0	23.0
Max. force during the test Q_{test} [kN]	3500	3500	4400	4400	5100	2250	3000
Subsidence at force 100% N_t [mm]	1.89	2.93	1.78	2.19	1.44	10.23	2.59
Permanent subsidence after the cycle I [mm]	0.44	1.46	0.55	0.81	0.32	5.88	0.57
Subsidence at force Q_{test} [kN]	9.88	16.23	7.57	14.01	6.05	49.55	13.78
Permanent subsidence after the cycle II [mm]	5.14	11.09	3.55	9.90	3.57	42.41	6.99
Measured load bearing capacity of the pile N_k [kN]	2844	2406	3575	3300	4144	1688	2063

7. Results of calculations of pile load bearing capacity

Calculations according to Polish standards

On the grounds of the recorded resistance under the q_c cone, the values of soil parameters were determined based on correlations according to PN-B-04452:2002. The layer of limestone embankment, which lies at a depth of 17.5 m BGL, was treated as cohesive soil of plastic and soft plastic consistency. Based on the I_D and I_L parameters determined in accordance with the Polish standard PN-83/B-02482, unit values of resistance under base q and along the pile shaft t were assumed. The base of the piles was placed at a depth of approx. 26.0 m BGL, in a layer of medium-density sands. The pile was, therefore, submerged at a depth of approx. 8.5 m in the native soil layer.

Calculation according to Eurocode 7

The calculation procedure presented in Annex D.7 of EN 1997-2 uses directly measured resistance values q_c under the static probe cone. Soils with q_c value less than 2.0 MPa are considered as non-bearing layers. The final load bearing capacity of the pile under consideration is $R_{c;d} = 2632$ kN, including load bearing capacity of the base $R_{b;d} = 2280$ kN and load bearing capacity of the shaft $R_{s;d} = 352$ kN.

Analysis of the results

The difference in the results of the calculations performed by the two standard procedures is significant. The design procedure according to Polish standards estimates the load bearing capacity of an exemplary pile at the level twice lower than the Eurocode 7 procedure using directly the CPT test results. The main reason for the differences is the way of using the results of static tests for the evaluation of soil parameters. The direct use of static test results for the assessment of unit resistance of the base and side of the pile, established in the Eurocode 7 procedure, leads to higher values of these parameters. It should be noted that the higher value of the total load capacity of the pile was influenced by the load bearing capacity of the pile base, resulting directly from the assumed values of unit resistance, which for Polish standards is only $q = 1.71$ MPa, while according to Eurocode 7 $p_{max;base} = 6.99$ MPa
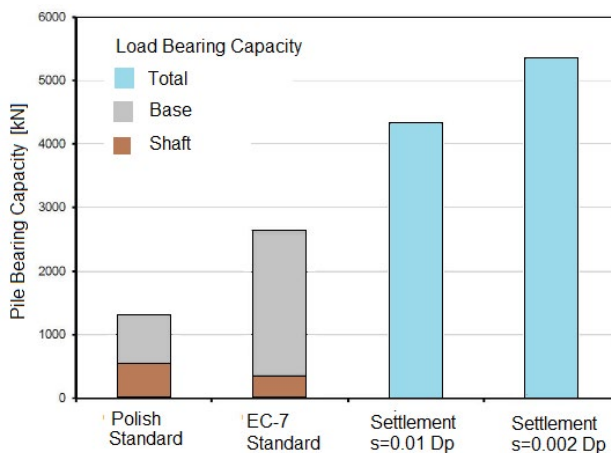

Fig. 7.   The comparison of results of the load bearing capacity tests. *Source:* the archive of Bogumił Wrana

The assessment of the load bearing capacity of the pile shaft turned out to be more cautious according to Eurocode – the lowest non-bearing layer was located here at a several meters lower level than according to Polish standards.

The figure 7 shows a comparison of the design load bearing capacity of the pile determined according to the Polish standard and the European standard. In the investigated soil conditions of White Seas area, the design pile load bearing capacity according to the European standard is much higher than according to the Polish standard. The measured load bearing capacity of the pile, in the load bearing capacity test carried out in the area of the test plot, turned out to be higher than the load bearing capacity calculated according to the standards.

8. The John Paul II Centre (CJP II)

The area where the John Paul II Centre (CJP II) has been constructed since 2008 is located, according to the current administrative division of the city, in the district IX of Kraków; Łagiewniki-Borek Fałęcki.

Łagiewniki is the first part of the current IX district of Kraków (a village located on the bank of the Wilga river, basin of the Vistula river, the name of which has been mentioned since 1373) as a knight's property. From the late fifteenth century, the area has belonged to the Castellan of Cracow (the manor buildings preserved to this day date back to the nineteenth century). Until the 18th century, the village was managed by leaseholders; in the second half of that century, the imperial route from Vienna to Lviv was marked out by Łagiewniki and Borek Fałęcki (nowadays it is Zakopiańska Street – an exit road in the direction of Zakopane). The second part of District IX is the area of the village of Borek Fałęcki (the name comes from coniferous forests with the dominating Góra Borkowska hill, first mentioned in 1392. After the First Partition of Poland, the village became a private property, where in the 19th and 20th centuries the industry developed (as a result of discoveries of shale clay and gypsum, limestone. Due to this fact, numerous brickyards, mills and industrial plants we-re built. During the period of the Austro-Hungarian partition, an "industrial zone" was created on the south of the Vistula (in the vicinity of the then Dębniki -the present districts of XI Podgórze, and IX Łagiewniki -Borek Fałęcki). At the end of the 19th century, a section of the railway line to Oświęcim runs through Borek Fałęcki with Borek Fałęcki stop.In 1901„Pierwsza Galicyjska Fabryka Sody Amoniakalnej S.A." (First Galician Soda Ash Factory S.A.) was established in this area (near the rich deposits of limestone -a raw material for the production of sodium), and after obtaining permission, was launched in 1906 by Bernard Lebanon. Three years later, he leased the factory to the Belgian concern "Solvay". (Ernest Solvay 1838 -1922, is chemist, inventor, industrialist). The expanded plant, after the completion of a narrow w gauge railway line in 1918 for transport of the raw material from a distance of 4 km (quarry in Zakrzówek – the current district of Dębniki), was bought by the Solvay concern in 1921. The management of the expanded plant decides to buy the parcel of land by the Wilga river, where it started storing white waste. After a few dozen years, a high embankment was built in the area called "White Seas" by the inhabitants of Cracow. After the change of the political system, as a result of an assessment during which it was found that the factory had been heavily polluting the environment, it was liquidated between 1989-1996. During the occupation, the sodium factory was transformed into Ostdeutsche Chemische Werke GmbH, employing German managers. Karol Wojtyła, a student living with his father in neighbouring Dębniki at 10 Tyniecka Street -15 minutes from the Wawel Cathedral, after interrupting his Polish studies in 1939 (started in 1938 at the Jagiellonian University), initially began working as a shop messenger, and since September 1940 in

a quarry in Zakrzówek (it should be mentioned that employment in the German factory protected him from being transported to the Reich for forced labour). On February 18th 1941 Karol Wojtyła's father died. At the age of less than 21, he became an orphan (at the age of 9 he lost his mother and at the age of 12 he lost his older brother). In the summer of 1941 Wojtyła moved from the quarry to the factory in Borek Fałęcki[1]. In 1944 he stopped working in the Solvay factory (earlier, in October 1942, he started studying at the secret classes of the Jagiellonian University.

A house that Karol Wojtyla never had; *In Wadowice he lived in a rented apartment, in Cracow as a student – somewhere in the basement of a house belonging to a relative on the side of Emilia's mother, as a priest he resided in the parish, as a bishop in the curia, and as Pope at the Apostolic Palace…*[2] – currently, it's called the House of St. John Paul II
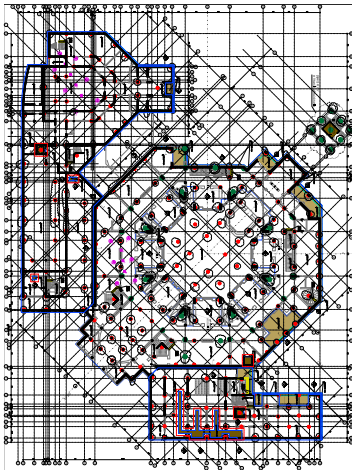

Fig. 8.1   Foundation lower slab (on the pillars) of the main unit (part of the urban complex); a. The church, b. The Centre building, c. The Institute building. *Source:* the archive of Bogumił Wrana
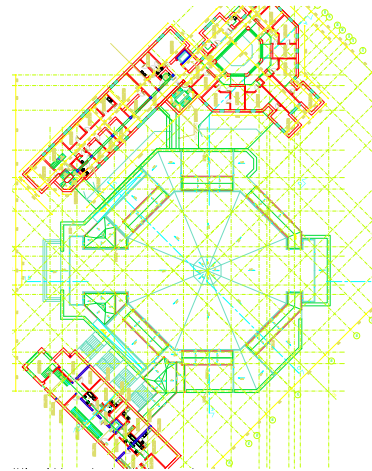
Fig. 8.2.   Foundation upper slab of the main unit (part of urban complex); a. The church, b. The Centre building with marked pile spacing, c. The Institute with sketched buildings. *Source:* the archive of Bogumił Wrana

The symbolism of the urban complex (e.g. the scale of the market square in Wadowice) located on a system of 200 piles, above the post-industrial landfill/heaps of sediments ensuring its protection by architectural solutions referring to places connected with the life of JPII (the Wawel Cathedral, St. Mary's Basilica in Kraków) with the adopted natural material solutions (brick and white stone) recalling the ways of combining them, and used on the facades of the emerging JPII buildings.

---

[1]   "His colleagues from those times, whose memories, despite many hardships, were collected by the invaluable Mrs. Karolina Biedrzycka (in the book „Ten człowiek w drewniakach. Solvay 1940-1944"), stressed that Karol was always modest and quiet, very calm, thoughtful and serious, actually too serious for his age. He always walked with his head, in too big a shirt and clogs without socks. Some people also remembered the rubber jacket he was wearing." [after:] A. Bujak, J. Sosnowska, Dom Świętego. Sanktuarium św. Jana Pawła II, Wydawnictwo Biały Kruk sp. z o.o. Kraków 2015.

[2]   Ibid. p. 21

Solutions in terms of colours and materials, (evoking places connected with the life of JP II): (Figs. 8.1, 8.2, 9.a, 9.b, 9.c, 10.a, 10.b, 10.c, 11.a, 11.b, 11.c) 2. and inspirational of interior mosaics (Figs. 12.a, 12.b, 12.c, 12.d, 13.a, 13.b, 13.c, 13.d).

a)

b)

c)

d)

Fig. 9. a, b, c The John Paul II Centre, first buildings: St. John Paul II Sanctuary, the Volunteer Centre, the John Paul II Institute of Intercultural Dialogue and a tower with a terrace and bell. Fig d. Direct communication by tram, bus, car (a route with a tunnel under Zakopiańska Street under construction (Source: own photographs of J. Wrana). *Source:* the archive of Jan Wrana

a)

b)

c)

Fig. 10.   The Wawel Cathedral

a)

b)

c)

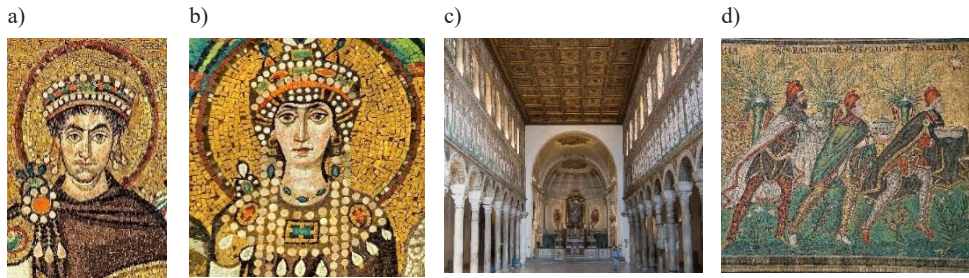Fig. 11.   St. Mary's Basilica

a)   b)   c)   d)

Fig. 12.   Inspirational mosaics – early Christiam mosaics (the church of San Vitale and Basilica of Sant'Apollinare Nuovo in Ravenna) on the way of creating contemporary mosaic decoration of the "theology of mosaics" temples by mosaic author Marko Ivan Rupnik at the JPII Centre
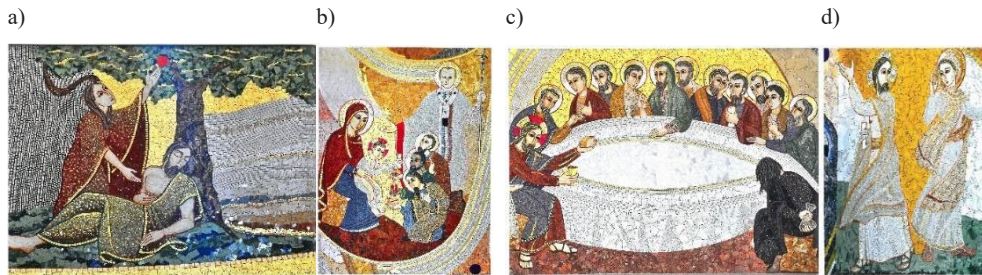
a)   b)   c)   d)

Fig. 13.   Mosaic in the JPII Centre Sanctuary

The newly established "Have No Fear" John Paul II Centre is a continuation of the work started by the John Paul II Institute, established in 1995 by Cardinal Franciszek Macharski in order to "deepen the knowledge of the Person and work of Cardinal Karol Wojtyła, professor of ethics and shepherd of the Archdiocese of Cracow"[3].

The "Have No Fear" John Paul II Centre is being built on an area formed from the post-production sludge of the former "Solvay" Sodium Plant[4] – the limestone sediments as a construction base for the CJPII buildings is an unprecedented ground in the world and has thus became a challenge for civil enginnering, but on the other hand, it is a very important symbol of the complex – *referring to the words "You are a rock"*. It built a permanent independent foundation for the *"Good Shepherd"* house with inspiration / architectural and material solutions (brick and white stone) evoking places connected with the life of JPII (tenement houses in Dębniki and Podgórze in Kraków, the Wawel Cathedral, St. Mary's Basilica, tenement houses on Kanonicza Street, early Christian temples in Ravenna and Venice, Archbasilica of St John Lateran, St. Peter's Basilica in Rome proposed by Andrzej Mikulski – graduated from the Cracow University of Technology. The way of creating contemporary mosaic decoration of the temples, "theology of mosaics", by mosaic author Marko Ivan Rupnik in the JPII Centre.

"The main institutions of the Centre that were established until 2019: "The John Paul II Sanctuary, the Volunteer Centre, the John Paul II Institute of Intercultural Dialogue, a tower with

---

3   Ibid. p. 24
4   Ibid. p. 24

a viewing terrace and bell tower, and the Museum building. The next stages will be: Pilgrim's House, Retreat House, Conference Centre and Rehabilitation Centre"."

Due respect for the work of Karol Wojtyla and his friends – workers in Solvay during the war – is expressed by the preserving the steel footbridge (once a technological bridge for the transport of waste) connecting the Centre's grounds with the rest of White Seas and the direction of the pedestrian route which it marks.[5]

References

[1] Wrana B., *Projekt budowlany posadowienia obiektów Centrum Jana Pawła II na „Białych Morzach"*. BOMES, Kraków, 2009.

[2] Czado B., Domski J., Wrana B., „Optymalizacja posadowienia palowego obiektów Centrum Jana Pawła II w Krakowie-Łagiewnikach", in *Materiały Seminarium IBDiM i PZWFS Wzmocnienie podłoża i fundamentów*, Warszawa, 2014.

[3] Wrana B., Czado B., „Zastosowanie wyników testu CPT do oceny nośności pala", *Górnictwo i Geoinżynieria*, vol. 35, no. 2, pp. 605-611.

[4] Wrana B., *Lectures on Soil Mechanics*. Wydawnictwo Politechniki Krakowskiej, Kraków, 2014.

[5] Wrana B., *Lectures on Foundation Design*. Wydawnictwo Politechniki Krakowskiej, Kraków, 2016.

[6] Wrana B., „Pile load capacity – calculation methods", *Studia Geotechnica et Mechanica*, vol. 37, no. 4, 2015, pp. 83-93.

[7] Robertson P.K., Campanella R.G., Gillespie D., Greig J., "Use of piezometer cone data", in *Proceedings of the ASCE Specialty Conference In Situ '86: Use of In Situ Tests In Geotechnical Engineering*, pp. 1263-1280, Blacksburg, 1986.

[8] EN 1997-1, Eurocode 7: Geotechnical design – Part 1: General rules.

[9] EN 1997-2, Eurocode 7: Geotechnical design – Part 2: Ground investigation and testing.

[10] PN-B-02482:1983 – Fundamenty budowlane. Nośność pali i fundamentów palowych.

[11] ISO 14688-1: Geotechnical investigation and testing – Identification and classification of soil – Part 1: Identification and description.

[12] ISO 14688-2: Geotechnical investigation and testing – Identification and classification of soil – Part 2: Principles for the classification.

[13] Wrana J., *Tożsamość miejsca – kryterium w projektowaniu architektonicznym*. Politechnika Lubelska, Lublin, 2011.

[14] Wrana J., *Eseje o tożsamości miejsca. Wybrane artykuły dotyczące tożsamości i kontekstu.* Politechnika Lubelska, Lublin, 2012.

[14] Wrana J., „Architektura – zrozumiały komunikat przestrzenny", *Czasopismo Techniczne*, PK, no. 15, 2010.

[15] Wrana J., „Architektura z poszanowaniem miejsca", *Budownictwo i Architektura*, vol. 9, no. 2, 2011, pp. 129-139.

[16] Wrana J., Fitta A., „Architektura a kontekst miejsca", *Budownictwo i Architektura*, vol. 11, no. 1, 2012, pp. 5-13.

[17] Wrana J. *Sacrum a nowoczesność – rozważania na przykładzie kościoła św. Stanisława w Krakowie*. Wydawnictwo Architecturae et Artibus, vol. 8, no. 3, Białystok, 2016.

[18] de Palol P. et al., *Sztuka Świata*. Wydawnictwo Arkady, vol. 3, Warszawa, 1970.

---

[5] Ibid. p. 25

[19] Adamska M., Siewak-Sojka Z. et al., *Architektura świata*, *Architektura wczesnochrześcijańska i bizantyjska. Architektura wczesnego średniowiecza*. Wydawnictwo Dragon, Bielsko-Biała, 2011.

[20] Muratow P., *Obrazy Włoch*. Państwowy Instytut Wydawniczy, Warszawa, 1972.

[21] Bujak A., Sosnowska J., *Dom Świętego. Sanktuarium św. Jana Pawła II*. Wydawnictwo Biały Kruk, Kraków, 2015.

[22] *Dzieje Krakowa*, red. Bieniarzówna J., Małecki J., Mitkowski J., vol. 4, Kraków, 1979-1997.

Nonlinear finite element analysis of punching shear strength of reinforced concrete slabs supported on L-shaped columns

Qing Zhang[1], Graeme J. Milligan[2], Maria Anna Polak[3]

[1] *Department of Civil and Environmental Engineering (CEE); University of Waterloo;*
200 University Avenue West, Waterloo, Ontario, Canada; paris.zhang@uwaterloo.ca
[2] *Department of Civil and Environmental Engineering (CEE); University of Waterloo;*
200 University Avenue West, Waterloo, Ontario, Canada; gjmillig@uwaterloo.ca
[3] *Department of Civil and Environmental Engineering (CEE); University of Waterloo;*
200 University Avenue West, Waterloo, Ontario, Canada; polak@uwaterloo.ca

Abstract: Most current concrete design codes include provisions for punching shear of reinforced concrete slabs supported on columns with L, T, and cruciform shapes. Reference studies verifying the accuracy of these code provisions are typically not provided. Empirical data of punching failures of slabs supported on columns with L, T, and cruciform shapes are limited due to the cost and time required to test specimens with slab thicknesses and column sizes commonly used in practice. In this paper, the punching shear behaviour of five interior L-shaped slab-column connections, one without a slab opening and four with slab openings, subjected to static concentric loading are analyzed using a plasticity-based nonlinear finite element model (FEM) in ABAQUS. The FEM is similar to models previously calibrated at the University of Waterloo and was calibrated considering nine slabs that were tested to study the impact of column rectangularity on the punching shear behaviour of reinforced concrete slabs. The finite element analysis results indicate that shear stresses primarily concentrate around the ends of the L, and that current code predictions from ACI 318-19 and Eurocode 2 may be unconservative due to the assumed critical perimeters around L-shaped columns.

Keywords: punching shear, finite element analysis, L-shaped columns, slab openings

1. Introduction

Due to the complicated three-dimensional state of stress in the vicinity of the columns, reinforced concrete slabs supported on columns are susceptible to brittle punching shear failures. For slab-column connections without shear reinforcement, a punching shear failure occurs when the shear stresses due to the applied loads exceed the shear strength provided by

the concrete. Due to the brittle nature of the failure, a punching failure of one slab-column connection can lead to the progressive collapse of an entire structure.

Much research has been dedicated to the study of the punching shear behaviour of reinforced concrete flat slabs due to the brittleness of the failure. The majority of this past research has been experimental, and has involved the testing of isolated slab-column connections, where the portion of the slab included in the test approximates the negative moment area around the column. Even though the existing experimental punching shear database is extensive [1], [2], not all parameters have been sufficiently studied. For example, the punching shear behaviour of reinforced concrete slabs supported on L, T, and cruciform-shaped columns has received limited attention [3], [4] even though most current worldwide design codes include provisions for these column shapes [5], [6]. The derivation and reasoning behind these code provisions are unclear.

Empirical tests of slabs supported on L, T, or cruciform-shaped columns are limited due to the cost and time required to test specimens with slab thicknesses and column sizes seen in practice. Additionally, the measurement of quantities, such as the shear stress distribution in the slab, can be difficult in experiments, making it complicated to identify the portion of the slab and column which are effective in transferring loads. Nonlinear finite element analysis (FEA), calibrated to the results of experimental tests, can be used to efficiently supplement the existing experimental database, and allows for detailed investigations of the influence of specific parameters and the internal stress distribution in the slab.

In this paper, the punching shear behaviour of interior L-shaped slab-column connections subjected to static concentric loading with or without openings in the slab is analyzed using a three-dimensional nonlinear finite element model (FEM) implemented in ABAQUS using the Concrete Damaged Plasticity Model. The FEM used in this work is similar to other models used to study punching shear at the University of Waterloo [7], and it was calibrated considering the nine isolated interior slab-column connections tested by Hawkins, Fallsen, and Hinojosa [8]. These nine slab-column specimens were tested to study the influence of the column aspect ratio, β, on punching shear capacity, and the test results form the basis of the ACI 318-19 provisions relating punching capacity to β [5], [9]. As will be discussed herein, the ACI 318-19 provisions for square, rectangular, or L-shaped columns are the same, other than the shape of the assumed critical perimeter and calculation of β for L-shaped columns.

The punching shear provisions from ACI 318-19 [5] and Eurocode 2 [6] are evaluated by comparing the code and FEM predictions for five slabs supported on L-shaped columns, four of which have openings in the slab near the column. Additionally, the applicability of the assumed critical perimeter around L-shaped columns is investigated through an analysis of the slab shear stress distribution along the column perimeter. A brief discussion of the FEM calibration is also provided.

2. Punching shear design of L-shaped slab-column connections according to ACI 318-19 and Eurocode 2 (2004)

In punching shear design, the shear stress due to the applied load and shear stress resistance along a critical perimeter located at some distance from the column face are typically assumed to be constant. In ACI 318-19 [5] and Eurocode 2 [6], the critical perimeter for slab-column connections without shear reinforcement typically has the same shape as the column and is located at a distance of $d/2$ and $2d$ from the column face respectively. However, for L-shaped columns, the critical perimeter assumed in both codes does not follow the column perimeter, and is instead based on an assumed effective loaded area as shown in Fig. 1a.

Previous FEA of slabs supported on rectangular columns [10] and walls [11] has shown that the shear stresses along the column perimeter and the critical perimeters assumed in design codes, mainly that assumed in ACI 318-19 [5], are non-uniform and typically concentrate along the short sides and near the corners of the column. Similar stress concentrations are expected for slabs supported on L-shaped columns, and as such, it is hypothesized that the diagonal portion of the critical perimeter shown in Fig. 1a is ineffective in resisting punching shear.
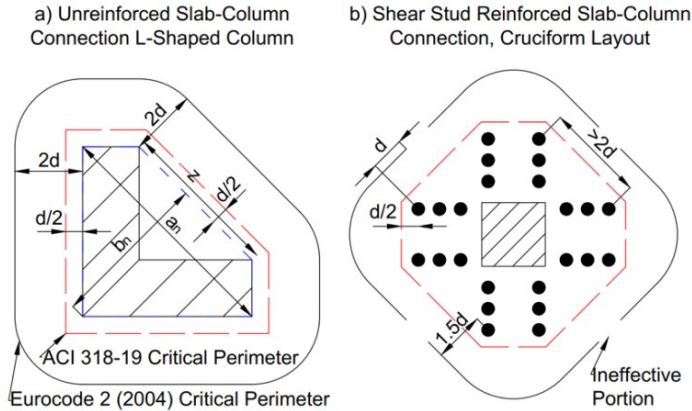

Fig. 1.   Critical perimeters assumed in ACI 318-19 [5] and Eurocode 2 [6]: a) around L-shaped columns, b) shear-reinforced connection with cruciform layout. *Source*: own study based on [5], [6]

Additionally, Eurocode 2 [6] assumes that the entire critical perimeter is effective for L-shaped slab-column connections without shear reinforcement. This contrasts with the assumed critical perimeter around slab-column connections with shear reinforcement arranged in a cruciform layout, where the diagonal distance between the outer shear reinforcement on adjacent sides of the column exceeds $2d$. When the diagonal distance between shear reinforcement on adjacent sides of the column exceeds $2d$, Eurocode 2 ([6]) assumes the reduced effective critical perimeter shown in Fig. 1b. This reduced critical perimeter accounts for large unreinforced portions of the slab near the column. However, no similar reduction is stated for unreinforced L, T, or cruciform-shaped slab-column connections where the diagonal distance between the inner flange edges, z (see Fig. 1a), exceeds $2d$. If an effective critical perimeter applies for the unreinforced portions of shear-reinforced slab-column connections, a similar reduction should apply to L-shaped columns with a large unreinforced zone between the column flanges.

In ACI 318-19 [5] the nominal shear capacity along the critical perimeter, v_c is calculated as the minimum of Eqs 1-3 regardless of the column shape:

$$0.33\lambda\lambda_s\sqrt{f_c'} \tag{1}$$

$$0.17\left(1+2/\beta\right)\lambda\lambda_s\sqrt{f_c'} \tag{2}$$

$$0.083\left(2+\alpha_s d/b_o\right)\lambda\lambda_s\sqrt{f_c'} \tag{3}$$

where λ is a parameter accounting for concrete density, λ_s is the size effect factor, f_c' is the concrete compressive strength (MPa), α_s is a term dependent on the column location, d is the effective slab depth (mm) and b_o is the critical perimeter length (mm). Eq. 2, which relates the nominal shear capacity to the column aspect ratio, β, was primarily derived from the results of

nine isolated slab-column tests by Hawkins, Fallsen, and Hinojosa [5], [8], [9]. Due to the lack of experimental tests of slabs supported on L-shaped columns, and since Eq. 2 is applied to both rectangular and L-shaped columns, these experimental tests, which are summarized in Section 3.2, form the basis of the FEM used in this study. For slabs supported on rectangular columns, β is defined as the ratio of the maximum and minimum column dimensions, but for slabs supported on L-shaped columns, β is defined as a_n/b_n, where a_n and b_n are defined as shown in Fig. 1a. As such the effective aspect ratio for L-shaped columns is significantly lower than the aspect ratio of the individual rectangular portions which make up the L-shape, which causes Eq. 2 to predict much higher nominal shear stress capacities.

3. FEA of L-shaped slab-column connections

3.1. Study overview

To verify if the diagonal portion of the critical perimeter around L-shaped columns assumed in ACI 318-19 [5] and Eurocode 2 [6] is effective in resisting punching shear, the four isolated slab-column specimens shown in Fig. 2, and one specimen without an opening in the slab are analyzed using the calibrated FEM discussed in the next section of this paper. Since the overall accuracy of the code provisions for L-shaped columns is unknown, three of the analyzed specimens contain openings in the slab between the column flanges. If the portion of the slab in the vicinity of the diagonal portion of the critical perimeter is ineffective in transferring loads between the slab and the column, the capacity of these three specimens (L1x6x1x4i, L1x6-1.2x1.2i and L1x6-1.2x1.2o) should be similar to that of the connection without an opening, L1x6-0.
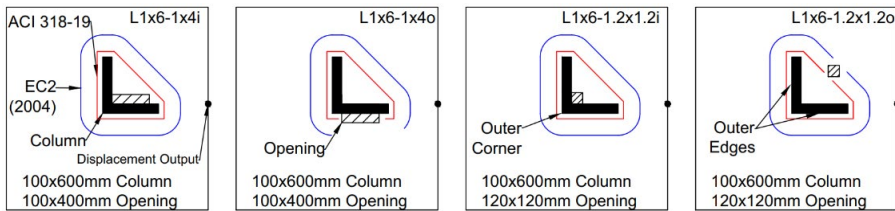

Fig. 2.   Slab-column specimens studied and critical perimeters used to calculate capacities according to ACI 318-19 [5] and Eurocode 2 [6] (specimen without opening, L1x6-0 not shown). *Source*: own study

If the capacity of the three specimens with openings between the column flanges is similar to that of the specimen without an opening, it proves that the diagonal portion of the critical perimeter is ineffective and should be neglected in the calculation of punching capacity. However, if this portion of the critical perimeter is ineffective, openings could be located in the region between the column flanges with a minimal impact on the connection's punching capacity, which is a significant benefit compared to slabs supported on square or rectangular columns, where the introduction of an opening near the column typically results in a significant decrease in capacity. Additionally, locating openings between the column flanges would allow the equipment or pipes requiring the openings in the slab to be easily concealed.

3.2. Overview of FEM

The punching shear behaviour of special-shaped slab-column connections has not been extensively studied, even though these connections were proven to have good seismic performance [3] and higher ductility and strength than conventional square slab-column connections [4]. Since previous experiments of slabs supported on L-shaped columns are limited, the FEM used in this study was calibrated based on the results of nine isolated slab-column tests performed by Hawkins et al. [8] focussed on determining the impact of the column aspect ratio, β, on punching shear behaviour.

The nine specimens tested by Hawkins et al. [8] are summarized in Tab. 1. All slabs were 2133.6 mm square in plan, 152.4 mm thick, and supported on rectangular columns located at the slab center. The investigated parameters included the column aspect ratio, β, concrete compressive strength, the loading pattern and the flexural reinforcement. The column length was 1041.4 mm for all nine specimens, and the column aspect ratio varied between 1 and 4.33. For slabs 1 through 6, eight equal concentrated loads were applied to the slab edges parallel to the short side of the column, except for slab 6, where the loads were applied on the slab edges parallel to the long side of the column. The eight equal concentrated loads are labelled as P in Fig. 3. For slabs 7-9, four additional concentrated loads were applied to the slab edges parallel to the long side of the column. The magnitude of each of these additional loads was 65% of the loads on the other slab edges, as shown in Fig. 3. The flexural reinforcement also varied between the slabs. One flexural reinforcement layout was used for slabs 1-4 and 6, and modified layouts were used for all remaining slabs. The parameters investigated included the flexural reinforcement ratio, effective depth, spacing and adding additional reinforcement in the vicinity of the column. For all slabs, the top reinforcement layer was placed in the direction of the P loads. A summary of the experimental setup is shown in Fig. 3a, and the modified slab dimensions used in the L-shaped column study are shown in Fig. 3b. The reasoning behind these modifications is discussed at the end of this section. The reinforcement layout for slab 1 was used in the L-shaped column study.

Table 1. Summary of slabs tested by Hawkins et al. [8] and FEA predictions. *Source*: own study

	Column Dimensions $(c_{min}$ x $c_{max})$		f'_c (MPa)	d (mm)[d]	V_{exp} (kN)	V_{FEA} (kN)	
Slab	Original	Modified				(a)	(b)
1	304.8x304.8	320x320	30.3[c]	117.3	383.9	326.0	336.8
2	203.2x406.2	200x400	26.3	117.3	351.4	331.3	332.2
3	152.4x457.2	160x480	32.0	117.3	333.2	339.9	351.8
4	114.3x495.3	120x480	31.0	117.3	330.5	331.8	337.2
5	152.4x457.2	160x480	26.9	117.3	355.0	325.8	332.6
6	152.4x457.2	160x450	22.7	117.3	335.8	300.9	308.2
7	152.4x457.2	160x480	25.9	117.3	319.8	297.7	307.3
8	114.3x495.3	120x480	26.1	120.65	314.5	292.5	298.4
9	152.4x304.8	160x320	29.5	120.65	315.4	285.0	287.7

(a) FEA predicted capacity considering specific slab parameters

(b) FEA predicted capacity considering modified slab and column dimensions

(c) used in analysis of L-shaped column specimens

(d) slab thickness, *h*, of 152.4 mm and column height of 1041.4 mm in original calibration, *h* and column height modified to 152 mm and 1068 mm respectively for $V_{FEA}^{[b]}$, $d = 117$ mm for all specimens for $V_{FEA}^{[b]}$, modified *d, h* and column height used in L-shaped column study
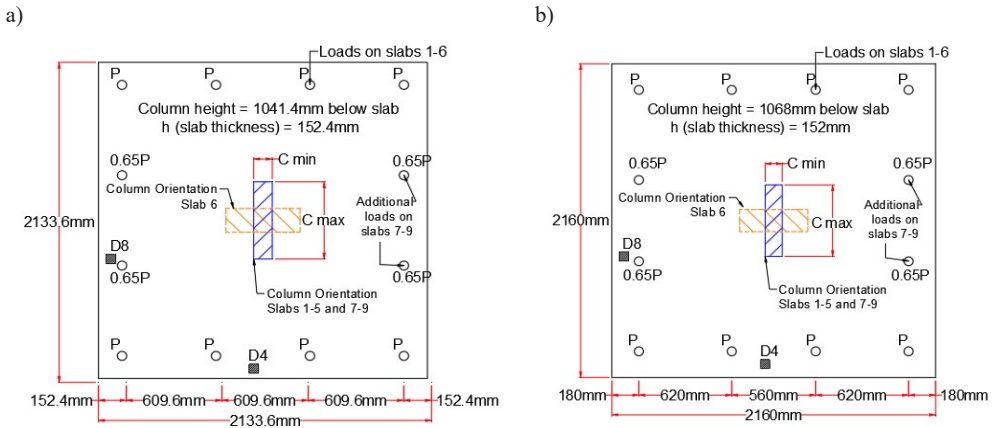
Fig. 3.   a) Experimental specimen dimensions and loading [8], b) modified dimensions
          * Note: in L-shaped column study, all concentrated loads have equal magnitude. *Source*: own study

In the FEM the concrete slab and column are discretized using three-dimensional, eight-node, hexahedral continuum reduced integration elements (C3D8R) and the steel reinforcement is discretized using three-dimensional, two-node linear truss elements (T3D2). Only a quarter of the slab-rectangular-column connections are modelled, taking advantage of symmetry, as shown in Fig. 4. For the L-shaped slab-column connections, the full isolated slab-column connection is modelled, and the symmetry boundary conditions used in the quarter model are removed.

Based on a comparison of the FEA predictions and experimental results, the parameters of the FEM were calibrated. A summary of the calibrated concrete parameters is provided in Tab. 2. The flexural reinforcement was modelled as linear-elastic perfectly plastic, with a yield strength of 414 MPa, Elastic Modulus of 200000 MPa and Poisson's ratio of 0.3. Applying the calibrated FEM to all nine specimens results in a maximum underprediction of 15.1% and a maximum overprediction of 2.0% compared to the experimental capacities. The predicted failure modes and crack patterns also agree with the experimental observations of Hawkins et al. [8].
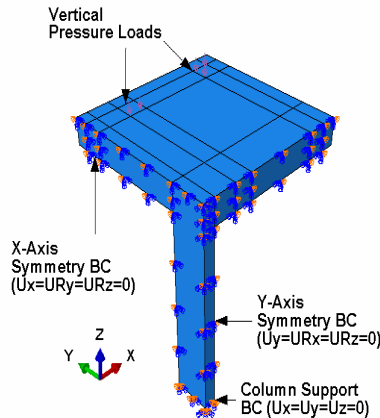

Fig. 4.   General boundary conditions used in FEM (slab 3 shown), ¼ models used in calibration, full slab
          specimen used in L-shape column study. *Source*: own study

Table 2.   Summary of concrete parameters in calibrated model. *Source*: own study

Material Model – Concrete Damaged Plasticity	Uniaxial Compression Model – Hognestad Parabola	Element Size – 20 mm
Dilation Angle – 42°	$E_c = 5000\sqrt{f_c'}$ (MPa)	Element Type – C3D8R
Eccentricity* – 0.1	Poisson's Ratio (v) – 0.2	
σ_{bo}/σ_{co}*– 1.16	Tension Model – Bilinear tensile stress-crack width [12]	*ABAQUS Default Value [13]
Damage Parameters – N.A.	G_f =0.08N/mm	

A comparison of the experimentally measured and FEA predicted load-displacement responses for slab 1 at the locations D4 and D8, as shown in Fig. 3 is provided in Fig. 5. It should be noted that the load-displacement response provided by Hawkins et al. [8] did not extend to the measured capacity, whereas the FEA predictions are included until the peak capacity predicted by the FEA. Even though the experimental curves are incomplete, important conclusions can be drawn. The calibrated FEM predicts a higher initial stiffness, likely due to the assumed uniaxial compressive stress-strain relationship for the concrete and due to the lack of temperature and shrinkage cracking in the FEM. However, the FEM predicts a similar stiffness to that measured experimentally in the plastic portion of the response.
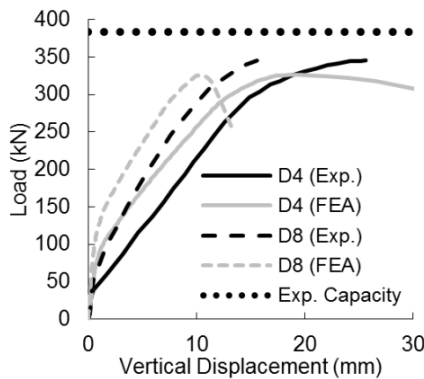

Fig. 5.   Comparison of the experimental and FEA load-displacement curves for slab 1. *Source*: own study (experimental data based on [8])

A comparison of the load-displacement response in the loaded and unloaded directions predicted by the calibrated FEM for slabs 1-6 and slabs 7-9 are provided in Fig. 6a, and Fig. 6b, respectively. For slab 1-6, which were loaded in one-way action, the FEM predicts a similar stiffness for all six slabs and a higher stiffness in the unloaded direction. A higher stiffness in the unloaded direction was also observed by Hawkins et al. [8] Unlike slabs 1-6, the predicted stiffness of slabs 7-9 is similar in both directions. The load-displacement response for slab 7 provided by Hawkins et al. [8] also displays similar stiffness in both directions, with the stiffness in the direction perpendicular to the short side of the column (D4) being slightly higher.
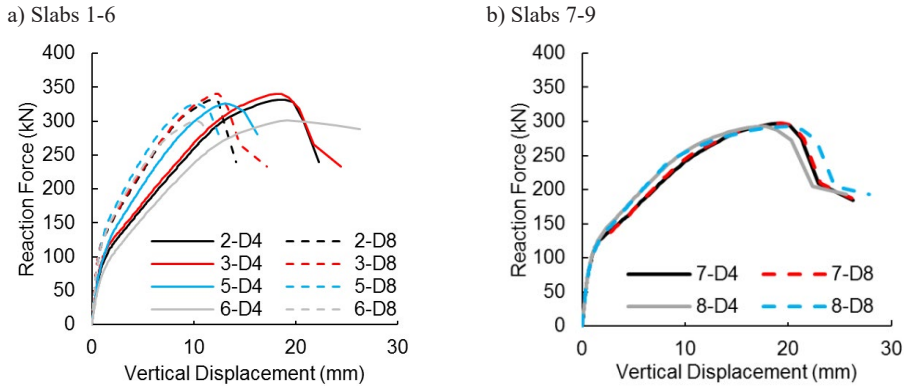
a) Slabs 1-6

b) Slabs 7-9

Fig. 6. Representative load-displacement curves at D4 and D8 locations for: a) slabs 1-6, b) slabs 7-9. *Source*: own study

As previously stated, the calibrated FEM is based on the Concrete Damaged Plasticity Model available in ABAQUS. This material model accounts for concrete cracking through a smeared crack approach, making the model results mesh size-dependent [14]. As mentioned previously, a global mesh size of 20 mm was found to result in the best correlation between the experimental and numerical results. In order to improve the mesh uniformity in the L-shaped column study, the slab dimensions, column dimensions and loading points were modified as summarized in Tab. 1, and Fig. 3b. The impact of these modifications for the Hawkins et al. [8] slabs was minor as shown in Tab. 1. The modified slab dimensions, column height, effective depth and loading point locations are used in the L-shaped column study, with equal loading applied on each point, as shown in Fig. 3b.

3.3. FEM results

Punching shear failures were predicted for all five specimens with L-shaped columns. On the tension surface of the slab there was a large concentration of cracks near the outer corner and along the outer edges of the L shape (outer corner and edges are labelled in Fig. 2). This cracking concentration suggests that a large portion of the total load is transferred along the outer edges of the L shape.
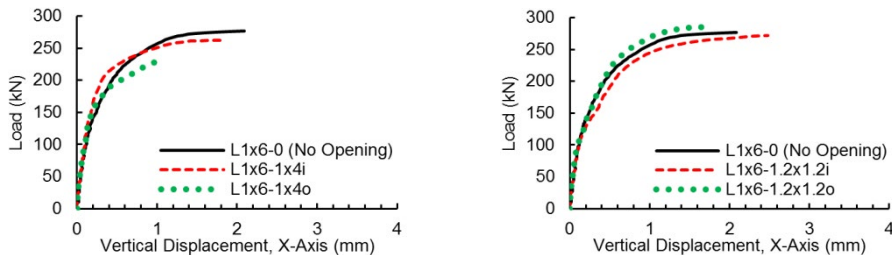

Fig. 7. Comparison of predicted-load displacement response (displacement location shown in Fig. 2). *Source*: own study

A comparison of the predicted load-displacement response for all five specimens, where the displacement is measured at the location shown in Fig. 2, is provided in Fig. 7, and the

capacities of each specimen predicted by the calibrated FEM are provided in Tab. 3. As expected the impact of openings located between the column flanges is minor, with a maximum decrease in punching capacity of 5.2% predicted for specimen L1x6-1x4i, compared to a decrease of 16.2% for the same opening size located on the outer edge of the column (L1x6-1x4o). This large decrease in capacity for an opening located on the outer edge of the column compared to openings located between the flanges supports the hypothesis that the diagonal portion of the critical perimeter assumed in ACI 318-19 [5] and Eurocode 2 [6] is ineffective in resisting punching shear.

Table 3. Comparison of punching capacity predicted by FEM, ACI 318-19 [5] and Eurocode 2 [6].
Source: own study

Specimen	Opening Size	V_{FEA} (kN)	V_{ACI} (kN)		V_{EC2} (kN)	
L1x6-0	None	277.1	523.3	382.4**	479.1	384.4**
L1x6-1x4i*	100x400	262.7	523.3	382.4**	479.1	384.4**
L1x6-1x4o	100x400	232.1	436.3	275.7**	372.1	277.4**
L1x6-1.2x1.2i*	120x120	271.7	523.3	382.4**	479.1	384.4**
L1x6-1.2x1.2o	120x120	284.9	509.6	382.4**	450.7	384.4**

*   Code required reduction in critical perimeter unclear. Full critical perimeter used in calculations

**   diagonal portion of critical perimeter neglected

An analysis of the shear stress distribution in the slab along the column perimeter further supports the hypothesis that the diagonal portion of the critical perimeter is ineffective. The shear stress distributions along the column perimeter predicted by ABAQUS for specimen L1x6-0 and L1x6-1x4o are provided in Fig. 8. As expected, shear stress concentrations at the column corners are predicted, and the shear stress magnitudes on the outer edges of the L are typically higher than those on the inner edges. However, unlike slabs supported on rectangular columns, only a very small amount of the total force is transferred along the short sides of the column, with the majority of the force being transferred along the outer edges of the column.

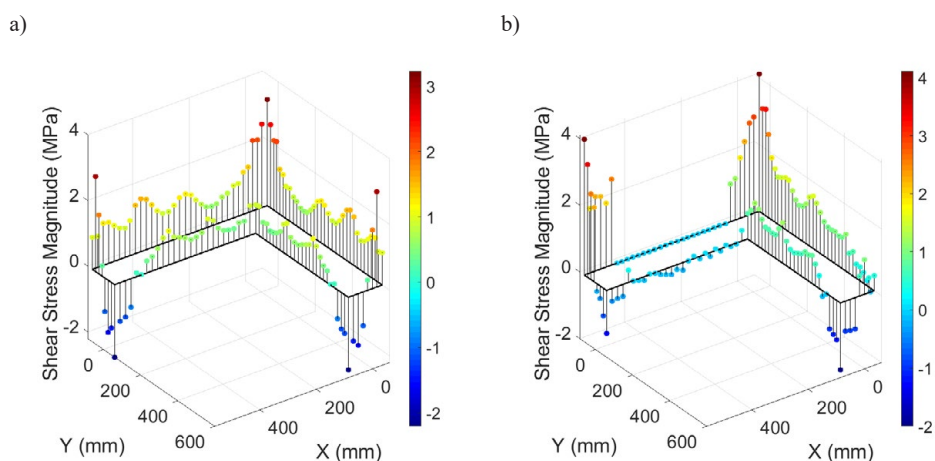a)   b)

Fig. 8.   Shear stress distribution along column perimeter: a) L1x6-0, b) L1x6-1x4o, 100% of peak load.
Source: own study

A comparison of the punching capacities predicted by the FEM, ACI 318-19 [5] and Eurocode 2 [6] is also provided in Tab. 3. As seen in Tab. 3, both the ACI 318-19 [5] and Eurocode 2 [6] provisions greatly overpredict the punching capacities predicted by the FEM for the five specimens, with ACI 318-19 [5] being more unconservative than Eurocode 2 [6]. Even if the diagonal portion of the critical perimeter assumed in both codes is neglected, both codes are still unconservative compared to the FEM predictions demonstrating that the punching behaviour of slabs supported on L-shaped columns is not accurately captured by either code. It is interesting to note that if the diagonal portion of the critical perimeter is neglected, both codes result in similar punching capacity predictions.

4. Conclusions

In this paper, the punching shear behaviour of five interior L-shaped slab-column connections, one without a slab opening near the column and four with slab openings, subjected to concentric vertical loading are analyzed using a plasticity-based three-dimensional nonlinear FEM in ABAQUS. The FEM, calibrated considering experimental results of nine interior slab-rectangular column connections, was used to verify the critical perimeter around L-shaped columns assumed in ACI 318-19 [5] and Eurocode 2 [6]. From the presented work, the following conclusions can be drawn:

1. The results of the FEA suggest that the effective critical perimeter around L-shaped columns assumed in ACI 318-19 [5] and Eurocode 2 [6] are incorrect. The capacity of the specimen without an opening is similar to that for the three specimens with openings located in between the flanges of the L. This similarity in capacity suggests that the diagonal portion of the critical perimeter is ineffective in resisting punching shear. The shear stress distributions along the column perimeter predicted by ABAQUS support the conclusion that the diagonal portion of the critical perimeter is ineffective. The predicted shear stress magnitudes along the inner sides of the L-shaped column are typically lower than those along the outer sides of the column, which demonstrates that the outer portion is more effective.

2. The punching provisions for L-shaped columns in ACI 318-19 [5] and Eurocode 2 [6] appear to be unconservative for connections with and without openings. Further analysis of multiple column sizes is required but the code predictions, even with the diagonal portion of the critical perimeter neglected, are unconservative compared to the FEA results for all five analyzed specimens.

3. The ideal location for an opening near an L-shaped slab-column connection is within the region between the column flanges as it minimizes the impact of the opening on punching capacity, while also allowing the equipment or pipes requiring the opening to be easily concealed.

References

[1] FIB, "Punching of structural concrete slabs", *fib Bulletin 12*, 2001.

[2] Ospina C.E., Birkle G., Widianto Y.W. et al., "NEES: ACI 445 Punching Shear Collected Databank", 2015.

[3] Wang Z.-j., Liu W.-q., Wang J., Jing Y.-s. and Xu C., "Shaking table test for a mid-highrise big-bay RC frame model", *Earthquake Engineering and Engineering Vibration*, vol. 19, no. 3, 1999, pp. 59-64 (in Chinese).

[4] Liu W. and Huang C., "Experimental investigation on punching shear behaviour of concrete slab-nonrectangular column connections", *Journal of Building Structures,* vol. 25, no. 4, 2004, pp. 26-33, (in Chinese).

[5] ACI Committee 318, Building Code Requirements for Structural Concrete (ACI 318-19) and Commentary on Building Code Requirements for Structural Concrete (ACI 318R-19), Farmington Hills, MI: American Concrete Institute, 2019.

[6] European Committee For Standardization, Eurocode 2: Design of concrete structures – Part 1-1: General Rules and Rules for Buildings, Brussels, Belgium, 2004.

[7] Genikomsou A.S., Milligan G.J. and Polak M.A., "Modeling Parameters in Punching Shear Finite Element Analysis of Concrete Slabs", *ACI Special Publication*, vol. 328, 2018, pp. 12.1-12.24.

[8] Hawkins N.M., Fallsen H.B. and Hinojosa R.C., "Influence of Column Rectangularity on the Behavior of Flat Plate Structures", *ACI Special Publication*, vol. 30, 1971, pp. 127-146.

[9] ASCE-ACI Committee 426, "The shear strength of reinforced concrete members – slabs", *Journal of the Structural Divison*, vol. 100, no. 8, 1974, pp. 1543-1591.

[10] Milligan G.J. and Polak M.A., "Finite Element Investigation on the Effect of Column Rectangularity on Punching Shear Strength of Concrete Slabs, The International Federation for Structural Concrete", in *fib Congress*, Melbourne, 2018, p. 12.

[11] Milligan G.J. and Polak M.A., "Finite Element Analysis of Shear Behaviour of Concrete Slabs Partially Supported on Walls", in *Concrete innovations in materials, design and structures: proceedings of the 2019 fib symposium, held in Krakow, Poland, May 27–29, 2019*, Kraków, 2019, pp. 1803-1810.

[12] Petersson E., *Crack Growth and Development of Fracture Zones in Plain Concrete and Similar Materials*. Division of Building Materials, LTH, Lund, Sweden, 1981.

[13] Dassault Systemes Simulia Corp., ABAQUS Analysis User's Manual 6.12-3, Providence, RI, USA, 2012.

[14] Genikomsou A.S. and Polak M.A., "Finite element analysis of punching shear of concrete slabs using damaged plasticity model in ABAQUS", *Engineering Structures*, vol. 98, 2015, pp. 38-48. https://doi.org/10.1016/j.engstruct.2015.04.016

Factors determining the quality of masonry – differentiation of resistance and reliability

Joanna Zięba[1], Lidia Buda-Ożóg[2], Izabela Skrzypczak[3]

[1] *Department of Building Structures, Faculty of Civil Engineering and Environmental Engineering, Rzeszow University of Technology, 2 Poznańska Street, Rzeszow 35-084, Poland, j.zieba@prz.edu.pl* (iD) *0000-0003-1800-5697*

[2] *Department of Building Structures, Faculty of Civil Engineering and Environmental Engineering, Rzeszow University of Technology, 2 Poznańska Street, Rzeszow 35-084, Poland, lida@prz.edu.pl* (iD) *0000-0002-1205-1345*

[3] *Department of Geodesy and Geotechnics, Faculty of Civil Engineering and Environmental Engineering, Rzeszow University of Technology, 2 Poznańska Street, Rzeszow 35-084, Poland, izas@prz.edu.pl* (iD) *0000-0003-0978-3040*

Abstract: A house or any other building without walls is truly hard to imagine. The first thing usually associated with walls is, of course, masonry. Today, masonry walls perform a load-bearing function in buildings up to four above-ground floors, in the higher parts of the buildings they perform a protective and stiffening function. However, there is a widespread opinion that the designer does not have to check the bearing capacity of masonry structures because masonry are were stand, are standing and will stand. Not everyone, however, currently works the wall as it should. The problem is that a lot of emphasis is now placed on reducing construction times. Therefore, there are a number of factors affecting the quality of the masonry structure, which overall reduce their safety. The article presents the influence of the quality of masonry on the differentiation of bearing capacity and reliability of an example masonry structure. The analyses included various values γ_m of the partial factor, recommended in the national annex PN-EN 1996-1 [1], depending on the category of masonry units, class execution of works and type of mortar. In addition, a decrease in load capacity and reliability caused by the increase of the initial eccentric resulting from the inaccuracy of the masonry wall was examined.

Keywords: masonry structures, reliability of construction, compressive strength, quality assurance

1. Introduction

Masonry structures are a type of structure which are still widely used in construction. Thanks to modern engineering tools, we can easily check the limited state of masonry elements.

However, in the light of today's requirements, checking only the limit state is not a sufficient step in the design process. The basis in the design of the structure is sufficiently safe and reliable design of the structure [2].

Regardless of the material chosen for the wall, its main function is to transfer loads to the lower parts of the structure and therefore it must be properly designed [3]. Errors in masonry structures can occur both at the design and execution stages. Until recently, there was a widespread opinion in the country that walls do not need to be checked computationally. In low-rise single-family buildings, the effort of the walls is indeed insignificant – which, however, does not exempt from checking the load-bearing conditions of the most loaded wall fragment. Even in buildings with a small number of floors, the load-bearing capacity of walls loaded mainly vertically may already fail, especially in elements with a small cross-section, such as window pillars and columns. Failure to check the load capacity of the wall for vertical loads may result in the adoption of too weak material or too small cross-section of the wall structural part, which may lead to overloading of the wall.

Despite the constant development of construction technologies, traditional masonry structures still remain one of the most common types of wall erection (it is estimated that in Poland they constitute about 90% of all walls made). Despite their popularity and long-standing tradition, masonry structures are still not free from manufacturing errors that may affect the fulfillment of the requirements set for buildings. It can easily be noticed just how important these issues are when recalling the seven so-called basic requirements for buildings, which are as follows:

- resistance and stability of the structure;
- fire safety;
- hygiene, health and the environment;
- safety of use and availability of facilities;
- noise protection;
- energy saving and thermal insulation;
- sustainable use of natural resources.

By combining the above requirements with the standard definition of masonry, which says that: masonry is a construction material made of masonry elements arranged in a specific way and permanently connected with each other with a proper mortar, a general conclusion can be made – the relevant elements have the effect of obtaining the assumed properties of masonry, properly selected mortar, as well as the quality of masonry work carried out. The basic source of information on the correct design and construction of walls is the package of Eurocode 6 standards: EN 1996-1-1 [1], EN 1996-1-2 [4], EN 1996-2 [5], EN 1996-3 [6].

2. The issue of masonry structure analysis due to their quality

When erecting masonry walls, not only their deviations from the vertical and level should be checked, but also the quality of details: corners and lintels, wreaths and wall reworking, in general – careful masonry work. There are a number of factors worth paying attention to when working with masonry, including: the quality of the building material – the masonry element and mortar, the quality of the masonry. The stages of erecting walls require inspection. For example, the first layer of the wall is very important – it must be well laid and leveled. Also, subsequent layers of walls must be erected in accordance with the masonry art (principles of

re-walling elements, wall connections, etc.) If the construction project lacks guidelines for the implementation of any of the details, they can be found in the relevant standards, ITB instructions and wall material manufacturers (they often have their own implementation recommendations).

In the design process, the quality of the masonry structure is reflected in the safety level adopted by the designer. Determining the value of the partial factor adopted in the calculations of the masonry structure is based on the determination of: the class execution of masonry works, the category of masonry elements, the type of mortar. The values of the basic partial factor determined by the polish annex EN 1996-1-1 [1] are presented in the table 1.

Table 1.   The exemplary values of the partial factor γ_m according to the polish annex EC6. *Source:* [1]

Material	Classes of execution control	
	A	B
masonry made with units of category I, designed mortar	1.7	2.0
masonry made with units of category I, prescribed mortar	2.0	2.2
masonry made with units of category II, any mortar	2.2	2.5

2.1. Classes of execution control according to the polish annex EC6 [1]

The construction of masonry elements is based on a number of basic assumptions, including the class of masonry. EN 1996-1-1 [1] distinguishes between five classes of execution of works 1 to 5, including two in the polish annex: class 2 and class 3, named accordingly class A and class B. The designer of the structure decides about the choice of the class of masonry works. The category of wall A may be adopted if:

- the works are carried out by a well-trained team under the supervision of a bricklayer;
- factory-made mortars are used, and if they are mortars made on site, the dosing of ingredients and mortar strength should be controlled;
- the quality of work is controlled by a person with appropriate qualifications, independent of the contractor.

In the event that the conditions for the construction of a category A wall are not met, the category of execution of wall B should be used.

2.2. Specificity of masonry units

At the construction stage, it is not always possible to determine the quality of the materials used. Features such as frost resistance, tendency to excessive shrinkage or swelling usually only appear after the first heating period. Commercially approved materials should meet the requirements of the standards used, e.g. masonry components of EN 771-1: 6 [7]. A distinction is made between category I and category II masonry [8]:

- category I includes masonry elements whose manufacturer declares that the plant uses quality control, the results of which state that the probability of occurrence of average compressive strength lower than the declared strength is not more than 5%;
- category II includes masonry elements whose manufacturer declares their average strength, and the other requirements of category I are not met.

Ensuring that the probability of occurrence of average compressive strength lower than the declared strength is not more than 5% requires ongoing monitoring of the strength of the

produced elements. They will be found in the standard for masonry elements EN 771 [7], which consists of the parts: EN 771-1 – clay masonry units, EN 771-2 – calcium silicate masonry units , EN 771-3 – concrete masonry units (from regular concrete or aggregate concrete light), EN 771-4 – autoclaved aerated concrete masonry units, EN 771-5 – manufactured stone masonry units, EN 771-6 – natural stone masonry units. Compressive strength is one of the most important functional properties of masonry units. However, you should be aware that the impact of this parameter does not translate proportionally into the compressive strength of the masonry wall. Therefore, equating the compressive strength of masonry units with the masonry wall compressive strength is a mistake. For example, the article [9] presents what factors influence the compressive strength of the masonry wall when calculating it in accordance with the applicable standard.

A group of masonry elements is also important in the analysis of the masonry structure. The group of masonry elements is determined on the basis of:

- the volume of all holes (percentage share in gross volume);
- single hole volume (percentage of gross volume);
- declared thickness of internal and external walls declared equivalent thickness of internal and external walls (% of gross width).

Based on the group of masonry elements, the *K* factor can be determined which determines the characteristic strength of the masonry wall.

2.3. Specificity of mortar

The specific type and strength of mortar provided in the design must be strictly used. The selection of the right mortar protects against possible defects in masonry constructions. The mortar should have adequate adhesion and strength adapted to the masonry element. The mortar should not have strength far exceeding the strength of masonry elements (too high mortar strength may cause wall damage). In addition to the permanent connection of elements, its second, equally important task is to evenly distribute the loads. Therefore, it is important to evenly distribute the mortar over the entire surface of the joined elements. A distinction is made between mortars produced on the factory and mortars produced on the building site.
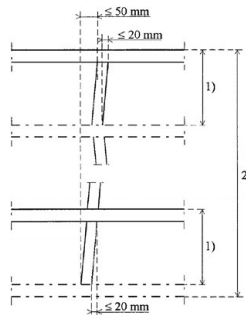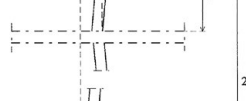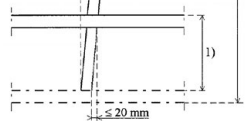
- the use of factory-made mortars and mortars manufactured on construction (for which the dosage of ingredients and strength of the mortar are controlled) authorizes the classification of works as category A;
- the use of mortars manufactured on construction, for which the mortar brand is determined only on the basis of its approximate volume composition, qualifies the performance of works as category B.

Guidelines for the correct execution of welds are clearly specified in EN 1996-1-1 [1]. Support joints (usually horizontal unless otherwise anticipated by the designer) and vertical joints made using ordinary mortars and light mortars should have an actual thickness of not less than 6 mm and not more than 15 mm (nominally 10 mm), while vertical and weld joints when using thin-joint mortar they should have an actual thickness of not less than 0.5 mm and not more than 3 mm (on average 2 mm). Masonry with unfilled vertical joints (unless the design clearly indicates the need to fill the vertical joint) can be made using masonry with profiled faces (tongue and grooves). When filling vertical joints, they can be considered filled if the mortar is on the entire joint height and width above 40% of the width of the masonry element. If at least one of the joined elements has a smooth face, the vertical joint should be filled with mortar.

2.3. The "verticality" of the masonry wall

In light of the requirements of EN 1996-1-1 [1], all construction works should be carried out in accordance with the given requirements and with permissible deviations. Most wall scratches can be avoided by improving the quality of the work. The performance of masonry structures significantly affects the load-bearing capacity, deformability and durability. The design recommendations provided in the standards for checking the limit states are only valid if the wall meets the relevant construction requirements. Only then can the simplifications adopted in the calculation models help ensure an appropriate level of security. Deviations of the made masonry structure from its assumed shape and location should not exceed the values given by the manufacturer of building materials and in the design documentation. EN 1996-2 [5] lists the permissible deviations – Table 2.

Table 2.   Permissible deviations for masonry elements. *Source:* [5]

Verticality	Maximum deviation
in anyone storey	± 20 mm
in total height of building of three storeys or more	± 50 mm
vertical alignment	± 20 mm

When analysing walls subjected to vertical loading, eccentricity resulting from construction deviations and differences in the material properties of individual components, should be made. An initial eccentricity, e_{init}, shall be assumed for the full height of a wall to allow for construction imperfections. The initial eccentricity, e_{init} may be assumed to be $h_{ef}/450$, where h_{ef} is the effective height of the wall. The effective height of a load bearing wall shall be assessed taking account of the relative stiffness of the elements of structure connected to the wall and the efficiency of the connections.

3. Impact of the quality of masonry on resistance and reliability

To illustrate the difference in the resistance of masonry walls resulting from the appropriate quality of masonry, an example of calculation of resistance for masonry made of clay masonry units by one of the Polish producers was presented. The work also shows the impact of the classes execution of works, categories of masonry units and mortar type on the reliability level of the designed structure. In addition, a decrease in load capacity and reliability caused by the increase of the initial eccentric resulting from the inaccuracy of the masonry was examined.

3.1. An example of differentiation of the resistance

The analysed masonry structures are located on the ground floor of a building. The height of the masonry wall is 2.75 m. The overview diagram of the analysed structure is shown in the figure – Fig. 1.
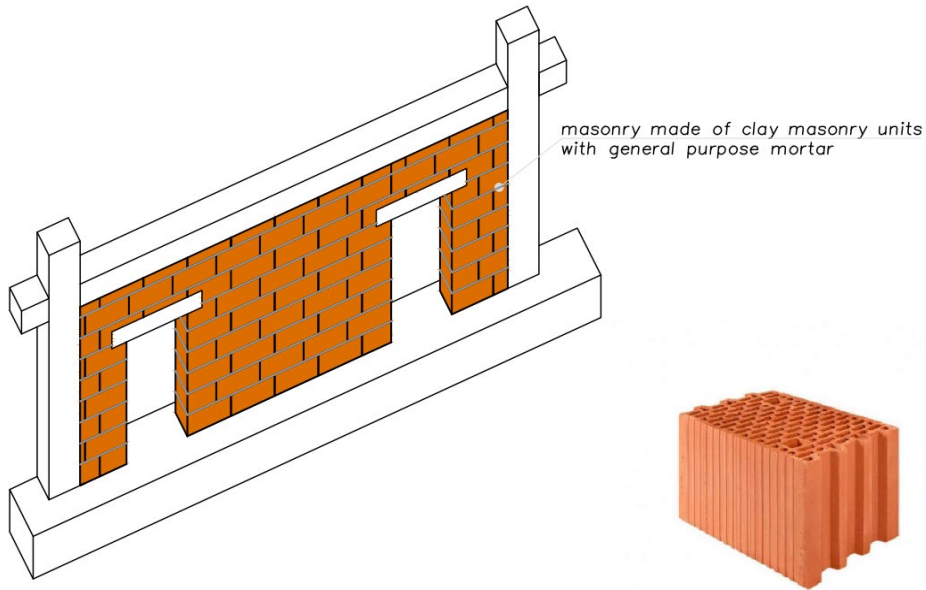
Fig. 1.   The overview diagram of the analysed structure. *Source:* own study

The framework model suggested by Eurocode for determining the resistance of the masonry was used. The wall should therefore be analysedat three points : at the top – point '1', in the middle – point 'm', at the bottom – point '2'. Design value of the vertical resistance of a masonry wall was determined from the formula:

$$N_{Rd} = \phi A f_d \tag{1}$$

where:

ϕ – reduction coefficient, in the analysed example only the initial eccentricity was taken into account, therefore:

$$\phi = 1 - 2\frac{e_{init}}{t} \tag{2}$$

A – masonry area;

f_d – design compressive strength of masonry.

Design compressive strength of masonry using Eurocode 6 [1] was assumed. Characteristic compressive strength of masonry of clay units with general purpose mortar is determined by formula:

$$f_k = K f_b^{0,7} f_m^{0,3} \tag{3}$$

where:

K – coefficient, for clay masonry units with general purpose mortar $K = 0.40$*;*

f_b – compressive strength of clay masonry units, $f_b = 15$ MPa;

f_m – compressive strength of mortar, $f_m = 5$ MPa.

Design compressive strength of masonry is determined by formula:

$$f_d = \frac{f_k}{\gamma_M} \tag{4}$$

where:

γ_M – relevant partial factor for materials.

Table 3.   Summary of load capacity calculations for the analysed masonry. *Source:* own study

Variant	Categories of masonry units	Classes execution of works	Type of mortar	Partial factor γ_M	Compressive strength [MPa]	Design value of resistance [kN]
1	I	A	designed mortar	1.7	2.54	611.3
2			prescribed mortar	2.0	2.16	519.6
3		B	designed mortar	2.0		
4			prescribed mortar	2.2	1.96	472.4
5	II	A	any mortar	2.2		
6		B		2.5	1.73	415.7

The differences in the calculated load-bearing capacity of the analysed masonry structure are presented in the form of a graph showing the percentage decrease in resistance of the masonry when switching to other variants of the structure analysis.
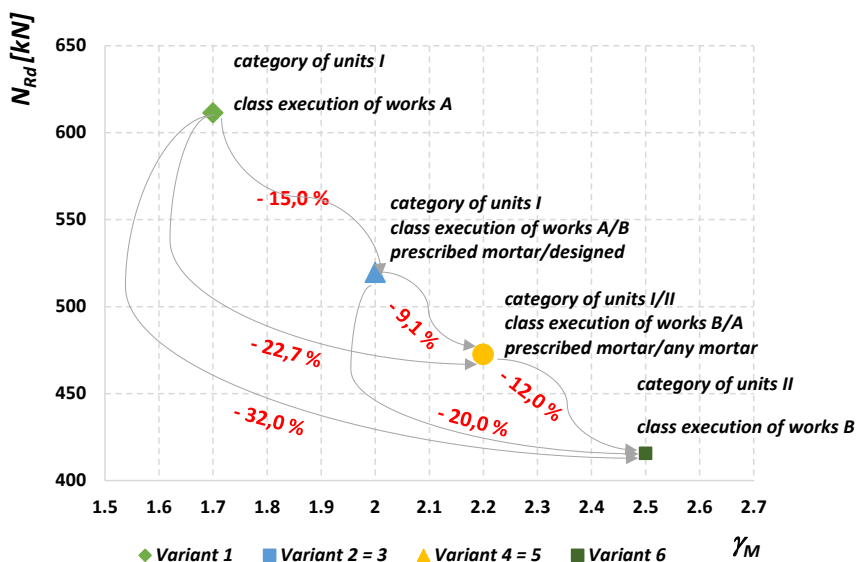

Fig. 2.   Differences in the calculated resistances of the analysed masonry. *Source:* own study

In the next stage of calculations, the value of the initial eccentric e_{init} was increased to the level of the maximum allowable deviation assumed in the Eurocode, i.e. e = 0.02 m. A decrease in masonry resistance of almost 13% was observed.

3.2. An example of differentiating masonry reliability

The properties and quality of materials affect the assessment of the reliability of building structures. A properly designed construction is one for which dependence is fulfilled:

$$N_{Rd} \geq N_{Ed} \tag{5}$$

where:

N_{Rd} – design value of the resistance;

N_{Ed} – design value of effect of action.

The designed resistance of a structural element is determined by the adopted calculation model and material properties [14]. Usually, they correspond to the specified quantile of the adopted statistical distribution of a specific material or product property [15], [16]. The procedure for the reliability analysis, in relation to the class execution of work and partial factors recommended in EC0 [10] and EN-ISO 2394 [9] was carried out. It has been assumed that the designed value of the resistance is equal to the designed value of effect of actions: $N_{Rd} = N_{Ed}$. Permanent and variable actions according to EC0 [10] can be combined with the relationships: 6.10a, 6.10b, 6.10. In the work with regard to the analysed structural element, only permanent actions and one variable action are considered. In order to determine the average of actions, the coefficient of variation for a constant action of $v = 0.10$ and for a variable action of $v = 0.20$ [12] was assumed. The relation between permanent and variable actions according to the formula was defined:

$$\chi = \frac{Q_k}{(G_k + Q_k)} \tag{6}$$

where:

G_k – characteristic value of a permanent action;

Q_k – characteristic value of a variable action.

Referring to literature, the coefficient of variation for the compressive strength of masonry $v = 0.19$ for variant 1 [13]. In the further part of the calculations, the coefficient of variation was increased by analogy to the percentage decrease in resistance for subsequent variants. The increase in the coefficient of variation is the result of a decrease in the quality of the masonry structure. For the presented element, the state of limit function has been built as follows:

$$Z = \left(1 - 2\frac{e_{init}}{t}\right) \cdot t \cdot l \cdot f_d - N_{Ed} \tag{7}$$

where:

e_{init} – initial eccentricity of a wall;

t – thickness of a wall;

l – length of a wall.

On the basis of the prepared database, the probabilities of exceeding the ultimate limit states and the corresponding reliability indices for individual action factors have been estimated. An important element of the example solution was determination of random variables occurring in the function of the limit state of the element being analysed. In determining the appropriate probability distributions, it was suggested to use literature that is rich in items concerning, for example, the determination of the probability density function for the compressive strength of masonry. Normal distribution was used for the permanent actions. Gumbel distribution was

used for the variable action. Log – normal distribution was used for the compressive strength of masonry. The analyses consisted in determining the reliability index β using the First Order Reliability Method (FORM). The results are presented in diagrams with reference to different construction classes execution of works, for reliability class RC2. The initial eccentricity of a wall and thickness of a wall were random variables with 5% coefficient of variation.
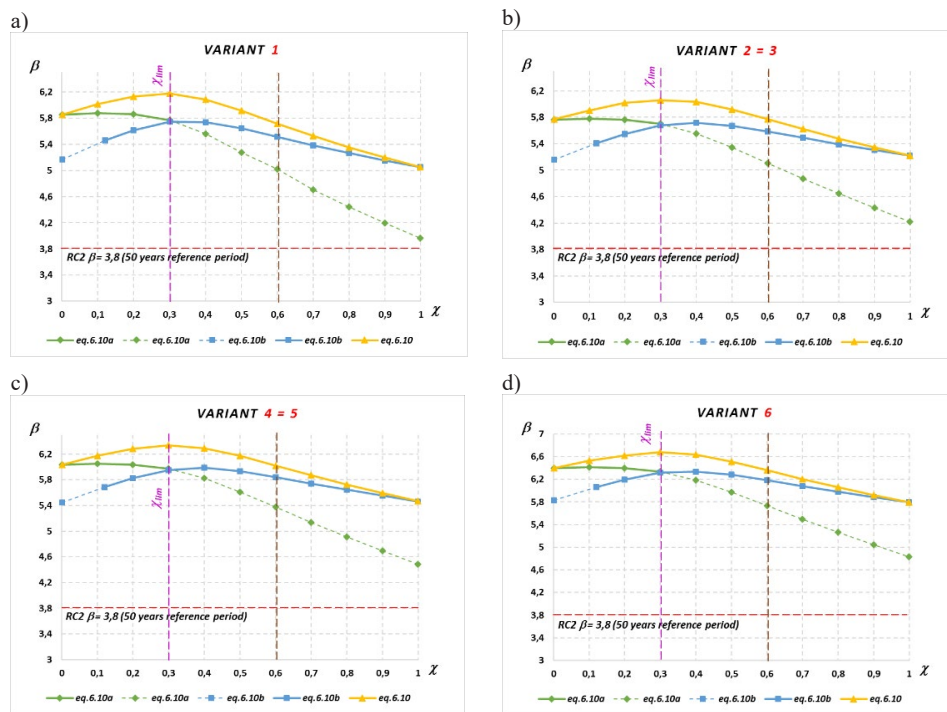

Fig. 3. Reliability coefficient curves β and load factor χ for three different combinations of standard coeffi-
cients (formulas: 6.10a, 6.10b, 6.10) – reliability class RC2: a) variant 1, b) variant 2=3, c) variant
4=5, d) variant 6. *Source:* own study

Analysing the graphs presented – Fig. 3, a slight increase in the level of safety should be noted along with the increasing partial factor from 1.7 to 2.5. The presented curves show the main intentions of the partial factor method – i.e. a higher value of the partial factor ensures a higher level of reliability in the structure. The approximate range of significance of each of the used combination formulas is marked on the charts with a solid line. The dashed line marks the remaining ranges of each curve, which for real values χ are not justified.

The minimum achieved value of β is 5.05 for variant 1, while the maximum achieved value is $\beta = 5.79$ for variant 6. The difference between the extreme values χ of the reliability indicator achieved in individual variants is about 13%. Therefore, it should be concluded that increasing the partial factor from 1.7 to 2.5 provides approximately 13% higher level of structural reliability.

In the next stage of calculations, variant 1 was modified by increasing the value of the initial eccentric e_{init} to the level of the maximum allowable deviation assumed in Eurocode 6, i.e. $e = 0.02$ m (variant 1A).
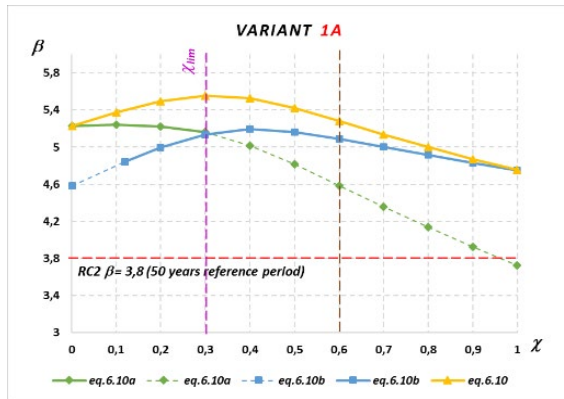
Fig. 4.   Reliability coefficient curves β and load factor χ for three different combinations of standard coef-
ficients (formulas: 6.10a, 6.10b, 6.10) – reliability class RC2: a) variant 1A. *Source:* own study

Comparing Fig. 3a and Fig. 4, one should notice smaller values of reliability index for the presented example. Increasing the initial eccentricity resulting from wall inaccuracy to 0.02 m results in a 6% lower reliability index value.

4. Quality control methods of masonry

4.1. Control of the production of masonry units

Standard EN 771 [7] was adopted by the European Committee for Standardization (CEN) and is a harmonized standard with the Construction Products Directive. All parts of this standard, with the exception of Part 6, provide for two conformity assessment systems:

- 2 + meaning mandatory certification of the factory production control and supervision over the certificate conducted by the certification body;
- 4 meaning the conduct of factory production control without external verification activities.

Certification of factory production control is carried out by a notified certification body, i.e. a body qualified by the competent minister or head of the central office and notified to the European Commission and EU Member States. According to PN-EN 771 [7], factory production control must be used in every masonry plant. In order to classify masonry elements in the 1st production category, it is necessary to use a 2 + conformity assessment system. It follows that e.g. stone masonry units described in the specification of the PN-EN 771-6 [6] natural standard can only be included in production category II.

Factory production control should include: measuring equipment; production equipment with control devices; raw materials and production process as well as finished products. The PN-EN 771 [7] standard specifies that the product compliance with the standard and the declared features is confirmed by the manufacturer on the basis of initial type tests and control tests of the manufactured products. These tests must be carried out by the manufacturer in both the 2 + conformity assessment system and in system 4. Preliminary type tests are carried out to confirm that the anticipated product properties meet the requirements of the standard and the values declared by the manufacturer. In the event of a change in raw materials or production

technology, these tests should be repeated. Type tests should cover all relevant properties of masonry elements related to their use, and thus:

- shape, dimensions and dimensional deviations;
- compressive strength;
- density and its deviations;
- frost resistance;
- water absorption;
- salt content;
- other relevant product features and applications.

Testing of masonry units should be carried out according to the methods given in the product standards. This is primarily EN 772 [17], consisting of many parts, each of which usually includes a method of testing one product feature. Factory production control should be carried out continuously, at every stage of production, by persons with appropriate qualifications and equipped with appropriate equipment. Control procedures should be recorded and their results documented.

4.2. Geodetic methods of inventorying verticality of walls

Control geodetic measurements, which include the measurement of deviations from the vertical plane of the facade walls of the building, are made to obtain information about the geometry of the object and determine deviations from their location. In the scope of measurement regarding deviations of facade walls from the vertical plane, the following methods of geodetic measurements have been the most common so far [18]: straight constant, angular spatial indentation forward, angular spatial indentation forward from 3 positions, polar 3D – total stations with reflector less measurement, polar 3D – scanning total stations (described in detail in [18]). The general principle of measuring the geometry of a building object regardless of the selected geodetic method remains the same, as the result is to obtain spatial coordinates of points selected on the building, which represent its geometry in the local coordinate system). Inventory measurements are a set of geodetic activities aimed at collecting appropriate geodetic data to determine: the location, shape and dimensions of completed buildings.

5. Conclusion

The article presents an example of differentiating the resistance of a masonry structure and its reliability due to the changing quality of workmanship. The analyses were carried out for several variants taking into account different categories of masonry elements, classes execution of works and changing mortar type. The reference value to the quality of the masonry structure was the changing partial factor determined by the national annex EC6 [1]. Analyses showed a decrease in the resistance of the structure by approximately 32% when using extreme γ_M values χ – from 1.7 to 2.5. In addition, it is also concluded that the value of the initial eccentric resulting from the inaccuracy of wall construction and adopted in the load capacity calculation is significant for the resistance of the structure. Analysing the value of the reliability coefficient obtained for individual variants, it is concluded that its value slightly changes in the γ_M variability range – from 1.7 to 2.5.

Technological progress in masonry constructions has resulted in the creation of competitive solutions, which forces the need for more and more accurate recognition of this type of

structure. Today's available control and monitoring technologies create a field to eliminate most construction problems resulting from poor quality of workmanship. Although it is probably still not possible to design, execute and operate masonry facilities with a full guarantee of no scratches or other defects, a significant part of these damages can be eliminated at the stage of execution and design.

References

[1]   EN 1996-1-1:2004 Eurocode 6: Design of masonry structures – Part 1-1: General rules for rein-forced and unreinforced masonry structures. 2004 CEN.

[2]   Stewart M.G., Lawrence S.J., "Model Error, Structural Reliability and Partial Safety Factors for Structural Masonry in Compression", *Masonry International*, vol. 20, no. 3, 2007, pp. 107-116.

[3]   Drobiec Ł., Jasiński R., Piekarczyk A., *Masonry structures according to Eurocode 6 and related standards*. PWN, vol. 2, Warsaw, 2013.

[4]   EN 1996-1-2:2005 Eurocode 6: Design of masonry structures – Part 1-2: General rules – Structural fire design. 2005 CEN

[5]   EN 1996-2:2006 Eurocode 6: Design of masonry structures – Part 2: Design considerations, selection of materials and execution of masonry. 2006 CEN.

[6]   EN 1996-3:2006 Eurocode 6: Part 3: Simplified calculation methods for unreinforced masonry structures. 2006 CEN.

[7]   EN 771-1:6, Specification for masonry units. 2005 CEN.

[8]   Buda Ożóg L., Skrzypczak I., Szylak K., Raczak A., *Masonry constructions – examples of calcu-lations according to Eurocode 6 and probabilistic methods*. Rzeszow University of Technology Publishing House, Rzeszow, 2017.

[9]   Rybarczyk T., „Czynniki wpływające na wytrzymałość muru na ściskanie", *Materiały Budowlane*, vol. 4, 2016, pp. 74-77. https://doi.org/10.15199/33.2016.04.20

[10] EN 1990:2002 Eurocode – Basis of structural design. 2002 CEN.

[11] PN-ISO 2394: General principles of reliability of building structures. 2010 CEN.

[12] Woliński Sz., *Fundamentals of Designing Structures in General Construction*. PWN, vol. 3, Warszawa, 2011, pp. 112-146.

[13] Woliński Sz., "Calibration of partial coefficients for existing structures", *Scientific Notebooks PRz*, 2011.

[14] Nowak A., Collins K., *Reliability of Structures*. CRC Press, 2012.

[15] Holicky M., Markova J., "Verification of load factors for concrete components by reliability and optimization analysis: Background documents for implementing Eurocodes", *Progress in Structural Engineering and Materials*, vol. 2, no. 4, 2000, pp. 502-507.

[16] Holicky M., Retief J.V., "Reliability assessment of alternative Eurocode and South African load combination schemes fot structural design", *Journal of South African Institution of Civil Engi-neering*, vol. 47, no. 1, (January 2005), pp. 15-20.

[17] EN 772-1, Methods of test for masonry units -Part 1: Determination of compressive strength. 2005 CEN.

[18] Ćwierz J., Cinal W., Kampczyk A., *Measurement of deviations of the building facade walls from the vertical plane*. https://doi.org/10.17512/znb.2016.1.04